Politecnico di Torino

ScuDo
Scuola di Dottorato ~ Doctoral School
WHAT YOU ARE, TAKES YOU FAR

Doctoral Dissertation
Doctoral Program in Electrical, Electronics and Communications Engineering (38^{th}cycle)

Digital Optical Performance Monitoring and Sensing of Coherent Long-Haul and Metropolitan Optical Fiber Links

Lorenzo Andrenacci
******

Supervisor(s):
Prof. Gabriella Bosco, Supervisor
Dr. Dario Pilori, Co-Supervisor
Prof. Roberto Gaudino, Co-Supervisor

Doctoral Examination Committee:
Prof. Elie Awwad, Télécom Paris
Prof. Marco Secondini, Scuola Superiore Sant'Anna di Pisa
Prof. Andrea Carena, Politecnico di Torino

Politecnico di Torino
2026

Declaration

I hereby declare that, the contents and organization of this dissertation constitute my own original work and does not compromise in any way the rights of third parties, including those relating to the security of personal data.

Lorenzo Andrenacci
2026

* This dissertation is presented in partial fulfillment of the requirements for **Ph.D. degree** in the Graduate School of Politecnico di Torino (ScuDo).

Abstract

This thesis investigates advanced signal processing techniques for optical performance monitoring (OPM) in long-haul and metropolitan fiber-optic networks. It demonstrates how the digital signal processing (DSP) already embedded in standard coherent transceivers can be leveraged to enable smarter, cost-effective, and flexible OPM solutions, meeting the evolving needs of modern high-capacity optical networks. The research is organized around two key areas of DSP-based OPM: digital longitudinal monitoring and optical fiber sensing.

Chapter 1 introduces the foundations of DSP in coherent transceivers and gives an overview of the historical development of OPM. It also presents the key concepts of digital longitudinal monitoring, focusing on longitudinal power monitoring algorithms, and explores the use of optical fiber for environmental sensing applications.

Chapter 2 presents novel applications of longitudinal power monitoring (LPM), including polarization-dependent loss (PDL) estimation and localization, as well as its extension to digital subcarrier-multiplexing (DSCM) and ultra-wideband (UWB) systems. A new PDL estimation algorithm based on least-linear squares (LLS) LPM is introduced and shown to provide accurate localization and magnitude estimates across a wide range of PDL configurations. Comparisons with a CM-based alternative highlight trade-offs between sensitivity and complexity. Further, LPM is applied to DSCM systems, demonstrating comparable accuracy despite increased profile noise. Experimental validation over a C+L band UWB link with Raman amplification confirms LPM's accuracy in tracking power evolution, underscoring its practical value in more complex transmission scenarios.

Chapter 3 proposes a new method for estimating Kerr-induced nonlinear interference (NLI) using only receiver-side DSP data. Integrated within the LLS-based LPM algorithm, the method is validated through simulations and experiments over 300-km and 1100-km links. It reliably estimates NLI power and predicts optimal launch conditions. Limitations related to estimating only the self-channel interference (SCI) component are addressed via analytical correction factors. Additionally, the chapter discusses implementation aspects, including

power offsets from using hard-decision symbols, and proposes a BER-based correction that maintains estimation accuracy within 0.3 dB.

Chapter 4 explores DSP-based fiber sensing using coherent receivers, comparing two length-integrated approaches: state-of-polarization (SOP) and optical phase-based sensing. SOP estimation is first analyzed for accuracy, with post-processing via moving averages shown to reduce angular deviation below 2° across different OSNR levels. Experimental and simulation results demonstrate strong consistency, confirming the method's robustness and hardware-independence. A comparative study over a 32-km urban link reveals superior performance of SOP-based sensing in noisy environments. While phase-based sensing suffers from environmental noise and demands narrow-linewidth lasers, SOP extraction can be implemented with minimal DSP modifications and no hardware upgrades, making it more suitable for real-world deployment.

Overall, this thesis establishes DSP-based OPM as a key enabler for next-generation optical networks and fiber sensing. By reusing existing DSP infrastructure, this approach reduces complexity and cost while supporting flexible, multi-impairment monitoring. The proposed methods provide practical insights and validated solutions for deploying adaptive, intelligent monitoring strategies, paving the way toward elastic optical networks and integrated sensing platforms.

Contents

List of Figures

List of Tables

Nomenclature

Acronyms / Abbreviations

ADC Analog-to-Digital Converter

AEQ Adaptive Equalizer

AIR Achieveable Information Rate

ANN Artificial Neural Network

ASE Amplified Spontaneous Emission

AWGN Additive White Gaussian Noise

BER Bit Error Rate

BPS Blind Phase Search

CD Chromatic Dispersion

CDC Chromatic Dispersion Compensation

CM Correlation Method

CMA Constant Modulus Algorithm

CPE Carrier Phase Estimation

DAC Digital-to-Analog Converter

DAS Distributed Acoustic Sensing

DBP Digital Back-Propagation

DD Direct Detection

DFB Distributed-Feedback

DFOS Distributed Fiber Optic Sensing

DGD Differential Group Delay

DLM Digital Longitudinal Monitoring

DSCM Digital Subcarrier Multiplexing

DSP Digital Signal Processing

DT Digital Twin

DWDM Dense Wavelength Division Multiplexing

EDFA Erbium-Doped Fiber Amplifier

EGN Enhanced Gaussian Noise

EON Elastic Optical Network

eRP Enhanced Regular Perturbation

EVM Error Vector Magnitude

FEC Forward-Error Correction

FFT Fast Fourier Transform

FIR Finite Impulse Response

FOC Frequency Offset Compensation

FWM Four-Wave Mixing

GMI Generalized Mutual Information

GN Gaussian Noise

GSNR Generalized Signal-to-Noise Ratio

HD Hard Decision

IM Intensity Modulation

ISRS Inter-channel Stimulated Raman Scattering

LLS Linear Least Squares

LMS Least Mean Squares

LO Local Oscillator

LPM Longitudinal Power Monitoring

MCI Multi-Channel Interference

ML Machine Learning

MMSE Minimum Mean Square Error

NLI Nonlinear Interference

NLPR Nonlinear Phase Rotation

NLSE Nonlinear Schroedinger Equation

OCM Optical Channel Monitor

OPM Optical Performance Monitoring

OSA Optical Spectrum Analyzer

OSNR Optical Signal-to-Noise Ratio

OTDR Optical Time-Domain Reflectometers

PDF Probability Density Function

PDL Polarization-Dependent Loss

PMD Polarization Mode Dispersion

PPE Power Profile Estimation

PSD Power Spectral Density

QAM Quadrature-Amplitude Modulation

QoS Quality of Service

QPSK Quadrature-Phase-Shift Keying

RBW Reference Bandwidth

RF Radio Frequency

RMSE Root-Mean-Square Error

ROADM Reconfigurable Optical Add-Drop Multiplexer

RP Regular Perturbation

RTO Real-Time Oscilloscope

RX Receiver

SCI Self-Channel Interference

SCM Subcarrier Multiplexing

SD Soft Decision

SDH Synchronous Digital Hierarchy

SDN Software-Defined Network

SMF Single-Mode Fiber

SNR Signal-to-Noise Ratio

SOA Semiconductor Optical Amplifier

SONET Synchronous Optical NETworking

SOP State of Polarization

SOP-PSDG State of Polarization - Power Spectral Density Gap

SOPAS SOP Angular Speed

SPM Self-Phase Modulation

SRS Stimulated Raman Scattering

SSFM Split-Step Fourier Method

SSMF Standard Single-Mode Fiber

SVD Singular Value Decomposition

TOF Tunable Optical Filter

TRX Transceiver

TX Transmitter

VOA Variable Optical Attenuator

WDM Wavelength-Division Multiplexing

WSS Wavelength-Selective Switch

XCI Cross-Channel Interference

XPM Cross-Phase Modulation

Chapter 1

Introduction

This chapter introduces the fundamental concepts that will be addressed throughout this PhD thesis. Sec. 1.1 presents the overall research framework, outlining the motivation and objectives that guide this study. Sec. 1.2 describes the main building blocks of the digital signal processing (DSP) module in coherent receivers, which represents a central component of modern optical communication systems. Sec. 1.3 provides a literature review of the main optical performance monitoring (OPM) techniques, highlighting their fundamental principles and describing their evolution over time. Sec. 1.4 introduces the principal methods for longitudinal power monitoring (LPM), which constitute one of the most relevant OPM approaches considered in this work. Sec. 1.5 presents the main strategies for fiber sensing, with particular attention to their application in leveraging existing optical infrastructure for monitoring purposes. Sec. 1.6 provides an outline of the thesis structure, while Sec. 1.7 lists all the scientific publications produced during the course of this PhD.

1.1 Research Framework

Optical communications have undergone a remarkable evolution since the advent of low-loss optical fibers in the 1970s enabled long-distance lightwave transmissions. Early field trials in the late 1970s and early 1980s demonstrated bit rates in the range of a few megabits per second, soon advancing to systems capable of hundreds of megabits and later gigabits per second [1]. The introduction of erbium-doped fiber amplifiers (EDFAs) in the late 1980s [2] and wavelength-division multiplexing (WDM) in the 1990s [3] pushed aggregate transmission

capacities to tens of gigabits and later terabits per second, laying the foundation for today's global information infrastructure.

A major breakthrough in the evolution of optical communications came with the advent of coherent detection in the late 1980s. Unlike direct detection, coherent receivers are capable of recovering both the amplitude and phase of the optical field, which improves both the sensitivity and the spectral efficiency. Early demonstrations of coherent quadrature-phase-shift keying (QPSK) transmission paved the way for the development of advanced modulation formats [4]. However, practical deployment was initially delayed by the technological limitations of analog phase and polarization tracking.

The revival of coherent communications in the mid-2000s was driven by the emergence of high-speed digital signal processing (DSP) [5]. By moving impairment mitigation into the electrical domain, DSP allowed to remove the need for elaborate optical compensation schemes, enabling electronic correction of chromatic dispersion (CD), polarization mode dispersion (PMD), and phase noise at the receiver [6]. This paradigm shift decoupled the system performance from the limitations imposed by the optical hardware, opening the door to flexible and adaptive transmission architectures.

The combination of DSP and coherent systems offers a wide range of benefits. They allow for the use of higher-order quadrature-amplitude modulation (QAM) formats, such as 16-QAM and 64-QAM, increasing both the per-channel spectral efficiency and capacity without requiring additional bandwidth. DSP also enables advanced techniques including probabilistic constellation shaping [7] and nonlinearity compensation [8]. As a result, digital signal processing has not only increased the achievable rates and extended the practical reach and efficiency of optical communication systems, but also represents a fundamental element for modern and future network scaling. As an example, Fig. 1.1 from [9] gives a representation of the evolution of commercial optical systems and an extrapolation of the future trends.

However, the exponential growth of global data traffic increases the demand for high-capacity optical communication networks. Several applications, ranging from cloud computing and artificial intelligence to future 5G/6G and beyond services, place stringent requirements on network throughput, reliability, and adaptability. To meet these demands, modern optical networks employ advanced modulation formats, reconfigurable optical add-drop multiplexers (ROADMs), and flexible-grid architectures [10]. While these elements make the use of the available spectrum more efficient and the provisioning of capacity more dynamic, they also increase the complexity and vulnerability of transmission systems exposing it to a wide

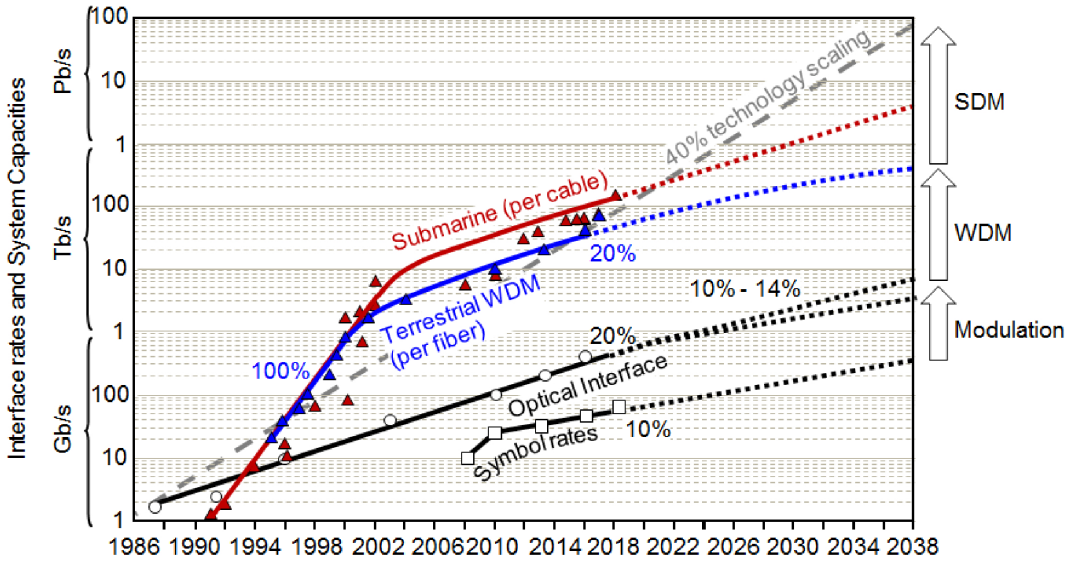

Fig. 1.1 Trends in data rates and capacity of commercial optical transmission systems: past 30 years and future outlook. Source: [9].

range of impairments with dynamic and stochastic nature, which makes their compensation and management increasingly challenging. For this reason, it is crucial to obtain continuous and accurate information about the state of both signals and links, ensuring robust operation, operational costs reduction and spectral efficiency maximization.

Optical performance monitoring (OPM) provides the means to fulfill this requirement and refers to a set of techniques designed to estimate key network parameters, enabling fault detection and localization, as well as impairment-aware resource allocation [11]. However, practical implementation of OPM presents several challenges. Traditional approaches often rely on hardware-based solutions, e.g., optical spectrum analyzers (OSAs) and other external monitoring modules, which increase system costs and complexity. Another issue is scalability: as networks grow in size and traffic volume, cost-effective monitoring solutions must be deployable at multiple points in the network without significantly increasing capital and operational expenditure. In this framework, the advent of digital coherent receivers represents a turning point. Coherent detection combined with DSP has enabled powerful impairment compensation and, simultaneously, provides inherent monitoring capabilities. DSP-based OPM allows key transmission parameters to be extracted directly from existing receiver operations, such as adaptive equalization or other DSP stages, with no need for additional optical hardware [12].

This approach offers several advantages. First, it is cost-effective, since it reuses the DSP hardware already present in coherent transceivers, avoiding the need for expensive external monitoring devices. Second, it is flexible, as algorithms can be adapted through software updates without modifying the hardware. Third, DSP-based OPM enables multi-impairment monitoring, where several impairments are tracked simultaneously and independently, providing a thorough view of link performance. Finally, it facilitates the use of advanced signal processing and machine learning techniques, paving the way for intelligent and adaptive monitoring strategies in future elastic optical networks (EONs) [13], such as digital twin (DT)-based strategies that are becoming increasingly popular [14]. Moreover, existing fiber networks constitute a valuable resource for detecting anomalous vibrations along the cables, including those induced by earthquakes, construction activities, or fiber tampering [15]. DSP-based OPM can further support such fiber-sensing applications by enabling the detection of these impairments in an instrument-free manner [16].

DSP-based (or digital) OPM is consequently a key research area that continues to evolve and attract significant attention, as will be discussed in more detail in the following.

1.2 Digital Signal Processing in Coherent Optical Communication Systems

To gain a better understanding of DSP-based OPM it is convenient to review the standard DSP structure used in modern coherent receivers. Unlike intensity-modulation direct-detection (IM-DD) systems, which recover only the optical intensity, coherent receivers detect both the amplitude and phase of the received optical field, allowing for full reconstruction of the complex signal after detection. When combined with high-speed DSP, coherent receivers provide the flexibility and robustness required to meet the escalating capacity demands of modern optical networks [17]. The importance of DSP in coherent receivers lies in its ability to digitally compensate for transmission impairments that accumulate along the optical channel. Following transmission through an optical link and coherent detection, the signal is generally affected by both deterministic and stochastic impairments, such as CD, PMD, laser phase noise, and carrier frequency offsets. While earlier generations of optical communication systems relied on optical-domain compensation, e.g., dispersion-compensating fibers, tunable filters, and polarization controllers, these approaches were costly and difficult to scale. In contrast, DSP offers a reconfigurable, purely-electrical solution that not only compensates

for impairments but also enables the use of spectrally efficient and higher-order modulation formats [18].

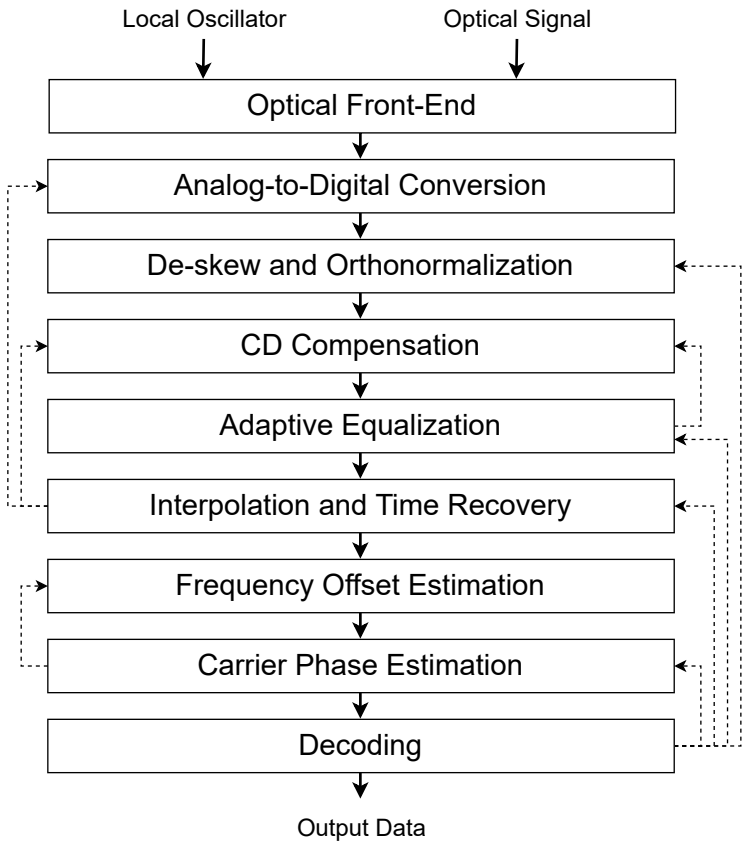

Fig. 1.2 High-level schematic of a standard DSP chain in modern optical coherent receivers.

In general, standard DSP modules consist of a series of functional blocks, each dedicated to compensating specific channel or system impairments. In Fig. 1.2 a high-level schematic of the DSP chain is presented, including potential feedback paths between processing blocks. In this context, the most relevant blocks include:

- **Chromatic dispersion compensation:** this block compensates for the pulse broadening of the optical signal caused by the wavelength-dependent group velocity of the propagating field. CD compensation is typically implemented through digital filtering, either in the time domain using finite impulse response (FIR) filters or in the frequency domain using fast Fourier transform (FFT)–based filters [6].

- **Adaptive equalization:** while polarization multiplexing allows to increase the transmission capacity by a factor 2, it requires the receiver to separate the two orthogonal polarizations,

which can become arbitrarily mixed during propagation. Moreover, adaptive equalizers mitigate additional impairments, including PMD, residual CD not compensated in earlier CD compensation stages, and potential filtering effects arising during signal propagation along the link. They can be implemented using various approaches, including blind techniques, such as the constant modulus algorithm (CMA), or decision-directed methods, such as the least mean squares (LMS) algorithm [19].

- **Frequency offset estimation:** in practical systems, transmitter and local oscillator (LO) lasers are generally not perfectly aligned in frequency. This mismatch introduces a frequency offset that causes fast symbol rotation in the received constellation. DSP algorithms estimate and remove this offset, typically using blind methods [20] or data-aided schemes [21]. Precise frequency offset compensation is essential to ensure the correct operation of the subsequent carrier phase estimation stage.
- **Carrier phase estimation:** even after frequency alignment, the residual phase noise stemming from the linewidth of the lasers employed for transmission and reception introduces random fluctuations in the signal phase. Carrier phase estimation algorithms are employed to estimate and correct this noise. Depending on the modulation format, techniques such as the Viterbi–Viterbi algorithm for QPSK [22], data-aided phase estimation [23], or blind phase search (BPS) for higher-order QAM formats are used [24].

Note that the DSP algorithms used to compensate channel impairments also provide useful information on the impairments themselves. For instance, the tap coefficients in the adaptive equalization stage reflect the amount of chromatic dispersion or polarization rotation in the link, while carrier recovery algorithms yield estimates of frequency offsets and phase noise. In this way, DSP not only enables reliable high-speed transmission but also represents an inherent tool for the monitoring of the physical layer. This dual role has led to the concept of digital OPM, where impairment estimates obtained from DSP are used to evaluate transmission quality, monitor system status, and support adaptive network control. DSP thus functions not only as the enabler of coherent optical communications, but also as the basis for a more flexible and cost-effective performance monitoring in future EONs.

1.3 Overview of Optical Performance Monitoring

As it is possible to observe in Fig. 1.3, OPM plays a central role in the optimization loop of optical network operation. Monitoring provides necessary information on network conditions,

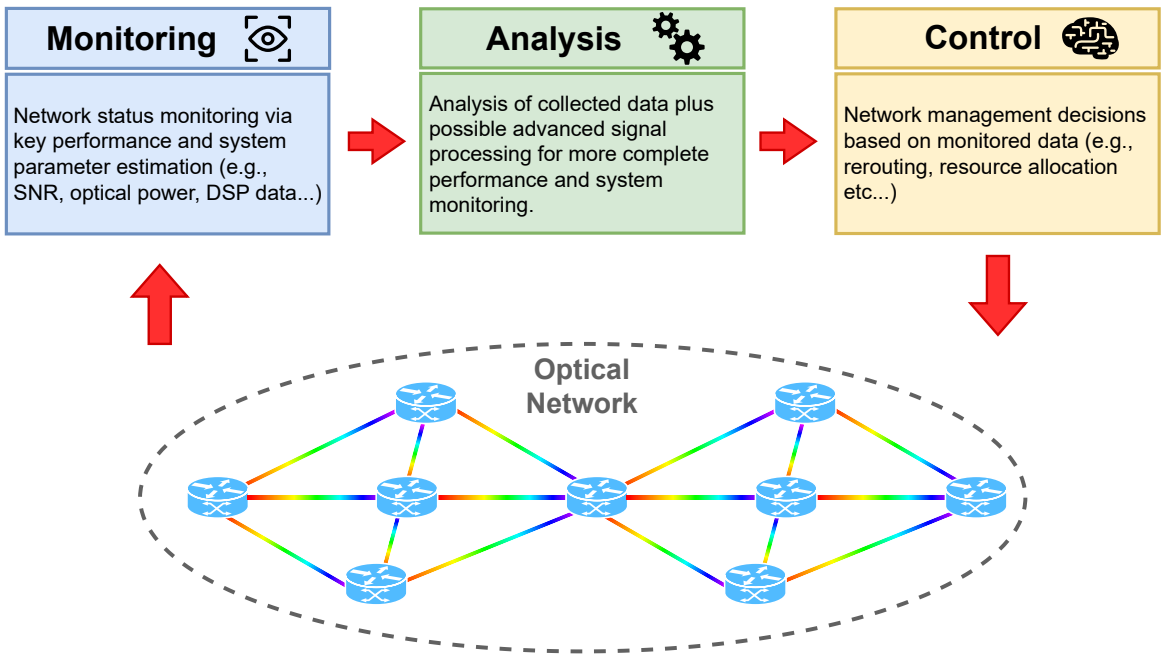

Fig. 1.3 Visual representation of the key stages in optical network operation optimization: monitoring, analysis and control.

including parameters such as signal-to-noise ratio (SNR), optical power levels, and outputs from DSP stages in optical receivers. These data are essential for the subsequent analysis stage. During analysis, they are processed to identify degradations, anticipate possible impairments, and assess suitable responses. Finally, the control stage implements these responses by adjusting network resources and parameters accordingly. The interaction between monitoring, analysis, and control creates a continuous feedback loop that enables efficient, adaptive, and reliable operation of optical networks.

Over the past decades, though, OPM techniques have evolved, and even the concept of OPM itself has shifted to reflect the changing needs of optical network technologies. As transmission systems have become more advanced and new demands have arisen, monitoring solutions have been adapted and extended to satisfy these new requirements. For this reason, a review of OPM solutions, starting from the early steps and moving toward the approaches in use today is given in the following. This also serves as an introduction to the main subject of this thesis.

1.3.1 Early Steps and Evolution of Performance Monitoring

OPM solutions started emerging in the early 1990s as a response to the limitations of traditional monitoring methods in optical networks. While conventional performance monitoring at the SONET/SDH layer provided information about bit error rates and quality-of-service (QoS) parameters, it did not offer direct insights into the specific impairments affecting the physical layer. OPM, by contrast, was conceived as the monitoring of physical-layer signal quality parameters and impairments, such as the optical signal-to-noise ratio (OSNR), Q-factor, CD, PMD, and timing jitter, thus enabling a more direct evaluation of signal health in the optical domain [25]. The initial motivation for OPM arised from the increasing transparency of optical transmission systems and the advent of dense wavelength division multiplexing (DWDM), which significantly reduced the available transmission margins [26]. In these systems, impairments accumulated over long distances and across multiple channels, while electronic regeneration points became fewer. Hence, new mechanisms were required to guarantee fault management, amplifier control, and reliable service delivery at the transparent optical layer. Research initiatives such as NUTEK and MONET played a fundamental role in highlighting the importance of OPM and demonstrating its feasibility through early field trials [27].

The first implementations of OPM were rather indirect, though. They typically relied on component alarms, e.g., monitoring amplifier pump currents, laser drive levels, or thermal parameters. In a similar way, aggregate power measurements or simple optical channel monitoring (OCM) provided information on channel presence, wavelength, and average power . These methods were not expensive and easy to integrate into existing systems. However, they suffered from a fundamental limitation: signal degradation could still occur even when all components appeared to be working in nominal state. A second class of early techniques used tone-based monitoring. In this case, subcarrier multiplexing was used to superimpose low-frequency radio-frequency (RF) tones on each optical channel, so that the tones could later be detected and analyzed to estimate the per-channel power and, in some cases, accumulated impairments like CD or PMD [28, 29]. Nevertheless, these approaches historically suffered from problems such as “ghost tones” created by amplifier cross-gain modulation, which impaired their reliability.

As optical networks moved toward higher rates, longer transmission distances, and reconfigurable architectures, the initial monitoring solutions were no longer sufficient. This led to the development of advanced OPM techniques, designed to both detect faults and identify their causes, enabling a possibly more adaptive control. A key breakthrough was the

development of OSNR monitoring techniques, initially implemented through technologies such as Fabry–Perot and Bragg grating filters [30], later refined with polarization-based approaches [31] and subcarrier methods [32]. At the same time, dispersion monitoring became crucial, targeting both CD and PMD. Proposed methods included phase-to-amplitude conversion [33], RF subcarrier delay [34], vestigial sideband filtering [35], and degree-of-polarization techniques [36]. Finally, a step forward was the introduction of Q-factor monitoring. Because measuring BER in the middle of a link required expensive O/E/O regeneration, Q-factor methods emerged as a cost-effective alternative. These techniques provided a reliable estimate of signal quality [37].

1.3.2 Towards DSP-based Monitoring of Modern Optical Networks

Although the previously reported methods enable the estimation of specific system parameters, they are extremely specific to those objectives and, in general, require modifications to the transmission system or the deployment of additional monitoring equipment [38]. This, of course, increases both monitoring and network-management costs. Moreover, modern optical networks operate in highly flexible environments where throughput and reliability must be guaranteed. Meeting these demands requires OPM solutions capable of operating on very short timescales (or even in real time) [39], while monitoring a broader set of system parameters than traditional approaches. This enables a more complete view of network conditions. Such approach is also beneficial in terms of cost per bit: having a deeper knowledge on the network parameters allows to preserve correct operation and high reliability while reducing design and operational margins, generally large to compensate for limited network knowledge [40, 41].

As already mentioned, a major turning point in this context was the introduction of coherent detection in combination with DSP [11]. Apart from compensating transmission impairments, DSP in coherent receivers also provides direct information about those impairments, making it a practical tool for more comprehensive, software-based (or DSP-based) monitoring. This approach significantly reduces monitoring costs, as the required data are inherently available during normal receiver operation, and it reduces the dependence on external measurement devices such as OSAs, OCMs, or optical time-domain reflectometers (OTDRs). While these devices are still essential in optical networks, they are not capable of providing a comprehensive view of the optical network and their scaling is not cost-effective. By contrast, DSP-based monitoring is inherently dependent on the proper operation of the receiver DSP chain and can function correctly only when this chain is fully operational. A

notable example is provided in [12, 42], where residual CD, accumulated PMD, accumulated polarization-dependent loss (PDL) and the system transfer function are jointly estimated leveraging the tap coefficients of the adaptive equalizer within the DSP of a coherent receiver. The method operates in a weakly nonlinear regime and relies on the appropriate modeling of these effects, e.g., modeling PDL matrices as Hermitian and PMD matrices as unitary. This clearly demonstrates the amount of information that is inherently contained within the DSP blocks and the potential of DSP-based methods for OPM. In general, numerous solutions have been proposed within this paradigm and can be categorized based on their main features and the signal-processing techniques on which they rely.

Pilot-tone modulation has been widely investigated as a cost-effective approach for OPM for some time now [43]. The basic principle consists in applying a low-frequency, small-intensity amplitude modulation on top of a high-speed data signal. At the receiver, only a small fraction of the optical power is tapped and converted into an electrical signal by a photodetector, with processing carried out by DSP. Since no dedicated external instrumentation is required, pilot-tone-based monitoring offers low cost and the possibility of large-scale deployment in optical networks. More advanced schemes have extended this concept to multi-band pilot tones [44], in which different modulation tones are applied to different channels. This enables accurate monitoring of a wide range of parameters, including optical spectrum [45], filter fault identification and localization [46], OSNR [47] and nonlinear noise [48].

Another approach to OPM is provided by machine learning (ML)-based techniques. Data-driven methods rely on labeled datasets of eye diagrams or amplitude histograms with corresponding impairments such as CD, differential group delay (DGD) and OSNR. Artificial neural networks (ANNs) have been successfully applied to jointly monitor OSNR, CD, and DGD [49] and infer OSNR from spectral features [50]. More advanced deep learning methods can further enhance performance: deep neural networks extract OSNR and modulation-format-sensitive features from amplitude histograms [51], while convolutional neural networks leverage raw eye diagrams and asynchronous delay-tap plots for OSNR monitoring and modulation format identification [52]. Hybrid approaches have also been proposed to incorporate physical knowledge and improve generalization. Gaussian process regression has been used to estimate parameters such as attenuation and nonlinear coefficients based on prior bounds and physics-based simulators [53]. More recently, physics-informed neural networks have been introduced, directly embedding governing equations into the training loss, enabling estimation of system parameters like dispersion and Raman gain spectrum from transmitted and received signals [54].

A recent breakthrough has been the development of digital longitudinal monitoring (DLM) techniques, which extend performance monitoring in the fiber-longitudinal direction [55]. This approach enables spatially-resolved estimation of signal and system parameters, allowing not only the detection of specific impairments but also their localization along the optical link.

1.3.3 Advent of Digital Longitudinal Monitoring

The capability to obtain spatially-resolved estimates of system and performance parameters directly from data-carrying signals during standard system operation offers several advantages, such as anomaly detection and localization, thus enhancing cost-effectiveness and efficiency of the optical network. In recent years, numerous applications have been explored, such as in [56], where fiber anomalies are localized by exploiting cross-channel interference (XCI). Most of these approaches, however, rely on a fundamental DLM technique: longitudinal power monitoring (LPM). LPM refers to a set of techniques designed to estimate the evolution of the optical power profile along the propagation direction of a signal transmitted over an optical link. These techniques typically exploit Kerr-induced nonlinear effects in optical fibers, such as self-channel interference (SCI) [57], combined with appropriate models of fiber propagation and the associated nonlinear effects.

The very first contribution in this field was presented in [58] and then extended in [59]. This approach, initially named in-situ power profile estimation (PPE), laid the foundation for correlation method (CM)-based LPM. In this approach, power profiles are computed by performing a series of correlation operations between a reference signal, obtained as a reconstruction of the originally transmitted waveform, and partially nonlinear compensated versions of the received signal. An example of output is reported in Fig. 1.4, clearly showing how the power profile evolution of the propagated signal is captured by the algorithm. Subsequent works have introduced several algorithmic modifications. For instance, [60] proposed performing correlation operations over entire signals rather than dividing them into smaller batches, while [61] suggested virtual forward propagation combined with a linearization of the nonlinear operators in the propagation model.

In parallel, alternative approaches have been explored by leveraging the structural similarities between ANNs and the digital back-propagation (DBP) algorithm. For example, [62] experimentally demonstrated power profile estimation and subsequent anomaly detection using a neural network-based adaptive DBP scheme. This approach exploits the fact that signal power is proportional to the nonlinear phase rotations (NLPRs) induced by the Kerr

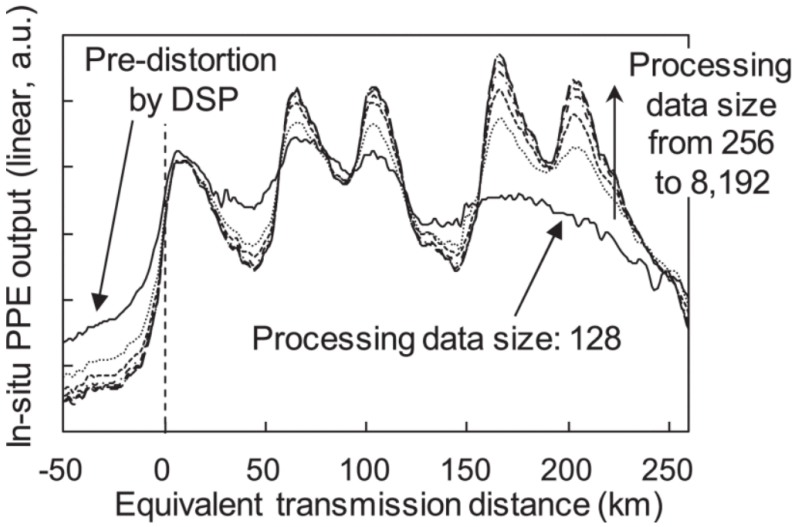

Fig. 1.4 Outputs of CM-based LPM algorithm vs. transmission distance for different processing data size. Source: [59].

effect during propagation. By adapting the NLPRs within the DBP algorithm, it is possible to get an estimate of the evolution of the power profile along the link. This approach can be defined as adaptive DBP or minimum mean square error (MMSE)-based method [63]. Although some improvements have been proposed to enhance its performance (e.g., optimizing the step size employed in the DBP algorithm [64]), a turning point was represented by the linearization of the MMSE-based LPM. In [65], it was demonstrated that replacing the SSFM model, on which DBP is based, with the regular perturbation (RP) model for the virtual propagation of the reference signal allows the optimization problem to be reformulated as a linear least-squares (LLS) problem, whose solution exists in closed form. This enables a closed-form expression for the entire power profile estimation, eliminating the need for computationally heavy iterative processing based on stochastic gradient descent, which also introduces the risk of convergence to wrong local minima. This approach is generally known as LLS-based LPM [66]. Similarly to CM-based LPM, algorithmic modifications have been proposed also for LLS-based LPM. For instance, [67] introduced the estimation of a complex-valued scaling factor to account for possible phase mismatch between the reference signal and the received signal after CPE, while [68] proposed a generalized method for LPM showing how the introduction of a Tikhonov regularization factor allows to move from LLS-based to CM-based LPM and vice versa based on the levels of accuracy and robustness required. Also, a multi-stage approach to implement LLS-based LPM at one sample-per symbol was proposed in [69]. A comparison between the two main LPM methods is reported in Fig. 1.5.

This provides the basis for discussing the main differences and limitations of the two algorithms. To begin with, LLS-based LPM estimates absolute power values (assuming that the nonlinear parameter γ is known), whereas CM-based LPM only provides relative power values in the form of correlation metrics. Consequently, anomaly detection and localization are more straightforward with LLS-based LPM, while CM-based LPM requires additional calibration procedures [70]. Furthermore, CM-based LPM exhibits modulation-format dependence, particularly near the transmitter, which requires CD pre-distortion and thus increases complexity [59]. It was shown in [71] that CM-based LPM can be interpreted as a convolved version of LLS-based LPM, due to an inherent low-pass filtering effect arising from non-zero correlations between nonlinear contributions at adjacent positions. Interestingly, this low-pass effect enhances CM-based LPM by improving its robustness to noise and other distortions, though reducing its accuracy. Finally, deconvolution strategies for CM-based LPM have been proposed, and their performance has been compared to that of LLS-based LPM, proving rather equivalent [72].

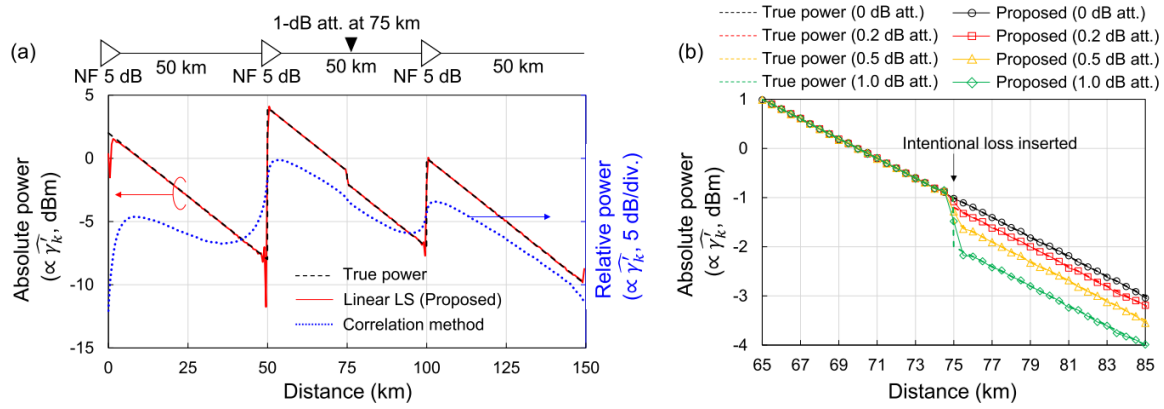

Fig. 1.5 Comparison between LLS-based and CM-based LPM performance. (a): power profile estimation and (b) LLS-based LPM anomaly detection capabilities. Source: [66].

To conclude, the applications of these methods are not only limited to power profile estimation [73]. Numerous uses have been demonstrated starting from LPM, including CD map estimation [63], optical amplifier gain tilt [63, 74], optical filter tuning [63], multi-path interference estimation [61] and fiber-type identification [75]. In [76] the first field trial of a 4D (i.e., distance, time, frequency and polarization-resolved) link tomography using a commercial transponder is presented. Notably, LPM has also been recognized as a promising and cost-effective approach for detecting potential physical-layer attacks (e.g., fiber tapping) through the identification of their characteristic power signatures [77] or other network soft failures by integrating it within the software-defined network (SDN) controllers, enabling more efficient and potentially self-healing optical networks [78].

1.4 Longitudinal Power Monitoring

The principal LPM algorithms share a common structure. At the receiver side, the transmitted signal is first reconstructed and then virtually propagated through a simulated (or DT) link. Depending on the chosen method, either correlation operations or LLS optimizations are carried out in combination with the actual received signal to estimate the power profile. A schematic representation of this process is shown in Fig. 1.6.

Since LPM constitutes the main tool underlying most of the works presented in this thesis, this section provides a more detailed overview of its principal methods. First, the nonlinear Kerr effect and the main fiber propagation models are briefly introduced. This step is essential, as LPM algorithms exploit the non-commutativity of linear and nonlinear effects during fiber propagation, thus, a more in-depth understanding of these models is useful to fully understand this concept. Then, the algorithmic details of the two primary approaches, namely CM-based and LLS-based LPM, are introduced. Finally, a comparative analysis of their respective advantages and limitations is presented.

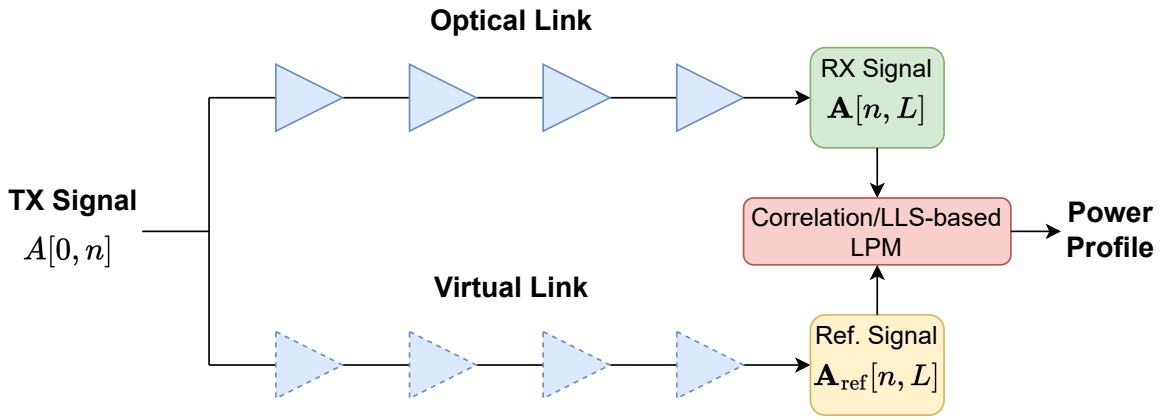

Fig. 1.6 Common structure of the main longitudinal power monitoring methods: LLS-based and CM-based LPM. Adapted from: [71].

1.4.1 Kerr-induced Nonlinear Effects in Optical Fibers

In this section, a fundamental nonlinear effect occurring during optical fiber propagation is presented: the Kerr effect. When light propagates through a dielectric medium, its interaction with the bound electrons induces a polarization that, under weak fields, is approximately linear in the applied electric field. However, for sufficiently intense electromagnetic fields, this response becomes nonlinear. At a microscopic level, this nonlinearity arises from the

anharmonic motion of bound electrons in the silica matrix. The macroscopic polarization **P** induced in the medium can be expressed as a power series in the electric field **E** [79]:

$$\mathbf{P} = \varepsilon_0 \left(\chi^{(1)} \cdot \mathbf{E} + \chi^{(2)} \cdot \mathbf{EE} + \chi^{(3)} \cdot \mathbf{EEE} + \cdots \right) \tag{1.1}$$

where ε_0 is the vacuum permittivity and $\chi^{(j)}$ is the j-th order susceptibility tensor. The linear susceptibility $\chi^{(1)}$ defines the refractive index and absorption coefficient, while the second-order susceptibility $\chi^{(2)}$ is responsible for effects such as second-harmonic and sum-frequency generation [80]. Since silica is symmetric at the molecular level, $\chi^{(2)}$ vanishes, and second-order processes are absent under normal conditions. Consequently, the third-order susceptibility $\chi^{(3)}$ becomes the dominant nonlinear contribution in silica fibers. The lowest-order nonlinear effects in optical fibers arise from nonlinear refraction, also known as the optical Kerr effect. This effect corresponds to the dependence of the refractive index on the optical intensity:

$$\tilde{n}(\omega, I) = n(\omega) + n_2 I = n(\omega) + \bar{n}_2 |E|^2 \tag{1.2}$$

where $n(\omega)$ is the linear refractive index, I is the optical intensity, and $\bar{n}_2$ is the nonlinear index coefficient, related to the real part of $\chi^{(3)}$ by

$$\bar{n}_2 = \frac{3}{8n} \mathrm{Re}\left[\chi^{(3)}_{xxxx} \right] \tag{1.3}$$

for linearly polarized fields.

The most direct manifestation of the Kerr effect is self-phase modulation (SPM) or self-channel interference (SCI), where an optical pulse induces a phase shift on itself as it propagates through the fiber. The total phase shift after a length L is:

$$\phi = \tilde{n} k_0 L = \left(n + \bar{n}_2 |E|^2 \right) k_0 L \tag{1.4}$$

with $k_0 = 2\pi/\lambda$ and λ the operating wavelength. The nonlinear contribution is therefore:

$$\phi_{\mathrm{NL}} = \bar{n}_2 k_0 L |E|^2 \tag{1.5}$$

which grows with the instantaneous intensity.

In WDM systems or when multiple fields propagate simultaneously, the Kerr effect also leads to cross-phase modulation (XPM) or cross-channel interference (XCI), in which the

intensity of one channel induces a phase shift on another. Considering two optical fields at frequencies ω_1 and ω_2, polarized along the same axis, the total field can be written as:

$$E = \tfrac{1}{2}\hat{x}\left(E_1 e^{-j\omega_1 t} + E_2 e^{-j\omega_2 t}\right) + \text{c.c.} \tag{1.6}$$

where c.c. stands for complex conjugate and $\hat{x}$ is the polarization axis. The nonlinear phase shift experienced by the field at ω_1 is

$$\phi_{\text{NL}} = \bar{n}_2 k_0 L \left(|E_1|^2 + 2|E_2|^2\right). \tag{1.7}$$

Here, the first term corresponds to SCI, while the second term represents XCI. A key feature is that, for equally intense signals, the contribution of XCI is twice as strong as SCI. This makes XCI a dominant impairment in WDM systems, often responsible for asymmetric spectral broadening and nonlinear crosstalk between channels.

Finally, another nonlinear multi-channel interference (MCI) mechanism is four-wave mixing (FWM). This type of effect arises from the beating among different channels at distinct frequencies, which generates new frequency components. In simple terms, the i-th, j-th, and k-th channel frequencies can interact to produce an l-th frequency that was not originally present. The problem becomes more severe when channels are equally and closely spaced, as the newly generated components may overlap with existing channel frequencies, coherently mixing with them. Moreover, the FWM process draws energy from the original signals, reducing their power.

In general, these nonlinear effects are described by the third term in the right-hand side of the nonlinear Schroedinger equation (introduced in the following), where the nonlinear parameter γ can be expressed as

$$\gamma = \frac{2\pi}{\lambda}\frac{n_2}{A_{\text{eff}}} \tag{1.8}$$

and A_{eff} denotes the effective area of the mode in the fiber.

Several approaches have been developed to model NLI. In the time domain, the pulse-collision theory has been proposed [81], while in the frequency domain the most established model is the Gaussian Noise (GN) model [82], which assumes that NLI behaves as additive Gaussian noise. However, some limitations of the GN model were later identified, such as its independence from modulation format, the assumption of noise symmetry in the complex plane, and the absence of phase noise [57, 83]. These issues were subsequently addressed through the enhanced Gaussian Noise (EGN) model [84].

1.4.2 Fiber Propagation Models: SSFM and eRP

The propagation of an optical field in an optical fiber is governed by the nonlinear Schroedinger equation (NLSE). Let us consider, for simplicity, the single-polarization optical field $E(t,z)$, where t is the time coordinate and z is the spatial coordinate in the fiber-propagation direction. The NLSE can be expressed as

$$\frac{\partial}{\partial z}E(t,z) = j\frac{\beta_2(z)}{2}\frac{\partial^2}{\partial t^2}E(t,z) - \frac{\alpha(z)}{2}E(t,z) - j\gamma(z)\left|E(t,z)\right|^2 E(t,z) \tag{1.9}$$

where $\beta_2(z)$ is the CD coefficient, $\alpha(z)$ the fiber attenuation parameter and $\gamma(z)$ the nonlinear fiber parameter. This equation consists of two distinct contributions: a linear term and a nonlinear term. It can therefore be reformulated as

$$\frac{\partial}{\partial z}E(t,z) = \hat{D}\{E(t,z)\} + \hat{N}\{E(t,z)\} \tag{1.10}$$

where $\hat{D}$ accounts for the linear contribution, i.e., CD and attenuation, and $\hat{N}$ for nonlinear contributions. Because the equation is not fully linear, the superposition principle does not hold and the individual contributions cannot be separated. Moreover, no general analytical solution exists. Nevertheless, by considering sufficiently short fiber segments of length dz, such a separation can be approximated with limited error, enabling the application of numerical methods, such as the SSFM [85]. In the SSFM, each step is computed by alternating the nonlinear operation in the time domain:

$$E_N(t,z+dz) = e^{-j\gamma(z)|E(t,z)|^2 dz}E(t,z) \tag{1.11}$$

and the linear operation in the frequency domain:

$$E_D(t,z+dz) = e^{-\frac{\alpha(z)}{2}dz}\mathscr{F}^{-1}\left\{e^{-j\frac{\beta_2(z)}{2}(\omega-\omega_0)^2 dz}\mathscr{F}\left\{E(t,z)\right\}\right\} \tag{1.12}$$

where $\mathscr{F}$ and $\mathscr{F}^{-1}$ denote the Fourier and inverse Fourier transform operators, which can generally be computed in the discrete-time using the FFT and inverse FFT algorithms, and $\omega = 2\pi f$ is the angular frequency. This operation is performed until the whole link length is covered.

Note that the SSFM is a serial model of fiber propagation and does not provide a closed-form approximation of the propagated signal. To overcome this, the RP model was proposed [86], implemented with a parallel structure and enabling a closed-form approximation of

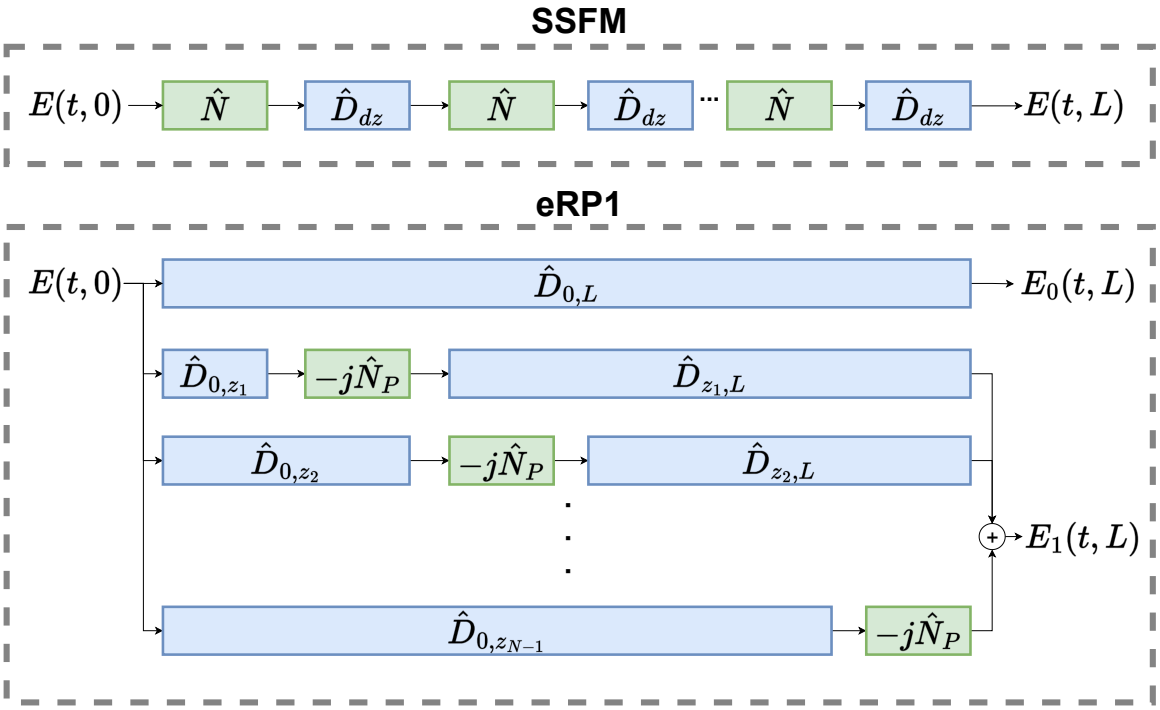

Fig. 1.7 Schematic of SSFM and eRP1 methods. Adapted from: [71].

the signal. While a detailed derivation of the RP method is provided in [86], here only the aspects relevant to this thesis are outlined. In the RP method, the field at time t and position $z = L$ is expressed as

$$E(t,L) = E_0(t,L) + \sum_{m=1}^{\infty} \gamma^m E_m(t,L) \tag{1.13}$$

where the first term denotes the unperturbed solution of the NLSE, incorporating only linear impairments, the second term the nonlinear perturbation and L the total link length. A good approximation is achieved by truncating this perturbation term at the first order, i.e., $E(t,L) = E_0(t,L) + \gamma E_1(t,L)$. Each term can be written as

$$E_0(t,L) = h_{0,L}(t) * E(t,0) \tag{1.14}$$

$$E_1(t,L) = -j \int_0^L h_{z,L}(t) * \hat{N}_0 \left\{ h_{0,z}(t) * E(t,0) \right\} dz \tag{1.15}$$

where $h_{z_i,z_j}(t)$ denotes the linear operation impulse response from arbitrary positions z_i to z_j along the link, $*$ the convolution operator and $\hat{N}_0\{\cdot\} = |\cdot|^2(\cdot)$ the nonlinear operator. An enhanced version, referred to as eRP [86, 87], has also been proposed. In this formulation,

the nonlinear operator is defined as $\hat{N}_P\{\cdot\} = \left[|\cdot|^2 - 2P(z)\right](\cdot)$ for the single polarization case and $\hat{N}_P\{\cdot\} = \left[|\cdot|^2 - \frac{3}{2}P(z)\right](\cdot)$ for the dual-polarization case, where $P(z)$ denotes the power evolution of the propagating signal. In the following, only the first-order RP model will be considered, referred to as RP1 (or eRP1 for its enhanced version). A visualization of the two methods is provided in Fig. 1.7, where the notation $\hat{D}_{z_i,z_j}\{\cdot\} = h_{z_i,z_j}(t) * (\cdot)$ is used to establish a parallelism with the SSFM, with $z = 0,\ldots,z_k,\ldots,L$ and $k = 1,\ldots,N-1$.

1.4.3 Linear Least Squares Method

The starting point of this method is to concentrate the entire contribution of power evolution into a single parameter within the NLSE described by (1.9). This is achieved by introducing the amplitude-normalized optical field, defined as $A(t,z) = E(t,z)\exp\left(\frac{1}{2}\int_0^z \alpha(z')dz'\right)$. This field has constant power while propagating and, inserting it into (1.9), it is possible to rewrite the equation as

$$\frac{\partial}{\partial z}A(t,z) = j\frac{\beta_2(z)}{2}\frac{\partial^2}{\partial t^2}A(t,z) - j\gamma'(z)\,|A(t,z)|^2 A(t,z) \tag{1.16}$$

where all the information about signal power evolution $P(z)$ is contained in $\gamma'(z) = \gamma P(z)$, if we assume γ to be constant over the fiber link. Thus, estimating $\gamma'(z)$ allows to estimate $P(z)$ as well. Let us now consider the discrete-time version of the received signal, i.e., $\mathbf{A}[L] = [A[0,L],\ldots,A[n,L],\ldots,A[N,L]]^T$, with $n = t/T_s$, T_s the sampling period and $(\cdot)^T$ the transpose operator. Also, it is possible to write $\boldsymbol{\gamma}' = \left[\gamma'_0,\ldots,\gamma'_{K-1}\right]^T$, with $\gamma'_k = \gamma'(z_k)$ and z_k the position on the link for $k = 0,\ldots,K-1$. $\boldsymbol{\gamma}'$ is estimated as the set of parameters of a virtual transmission link that best emulate the actual transmission link. In this optimization problem, the transmitted (or reference) signal and the received signal act as boundary conditions. The problem can be formulated as

$$\hat{\boldsymbol{\gamma}}' = \underset{\boldsymbol{\gamma}'}{\operatorname{argmin}}\ \mathbb{E}\left[\|\mathbf{A}[L] - \mathbf{A}_{\text{ref}}[L]\|^2\right] \tag{1.17}$$

where $\mathbb{E}(\cdot)$ denotes the expected value operator and $\mathbf{A}_{\text{ref}}[L]$ is the virtually-propagated reference signal. In the original implementation of MMSE-based LPM [63], the virtual propagation to compute $\mathbf{A}_{\text{ref}}[L]$ was carried out using the SSFM. Since the nonlinear step in (1.11) constitutes a nonlinear operation, the optimization of $\boldsymbol{\gamma}'$ in (1.17) is also a nonlinear problem and was solved through iterative processing based on stochastic gradient descent. A solution is to resort to the eRP1 model [66], that allows to approximate the received

and reference signals as $\mathbf{A}[L] \simeq \mathbf{A}_0[L] + \mathbf{A}_1[L]$ and $\mathbf{A}_{\text{ref}}[L] \simeq \mathbf{A}_{0,\text{ref}}[L] + \mathbf{A}_{1,\text{ref}}[L]$. Assuming $\mathbf{A}_0[L] \simeq \mathbf{A}_{0,\text{ref}}[L]$, (1.17) becomes

$$\hat{\gamma}' = \underset{\gamma'}{\text{argmin}}\, \mathbb{E}\left[\|\mathbf{A}_1[L] - \mathbf{A}_{1,\text{ref}}[L]\|^2\right] \tag{1.18}$$

Moreover, $\mathbf{A}_{1,\text{ref}}[L]$ can be rewritten according to (1.15) as

$$\mathbf{A}_{1,\text{ref}}[L] = \sum_{k=0}^{K-1} \gamma'_k(-j\Delta z_k)\hat{D}_{z_k,L}\left\{\hat{N}_P\left\{\hat{D}_{0,z_k}\left\{\mathbf{A}_{\text{ref}}[0]\right\}\right\}\right\} \tag{1.19}$$

where $\Delta z_k = z_{k+1} - z_k$. This operation allows to isolate the terms γ'_k

$$\mathbf{A}_{1,\text{ref}}[L] = \sum_{k=0}^{K-1} \gamma'_k \cdot g[z_k, n] \tag{1.20}$$

which can be rewritten in matrix form as $\mathbf{A}_{1,\text{ref}}[L] = \mathbf{G}\boldsymbol{\gamma}'$, where $(G)_{nk} = g[z_k, n]$. Substituting this expression in (1.18) yields

$$\hat{\gamma}' = \underset{\gamma'}{\text{argmin}}\, \mathbb{E}\left[\|\mathbf{A}_1[L] - \mathbf{G}\boldsymbol{\gamma}'\|^2\right] \tag{1.21}$$

This optimization problem is an LLS optimization problem and its solution exists in closed-form

$$\hat{\gamma}' = \left(\text{Re}\left[\mathbf{G}^\dagger\mathbf{G}\right]\right)^{-1}\text{Re}\left[\mathbf{G}^\dagger\mathbf{A}_1[L]\right] \tag{1.22}$$

where $\text{Re}[\cdot]$ and $(\cdot)^\dagger$ denote the real part and Hermitian transpose operators, respectively. This derivation can be easily extended to dual-polarization scenario [66], where the NLPR expression becomes $\gamma'(z) = \frac{8}{9}\gamma P(z)$.

In summary, (1.22) provides a closed-form estimation of the power profile evolution of a signal propagating over an optical link, based on the received signal and a reference signal reconstructed from the originally transmitted waveform. A schematic representation of the main steps of LLS-based LPM is provided in Fig. 1.8.

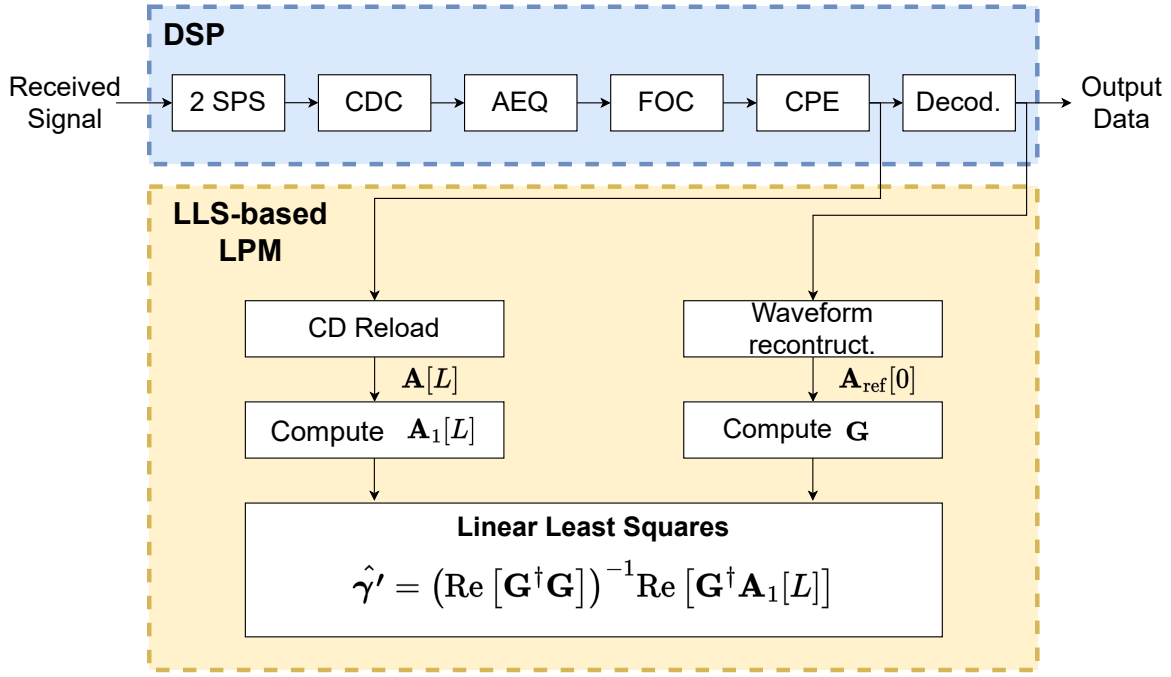

Fig. 1.8 Schematic view of the LLS-based LPM algorithm and relevant DSP blocks. SPS: sample-per-symbol, CDC: CD compensation, AEQ: adaptive equalizer, FOC: frequency offset compensaiton, CPE: carrier phase estimation. Adapted from: [66].

1.4.4 Correlation Method

The second technique for power profile estimation is the CM-based LPM. The principle is similar to the previous method: at the receiver, each polarization component is processed along two parallel paths. In the first path, the signal is processed through the standard DSP chain of a coherent receiver, and after adaptive equalization the output is extracted and fed to the CM-based algorithm. At this stage, the previously compensated CD is reloaded and then partially compensated by an amount $k\Delta c$, where Δc denotes the CD resolution, $k = 0, \ldots, K$, and K is the number of sections into which the optical link is divided. Each of these operations corresponds to compensating a CD equivalent to back-propagating from position $z = L$ to $z = L - z_k$ on the link, where $z_k = k\Delta c/D$, with D being the CD parameter. If we denote $E_i[n]$ as the output of the adaptive equalizer, with $i \in \{x, y\}$ indicating the two polarizations, we can write the output of this first operation as

$$e_i[n] = \hat{D}_{L,L-z_k}\{E_i[n]\}, \quad i \in \{x, y\} \tag{1.23}$$

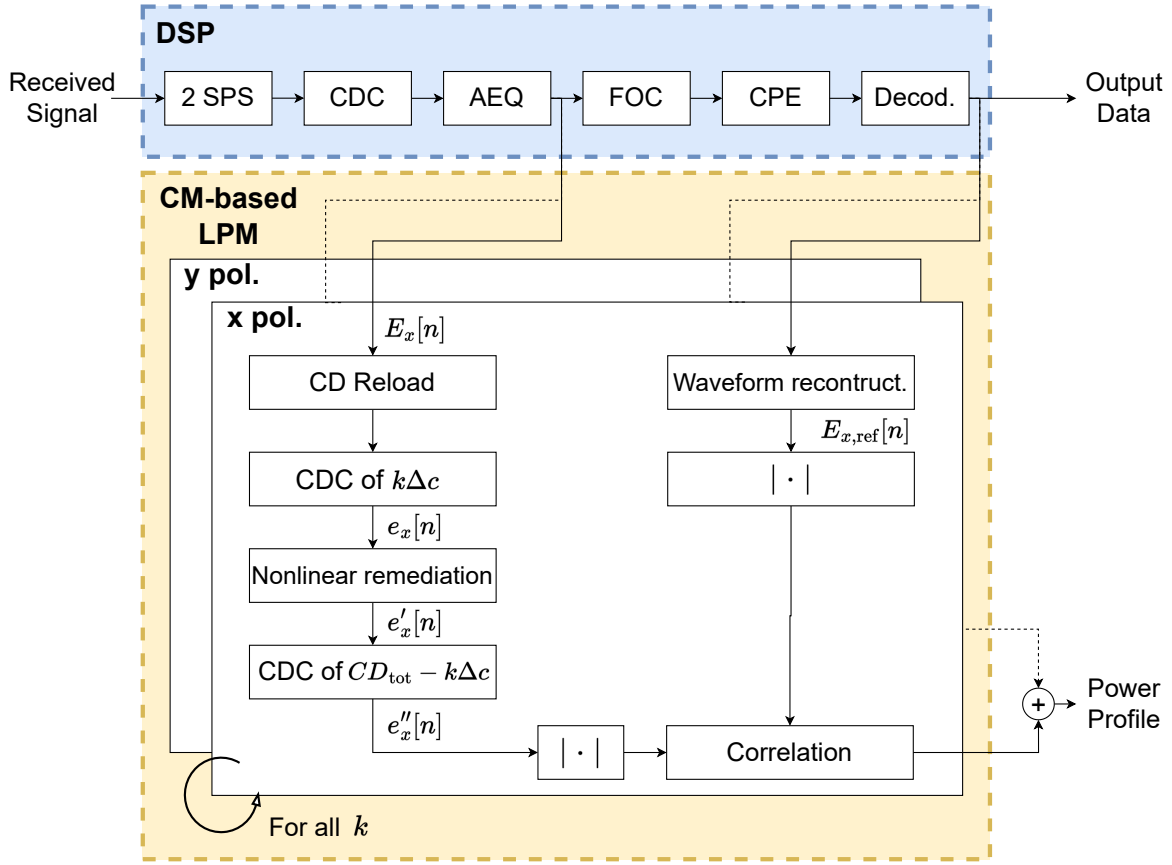

Fig. 1.9 Schematic view of the CM-based LPM algorithm and relevant DSP blocks. Adapted from: [59].

After the first partial CD compensation, a partial nonlinear remediation is applied to the resulting signal to compensate the point-wise nonlinear phase noise. Note that for this operation the nonlinear remediation parameter ε is set to a fixed and small constant value. The signal then becomes

$$e'_i[n] = e_i[n] \exp\left(-j\varepsilon\left(|e_x[n]|^2 + \left|e_y[n]\right|^2\right)\right), \quad i \in \{x,y\} \tag{1.24}$$

Finally, the remaining CD is also compensated

$$e''_i[n] = \hat{D}_{L-z_k,0}\left\{e'_i[n]\right\}, \quad i \in \{x,y\} \tag{1.25}$$

The output of this final step is used to estimate the power value by performing correlation (e.g., computing the Pearson correlation coefficient) with a reference signal $E_{\text{i,ref}}[n]$, with $i \in \{x,y\}$. The correlation output serves as an indicator of the local nonlinear optical power

at that position. This quantity depends on both the instantaneous optical power and the nonlinear refractive index of the fiber at the same location.

$$\hat{\gamma}'_k = \mathrm{corr}\left(|e''_x[n]|, |E_{x,\mathrm{ref}}[n]|\right) + \mathrm{corr}\left(|e''_y[n]|, |E_{y,\mathrm{ref}}[n]|\right) \tag{1.26}$$

To reconstruct the full power profile, this procedure must be repeated for all possible values of k. Since the signal is extracted before the FOC and CPE operations, the absolute value of both signals is considered. Furthermore, the structure of this version of the algorithm remains influenced by the DBP. An alternative approach, presented in [61] and often referred to as modified CM-based LPM, instead performs correlations between the received signal and each nonlinear branch of the RP1 model (see Fig. 1.7) applied to the reference signal. Also for the CM-based algorithm a visual representation of the main steps is reported in Fig. 1.9.

1.5 Optical Fiber Sensing

Another possible monitoring application is optical fiber sensing. With the widespread deployment of optical fiber networks across terrestrial and submarine environments, there is growing interest in leveraging these infrastructures for environmental sensing. Monitoring external natural and human-induced activities is important not only for public safety but also for protecting the integrity of the fiber itself. Environmental perturbations can lead to issues like fiber cuts, threatening network reliability. Real-time sensing enables early detection of such anomalies, supports hazard mitigation near fiber routes, and helps reduce the risk of costly outages or infrastructure damage.

1.5.1 Length-integrated Sensing Technologies

Length-integrated sensing technologies, which do not offer event localization, represent one category of fiber sensing methods. Among these, polarization-based sensing stands out by utilizing the inherent capability of modern coherent receivers to estimate the state of polarization (SOP) for signal demodulation. This makes it possible to implement polarization-based sensing with minimal added cost and complexity, as it can operate directly on existing telecommunication transceivers [88].

External perturbations, such as mechanical vibrations, temperature fluctuations, and electromagnetic interference, induce stress and geometrical deformations in the fiber, leading

to time-varying birefringence and SOP fluctuations. These changes can be monitored to detect natural events such as earthquakes and debris flows, as well as human-induced activities like construction work and tampering [88–90]. While polarization-based sensing does not inherently provide localization capabilities, as the SOP is an integrated parameter along the fiber, it extends the potential sensing range compared to distributed methods (discussed in the following), which are typically limited to around 100 km.

Recent studies have demonstrated polarization sensing across a variety of environments and fiber lengths, from short urban links to submarine spans of over 10,000 km. Events detected include mechanical vibrations, wind gusts, lightning strikes, and varying magnetic fields due to power lines [90–92]. For instance, ultra-low-frequency seismic events have been successfully detected with sampling rates as low as 100 S/s, using SOP data extracted from either polarimeters or directly from coherent receiver telemetry [92–94].

Despite its advantages, polarization sensing faces limitations in terms of localization. Since SOP is not spatially resolved, techniques based on cross-correlation between signals received at opposite ends of a fiber have been proposed [95]. These methods rely on detecting the time delay of a disturbance propagating through the fiber. Alternative strategies involve using different wavelengths in high-dispersion fibers to exploit time-of-arrival differences at a single receiver [96]. However, such approaches are sensitive to sampling rate, noise, and the spectral content of the perturbation itself.

SOP sensing accuracy is also affected by estimation noise from the receiver. Experimental work has shown that coherent receivers, though not optimized for polarization tracking, can still provide usable SOP data, particularly at higher OSNRs and with adequate signal smoothing, as will be discussed in Chapter 4. Conversely, real-world noise sources, such as environmental changes in metropolitan settings, introduce non-stationary SOP fluctuations over long periods [97]. As a result, hazard detection algorithms must be robust to these dynamics.

One basic method, SOP angular speed (SOPAS), calculates the angular rate of SOP variation between successive samples. While effective in controlled environments, SOPAS is sensitive to baseline fluctuations and unsuitable for non-stationary environments. To overcome this, a more adaptive algorithm called SOP - power spectral density gap (SOP-PSDG) was developed, which normalizes spectral deviations relative to a moving reference window. This approach offers improved sensitivity and a more stable thresholding baseline, enhancing reliability for real-time monitoring applications [98]. An example of these quantities is reported in Fig. 1.10.

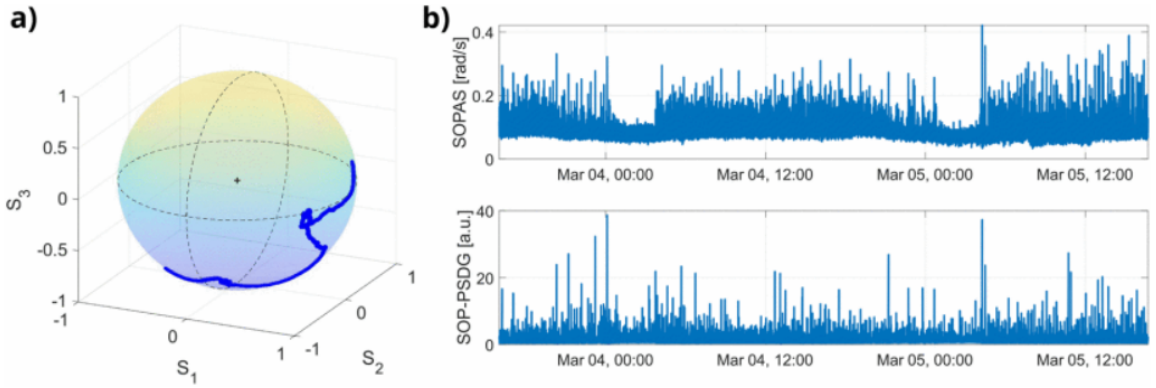

Fig. 1.10 a) SOP evolution over the Poincaré sphere surface over around two days of acquisition, considering a metropolitan fiber. b) Same acquisition, but the SOPAS and SOP-PSDG time evolutions are shown.

Overall, polarization-based sensing presents a promising and cost-efficient technique for leveraging existing optical fiber infrastructure to monitor environmental and security threats, with ongoing developments focused on enhancing accuracy, localization, and robustness to noise. It is worth noting that alternative approaches exist. For instance, optical phase-based sensing has been proposed [93], and its performance relative to polarization-based sensing will be analyzed in Chapter 4.

1.5.2 Distributed Sensing Technologies

Distributed fiber optic sensing (DFOS) enables the use of optical fiber infrastructure for simultaneous data transmission and environmental sensing, leveraging backscattering mechanisms inherent to the fiber medium, namely Rayleigh, Brillouin, and Raman backscatter, shown in Fig. 1.11. These methods permit spatially continuous measurement of parameters such as vibration, strain, and temperature along the entire fiber length, with spatial resolution dictated by the interrogation signal's bandwidth [99].

Rayleigh-based sensing, particularly for distributed acoustic sensing (DAS), utilizes the detection of Rayleigh backscattered light induced by microscopic inhomogeneities in the glass structure. A short optical pulse is launched into the fiber, and the backscattered signal, varying with strain or vibration, is measured as a function of time to infer spatial variations. The simplest form, intensity-based DAS, detects changes in backscatter amplitude caused by phase interference among scatterers due to dynamic strain. While it does not provide linear reconstruction of the vibration waveform, coherent detection enables phase-sensitive

DAS, which can recover the optical phase shifts induced by strain, thus enabling quantitative vibration measurements [100].

Brillouin-based sensing, implemented through Brillouin optical time-domain reflectometry, is suited for static or quasi-static measurements of temperature and strain. The Brillouin frequency shift of the backscattered light is sensitive to changes in both parameters. The frequency shift is extracted through frequency-domain analysis of the backscattered spectrum, typically using Lorentzian fitting or Fourier transforms. Advanced systems may also use diversity techniques or hybrid Raman/Brillouin setups to decouple temperature and strain contributions [101].

Raman-based sensing, used in distributed temperature sensing, is based on the asymmetric intensity of Stokes and anti-Stokes Raman scattering (see Sec. 2.3.1 for more details on this topic), which is temperature-dependent. The ratio of these components provides a direct estimate of temperature along the fiber. Due to the weak nature of the Raman signal, high-gain detection and temporal averaging are required [102].

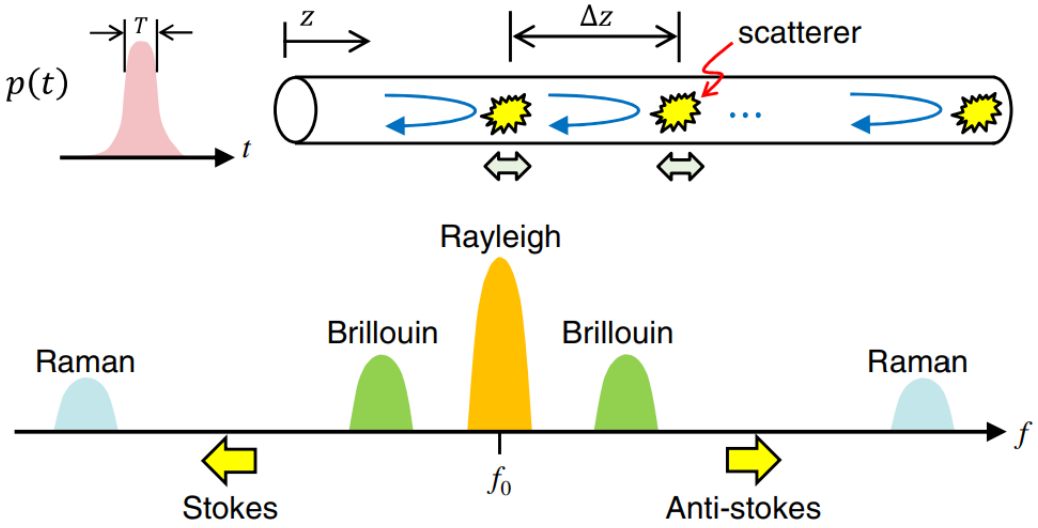

Fig. 1.11 Visualization of main backscattering mechanisms for distributed fiber optic sensing. Source: [99].

Each DFOS method offers distinct advantages. Rayleigh-based DAS is well-suited for high-resolution, real-time vibration monitoring, like the one discussed for polarization-based sensing; Brillouin systems provide accurate strain and temperature measurements over longer distances but with lower temporal resolution; Raman systems offer temperature sensing with high spatial resolution. These techniques can coexist with live data traffic by spectrum multiplexing, allowing telecommunication infrastructure to serve dual purposes. However,

limitations such as the presence of inline amplifiers, optical isolators, and strong reflections may require network modifications for optimal DFOS deployment [103]. Therefore, these techniques are presented here for completeness but will not be examined further in the scope of this thesis.

1.6 Thesis Outline

As highlighted in the introduction, in the context of modern optical networks, characterized by ever-increasing transmission rates, flexible and reconfigurable architectures, and the constant demand for cost-efficient operation, DSP has emerged as a key enabling technology. While its primary role is to support standard transmission and mitigate impairments, it has also proved highly valuable for OPM, leading to the development of DSP-based OPM solutions. Recent advances in this area include DLM, and specifically LPM, which enable spatially-resolved estimation and localization of impairments, as well as the extension of DSP-based OPM to fiber sensing, where existing network infrastructure can be exploited to detect external perturbations, such as vibrations or tampering. In summary, DSP-based OPM provides a scalable and cost-efficient alternative to traditional hardware-based monitoring, as it leverages the processing already available in coherent receivers to extract monitoring information directly from data-carrying signals, making it a crucial tool for the development of future optical networks.

With these motivations and in this context, this thesis investigates innovative OPM solutions, focusing on DLM for coherent optical fiber links and on DSP-based approaches for fiber sensing over metropolitan fiber networks. This thesis is structured as follows. Chapter 2 presents OPM solutions based on LPM for PDL estimation and localization, including a comparison with alternative methods proposed in the literature. This chapter also demonstrates the application of LPM in different transmission scenarios, such as subcarrier multiplexing and UWB transmission (C+L band) with backward Raman amplification. Chapter 3 highlights the intrinsic capability of LPM for simple nonlinear interference estimation, with a focus on transmit power optimization, and concludes with a discussion of the trade-offs involved in its practical implementation along with possible mitigation strategies. Finally, Chapter 4 introduces DSP-based techniques for fiber sensing in metropolitan networks, examining the accuracy of polarization state information extracted from standard coherent DSP and comparing its sensing performance with other DSP-based methods, such as optical phase sensing.

1.7 List of Publications

During the Ph.D. program, the following research contributions were published:

Peer-Reviewed Journal Articles

1. L. Andrenacci, G. Bosco and D. Pilori, "PDL Localization and Estimation Through Linear Least Squares-Based Longitudinal Power Monitoring," in IEEE Photonics Technology Letters, vol. 35, no. 24, pp. 1431-1434, 15 Dec.15, 2023, doi: 10.1109/LPT.2023.3331110;

2. L. Andrenacci, G. Bosco, Y. Jiang, A. Nespola, S. Piciaccia and D. Pilori, "DSP-Based Nonlinear Interference Estimation Using Linear Least Squares Longitudinal Power Monitoring," in Journal of Lightwave Technology, vol. 43, no. 8, pp. 3536-3546, 15 April15, 2025, doi: 10.1109/JLT.2025.3532100.

3. S. Pellegrini, L. Minelli, L. Andrenacci, G. Rizzelli, D. Pilori, G. Bosco, L. Della Chiesa, C. Crognale, S. Piciaccia and R. Gaudino, "Overview on the state of polarization sensing: application scenarios and anomaly detection algorithms," in Journal of Optical Communications and Networking, vol. 17, no. 2, pp. A196-A209, February 2025, doi: 10.1364/JOCN.537881;

4. D. Pilori, S. Straullu, A. Nespola, L. Andrenacci, S. Piciaccia and G. Bosco, "Experimental Demonstration of Longitudinal Power Monitoring Over a Mixed Fiber Link," in IEEE Photonics Technology Letters, vol. 37, no. 20, pp. 1181-1184, 15 Oct.15, 2025, doi: 10.1109/LPT.2025.3590274;

International Conference Proceedings

1. L. Minelli, S. Pellegrini, L. Andrenacci, D. Pilori, G. Bosco, L. D. Chiesa, A. Tanzi, C. Crognale and R. Gaudino, "SOP-based DSP blind anomaly detection for sensing on deployed metropolitan fibers," 49th European Conference on Optical Communications (ECOC 2023), Hybrid Conference, Glasgow, UK, 2023, pp. 519-522, doi: 10.1049/icp.2023.2232.

2. L. Andrenacci, G. Bosco and D. Pilori, "Longitudinal Power Monitoring Performance with Subcarrier Multiplexing Transmission," 2023 IEEE Photonics Conference (IPC), Orlando, FL, USA, 2023, pp. 1-2, doi: 10.1109/IPC57732.2023.10360788;

3. S. Pellegrini, L. Andrenacci, L. Minelli, D. Pilori, G. Bosco, L. Della Chiesa and R. Gaudino, "Estimation Accuracy of Polarization State from Coherent Receivers for Sensing Applications," 2023 IEEE Photonics Conference (IPC), Orlando, FL, USA, 2023, pp. 1-2, doi: 10.1109/IPC57732.2023.10360574;

4. S. Pellegrini, L. Minelli, D. Pilori, G. Bosco, B. Koch, R. Noe, C. Crognale, S. Piciaccia and R. Gaudino, "Real-Time Demonstration of Anomalous Vibrations Detection in a Metro-like Environment using a SOP-based Algorithm," 2024 Optical Fiber Communications Conference and Exhibition (OFC), San Diego, CA, USA, 2024, pp. 1-3;

5. L. Andrenacci, D. Pilori, S. Pellegrini, L. Minelli, G. Bosco, C. Crognale, S. Piciaccia and R. Gaudino, "Comparison between Phase and Polarization Sensing using Coherent Transceivers over Deployed Metro Fibers," 2024 Optical Fiber Communications Conference and Exhibition (OFC), San Diego, CA, USA, 2024, pp. 1-3;

6. S. Pellegrini, G. Rizzelli, L. Andrenacci, L. Minelli, D. Pilori, G. Bosco, C. Crognale, S. Piciaccia, A. Tanzi and R. Gaudino, "Polarization-based Optical Fiber Sensing: A State of the Art Review," 2024 Italian Conference on Optics and Photonics (ICOP), Firenze, Italy, 2024, pp. 1-4, doi: 10.1109/ICOP62013.2024.10803652;

7. L. Andrenacci, G. Bosco and D. Pilori, "PDL Localization and Estimation Through Longitudinal Power Monitoring: A Comparison between Least Squares and Correlation Methods," 2024 Italian Conference on Optics and Photonics (ICOP), Firenze, Italy, 2024, pp. 1-4, doi: 10.1109/ICOP62013.2024.10803656;

8. L. Andrenacci, S. Straullu, A. Nespola, G. Bosco, P. Poggiolini, S. Piciaccia and D. Pilori, "Experimental Demonstration of Linear Least Squares-based Longitudinal Power Monitoring over a Raman-amplified C+L Link," ECOC 2024; 50th European Conference on Optical Communication, Frankfurt, Germany, 2024, pp. 503-506;

9. S. Pellegrini, G. Rizzelli, L. Minelli, L. Andrenacci, D. Pilori, G. Bosco, C. Crognale, S. Piciaccia and R. Gaudino, "SOP-based Sensing for Detecting Different Anomalous Events: Practical Implementation Considerations," ECOC 2024; 50th European Conference on Optical Communication, Frankfurt, Germany, 2024, pp. 1952-1955;

10. L. Andrenacci, G. Bosco, Y. Jiang, A. Nespola, S. Straullu, S. Piciaccia and D, Pilori, "Nonlinear Noise Estimation using Linear Least Squares-based Longitudinal Power Monitoring," ECOC 2024; 50th European Conference on Optical Communication, Frankfurt, Germany, 2024, pp. 172-175;

11. L. Andrenacci, A. Nespola, S. Straullu, Y. Jiang, S. Piciaccia, G. Bosco and D. Pilori, "Implementation Penalties for Nonlinear Interference Estimation with Linear Least Squares Longitudinal Power Monitoring," 2025 Optical Fiber Communications Conference and Exhibition (OFC), San Francisco, CA, USA, 2025, pp. 1-3.

12. G. Bosco, L. Andrenacci, A. Nespola, S. Straullu, Y. Jiang, S. Piciaccia and D. Pilori, "DSP-Based Nonlinear SNR Estimation via Longitudinal Power Monitoring in Commercial Coherent Receivers," 2025 25th Anniversary International Conference on Transparent Optical Networks (ICTON), Barcelona, Spain, 2025, pp. 1-5, doi: 10.1109/ICTON67126.2025.11125018.

13. D. Pilori, L. Andrenacci, and G. Bosco, "Estimating the Nonlinear Interference at the Receiver: Methods and Pitfalls," in Advanced Photonics Congress (IPR, Networks, NOMA, SOLITH, SPPCom) , Technical Digest Series (Optica Publishing Group, 2025), paper SpTh2F.3.

14. L. Andrenacci, G. Caruso, I. N. Cano, Y. Zhicheng, G. Rizzelli, G. Talli, G. Bosco and R. Gaudino, "CD Pre-Compensated Tx with ODB Modulation and Direct Detection Rx for VHSP Downstream," ECOC 2025, Copenhagen, Denmark, 2025, W.03.07.1.

Chapter 2

Digital Longitudinal Monitoring of Long-Haul Transmission Systems

This chapter explores innovative optical performance monitoring techniques in the context of digital longitudinal monitoring, with corresponding simulative evaluations and, where possible, experimental validations. The central theme is the development and validation of LPM-based methods and their applicability to diverse transmission scenarios:

- **Multi-span transmission affected by PDL:** Sec. 2.1 presents a modification of the LLS-based LPM algorithm for polarization-dependent loss estimation and localization, along with a comparative analysis against an alternative method relying on CM-based LPM. Reference works:
  - L. Andrenacci, G. Bosco and D. Pilori, "PDL Localization and Estimation Through Longitudinal Power Monitoring: A Comparison between Least Squares and Correlation Methods," 2024 Italian Conference on Optics and Photonics (ICOP), Firenze, Italy, 2024, pp. 1-4, doi: 10.1109/ICOP62013.2024.10803656;
  - L. Andrenacci, G. Bosco and D. Pilori, "PDL Localization and Estimation Through Linear Least Squares-Based Longitudinal Power Monitoring," in IEEE Photonics Technology Letters, vol. 35, no. 24, pp. 1431-1434, 15 Dec.15, 2023, doi: 10.1109/LPT.2023.3331110;
- **Digital subcarrier multiplexing systems:** Sec. 2.2 demonstrates the use of LPM in subcarrier multiplexing systems, assessing its effectiveness in multi-carrier environments. Reference works:

  - L. Andrenacci, G. Bosco and D. Pilori, "Longitudinal Power Monitoring Performance with Subcarrier Multiplexing Transmission," 2023 IEEE Photonics Conference (IPC), Orlando, FL, USA, 2023, pp. 1-2, doi: 10.1109/IPC57732.2023.10360788;

- **UWB transmission with full backward Raman amplification:** Sec. 2.3 investigates the feasibility and accuracy of LPM in UWB transmission systems employing full backward Raman amplification. Reference works:

  - L. Andrenacci, S. Straullu, A. Nespola, G. Bosco, P. Poggiolini, S. Piciaccia and D. Pilori, "Experimental Demonstration of Linear Least Squares-based Longitudinal Power Monitoring over a Raman-amplified C+L Link," ECOC 2024; 50th European Conference on Optical Communication, Frankfurt, Germany, 2024, pp. 503-506;

2.1 Polarization-Dependent Loss Estimation and Localization

Polarization-dependent loss is a significant physical impairment in modern optical communication systems [104]. It refers to the variation in signal attenuation as a function of the state of polarization (SOP) of impinging light, meaning that different polarization states experience different levels of loss while propagating through the same optical path and, possibly, a loss of orthogonality [105]. A representation of the effect of PDL on an optical signal is illustrated in Fig. 2.1. PDL primarily stems from optical components along the link, such as wavelength-selective switches (WSSs) in ROADMs or EDFAs [106]. Furthermore, these optical components may induce PDL whose impact varies with parameters such as time or wavelength. As a result, PDL behaves as a stochastic impairment, which is particularly challenging to manage in networks containing multiple ROADMs, where the accumulated PDL can reach values of about 2-3 dB [107], thus requiring large design margins during network operation [40]. Such variability also results in fluctuations in signal quality, impacting both the OSNR and the overall system throughput. Since the SOP evolves unpredictably along the fiber due to environmental influences and imperfections in optical components, PDL emerges as a critical impairment that is difficult to control. Effectively monitoring PDL is therefore vital to maintain optimal network performance and guarantee reliable, high-quality data transmission.

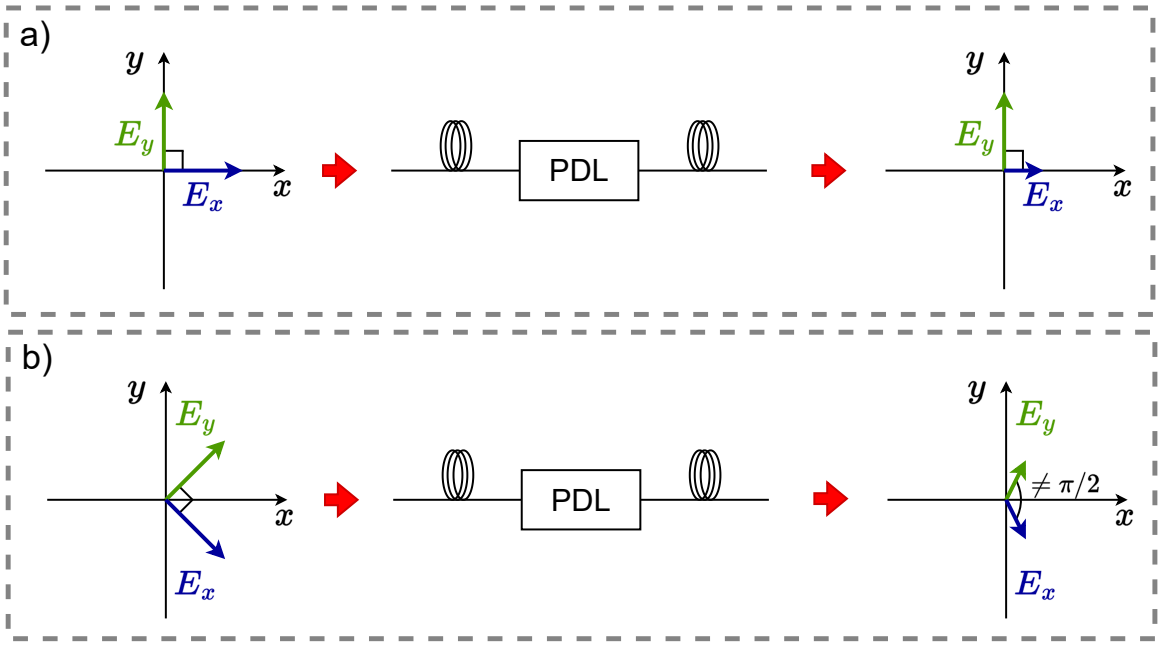

Fig. 2.1 Representation of polarization-dependent loss effect on a signal with a) x-polarization aligned ($\theta = 0$) with maximum PDL axis and b) x- and y-polarization at $\theta = \pi/4$ with respect to maximum PDL axis.

2.1.1 Modeling and Monitoring of Polarization-Dependent Loss

As mentioned before, PDL generally introduces different attenuation levels to the two polarization components of an optical signal. This effect can be readily modeled using Jones matrix formalism [108]. Let us consider a Jones vector $\mathbf{E}_{\text{in}} = [E_x, E_y]^T$ representing the optical field incident on a PDL element. The corresponding output field $\mathbf{E}_{\text{out}}$, neglecting losses/gains common to both polarizations and not affecting PDL, can then be generally expressed as

$$\mathbf{E}_{\text{out}} = \mathbf{H}_{\text{PDL}}\mathbf{E}_{\text{in}} \tag{2.1}$$

with

$$\mathbf{H}_{\text{PDL}} = \mathbf{R}^{-1}(\theta,\phi)\mathbf{H}\mathbf{R}(\theta,\phi) \tag{2.2}$$

where $\mathbf{H}$ denotes the matrix responsible for introducing power imbalance between the two polarizations, and $\mathbf{R}(\theta,\phi)$ is a unitary matrix that defines the PDL axes through the angles θ and ϕ. The inclusion of $\mathbf{R}(\theta,\phi)$ accounts for the fact that, in general, optical signals impinge on a PDL element with a random SOP, which is not aligned with the PDL axes. In particular,

it can be written as [109]

$$\mathbf{R}(\theta,\phi) = \begin{pmatrix} \cos(\phi) & j\sin(\phi) \\ -j\sin(\phi) & \cos(\phi) \end{pmatrix} \begin{pmatrix} \cos(\theta) & \sin(\theta) \\ -\sin(\theta) & \cos(\theta) \end{pmatrix}. \tag{2.3}$$

Matrix $\mathbf{H}$, on the other hand, can be modeled in two different ways depending on the behavior of the component introducing PDL. The loss can be applied to one polarization only, i.e.,

$$\mathbf{H} = \begin{pmatrix} 1 & 0 \\ 0 & \varepsilon \end{pmatrix}. \tag{2.4}$$

where $\varepsilon \in [0,\ 1]$ and the PDL value is given by $\mathrm{PDL_{dB}} = 10\log_{10}(\varepsilon^2)$. Note that this model introduces an energy loss at the output of the PDL element, since $\mathrm{Tr}\left(\mathbf{H}\mathbf{H}^{\dagger}\right) = 1+\varepsilon^2$, with $\mathrm{Tr}(\cdot)$ the matrix trace operator. The matrix can also be modeled as

$$\mathbf{H} = \begin{pmatrix} \sqrt{1+\varepsilon} & 0 \\ 0 & \sqrt{1-\varepsilon} \end{pmatrix}. \tag{2.5}$$

where $\varepsilon \in [0,\ 1]$ and $\mathrm{PDL_{dB}} = 10\log_{10}\left((1+\varepsilon)/(1-\varepsilon)\right)$. In this formulation, energy conservation is assumed, i.e., $\mathrm{Tr}\left(\mathbf{H}\mathbf{H}^{\dagger}\right) = 2$.

However, multiple PDL elements may be present along an optical link. In this case, and neglecting noise contributions for simplicity, the overall PDL matrix representing the accumulation of N individual PDL elements can be expressed as

$$\mathbf{H}_{\mathrm{PDL}} = \prod_{n=1}^{N} \mathbf{H}_{\mathrm{PDL}.n} \tag{2.6}$$

which indicates that a link with distributed PDL can be modeled as a single PDL element, whose equivalent PDL value can be computed resorting to the singular value decomposition (SVD) of (2.6).

A variety of methods have been proposed in the literature for PDL monitoring. Among them, one approach [12, 42], already discussed in Sec. 1.3.2, exploits the PDL models in (2.2) and (2.6) to extract PDL information from the taps of the adaptive equalization stage in the DSP of a coherent optical receiver. Other techniques include SOP-based monitoring schemes [110] and amplitude-modulated pilot-tone methods [111, 112]. Further approaches rely on statistical modeling of PDL [113, 114], where regression techniques are applied to

fluctuations in the SNR distribution to infer the PDL contribution introduced by network components [115].

However, these methods generally do not enable simultaneous localization and estimation of PDL. To address this limitation, DLM, and in particular LPM, offers a promising alternative. LPM provides an estimate of the longitudinal power profile evolution of an optical signal along the fiber. Since PDL is inherently a power-related impairment, the potential ability of LPM to recover polarization-resolved power profiles would make it possible to both localize and estimate PDL. Research in this direction has already been conducted using CM-based LPM. For example, [116] demonstrates PDL localization in a multi-span transmission relying solely on receiver-side DSP. However, estimation could not be achieved, since CM-based LPM does not provide absolute power values [71]. This limitation was subsequently overcome by introducing a calibration procedure applied to the CM power profiles, which enabled PDL estimation with high accuracy at the cost of additional complexity and reduction in flexibility.

A more direct approach to jointly estimate and localize PDL is to introduce suitable modifications to the LLS-based LPM algorithm, enabling it to operate in a polarization-resolved manner. This solution is presented in the following. In parallel to this work, a similar approach was proposed in [117]. While the underlying principle is the same, the implementation differs. The method proposed in this thesis modifies the nonlinear operator of the eRP1 model and performs two separate power profile estimations, one for each polarization. In contrast, the approach in [117] modifies the computation of the matrix $\mathbf{G}$ in (1.22), doubling its size to account for cross-polarization contributions.

2.1.2 Joint Localization and Estimation through Linear Least Squares-based Longitudinal Power Monitoring

The LLS-based LPM algorithm was introduced in Sec. 1.4.3 for the single-polarization case. Since PDL affects both polarizations, it is necessary to extend the analysis to the dual-polarization scenario. The LLS optimization problem in (1.21) for estimating the total signal power profile essentially remains unchanged, but it can be reformulated to explicitly highlight the polarization-wise contributions as

$$\hat{\boldsymbol{\gamma}} = \underset{\boldsymbol{\gamma}}{\operatorname{argmin}}\, \mathbb{E}\left[\left\| \begin{bmatrix} \mathbf{A}_{1,x}[L] \\ \mathbf{A}_{1,y}[L] \end{bmatrix} - \begin{bmatrix} \mathbf{G}_x \\ \mathbf{G}_y \end{bmatrix} \boldsymbol{\gamma} \right\|^2\right] \tag{2.7}$$

where each matrix $\mathbf{G}i$ can be computed from (1.19) using the corresponding polarization-wise reference signal $\mathbf{A}_{\text{ref},i}$, with $i \in x,y$. Ultimately, however, the LLS solution in (1.22) provides an estimate of the total power profile, given the problem formulation and the eRP1 nonlinear operator employed, i.e., $\hat{N}_P\{\cdot\} = \left[\|\cdot\|^2 - \frac{3}{2}\right](\cdot)$. Since the algorithm operates on the normalized amplitude field, the term $P(z) = 1$ can be assumed.

The proposed method, instead, separates the contributions of the two polarizations by splitting the optimization into two independent problems, one for the x polarization and one for the y polarization, while modifying the nonlinear term to its single-polarization form, similarly to the CM-based approach presented in [109]. Hence, each column of the $\mathbf{G}_i$ matrices can be expressed as

$$g_i[z_k,n] = \sum_{k=0}^{K-1}(-j\Delta z_k)\hat{D}_{z_k,L}\left\{\hat{N}_P\left\{\hat{D}_{0,z_k}\left\{\mathbf{A}_{\text{ref},i}[0]\right\}\right\}\right\},\ \ i \in \{x,y\} \tag{2.8}$$

where all the symbols have the same meaning as in Sec. 1.4.3 and the nonlinear operator is substituted with $\hat{N}_P\{\cdot\} = \left[|\cdot|^2 - 2\right](\cdot)$. Finally, this allows to compute the polarization-wise longitudinal power profiles as

$$\hat{\gamma}_i = \left(\text{Re}\left[\mathbf{G}_\text{i}^\dagger \mathbf{G}_\text{i}\right]\right)^{-1}\text{Re}\left[\mathbf{G}_i^\dagger \mathbf{A}_{1,i}[L]\right],\ i \in \{x,y\} \tag{2.9}$$

In summary, a minor modification to the original algorithm enables the estimation of polarization-resolved power profiles.

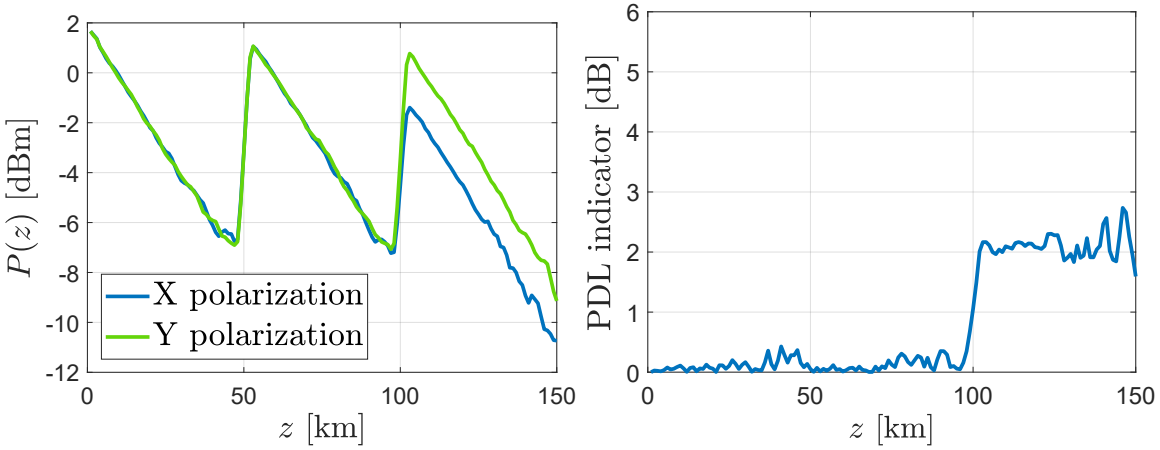

Fig. 2.2 Example of polarization-wise power profiles estimated with the proposed method (left) and corresponding indicator for subsequent PDL estimation and localization (right).

It should be noted that the effect of PDL is stochastic, as the SOP of the incoming optical signal may vary over time. For this reason, to obtain a true estimate of PDL, defined as the ratio between the maximum and minimum losses experienced across all possible SOPs, it is necessary to evaluate multiple profiles while varying the SOP of the input signal to the LPM algorithm. For each position along the link, a PDL indicator can then be computed as the ratio between the maximum and minimum values of the power profile at that location. An example of this procedure is illustrated in Fig. 2.2 for a nominal PDL value of 2 dB inserted at the beginning of the third span in a simple simulation setup composed of 3×50-km SMF spans. The two power profiles correspond to the two input states of polarization that maximize the PDL, among all possible SOPs. The effectiveness of this approach is evaluated in the following section through numerical simulations.

2.1.3 Numerical Validation of Proposed Method

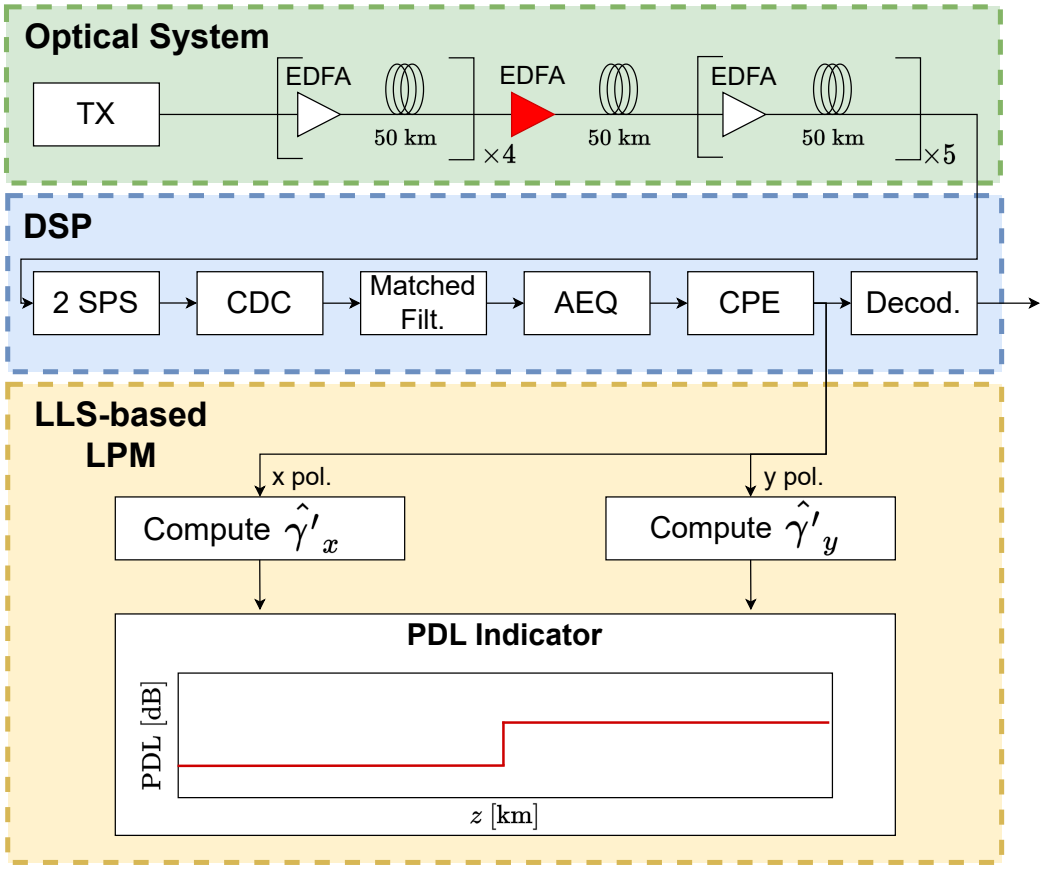

Fig. 2.3 Schematic of the simulation setup and the LLS-based PDL estimation algorithm, with the PDL element highlighted in red.

The simulation setup in Fig. 2.3 is used to validate the proposed method. The transmitted signal consists of three dual polarization (DP)-64QAM WDM channels shaped by a square-root raised-cosine filter with roll-off 0.15, modulated at 128 GBaud, and spaced by 200 GHz. A large channel spacing is adopted in order to minimize the contribution of XCI and to focus on PDL estimation, while also reducing the simulation time. Although a denser channel spacing would introduce additional measurement noise, a detailed analysis of its impact is beyond the scope of the present analysis and is left for future work. The central channel is taken as the channel under test (CUT). The optical link consists of 10×50 km identical spans of G.652 single-mode fibers (SMFs), characterized by an attenuation of $\alpha_{\mathrm{dB}} = 0.2\,\mathrm{dB/km}$, a chromatic dispersion coefficient of $\beta_2 = -21.28\,\mathrm{ps}^2/\mathrm{km}$, and a nonlinearity coefficient of $\gamma = 1.3\,1/\mathrm{W/km}$. Each span is followed by an EDFA with a noise figure of 5 dB, operated in constant output power mode.

The algorithm's performance was evaluated by inserting lumped PDL elements into the optical link, modeled according to the formulation in (2.5). In the simulations, fiber propagation is modeled using the split-step Fourier method, implementing the Manakov equation [85]. After propagation, the optical signal is received by a standard coherent receiver and sampled at a rate of two sample-per-symbol. The resulting samples are then processed by several DSP blocks performing CD compensation, matched filtering, LMS-based adaptive equalization, and BPS carrier phase estimation. The output of the final DSP stage is extracted and used as the input to the LPM algorithm. Each power profile is computed from approximately 8×10^5 samples. In the simulations, the reference signal for LPM is reconstructed directly from the transmitted sequence. In practice, however, this reconstruction would typically be carried out after error-free forward error correction (FEC) decoding, which was not implemented in this work, or hard-decision before FEC.

The initial analysis considered the estimation of the location of a lumped 3-dB PDL element inserted at the beginning of the 5-th span, emulating a faulty WSS placed after the EDFA. The estimation was performed under three different operating conditions. First, the algorithm was tested at a high transmit power of 8 dBm, as in [116]. It was then assessed at lower power levels of 5 and 2 dBm, the latter corresponding to the launch power that maximizes the overall SNR, as illustrated in Fig. 2.4. This approach also allows to test the algorithm under conditions where LPM is less effective, such as at low per-channel power, due to its reliance on nonlinear effects that are inherently power-dependent.

For each operating condition, 20 power profiles were estimated using a constant spatial step of $\Delta z = 2$ km in the LPM algorithm. In each case, the SOP of the transmitted signal was randomly rotated digitally at the transmitter, while the polarization-rotation elements within

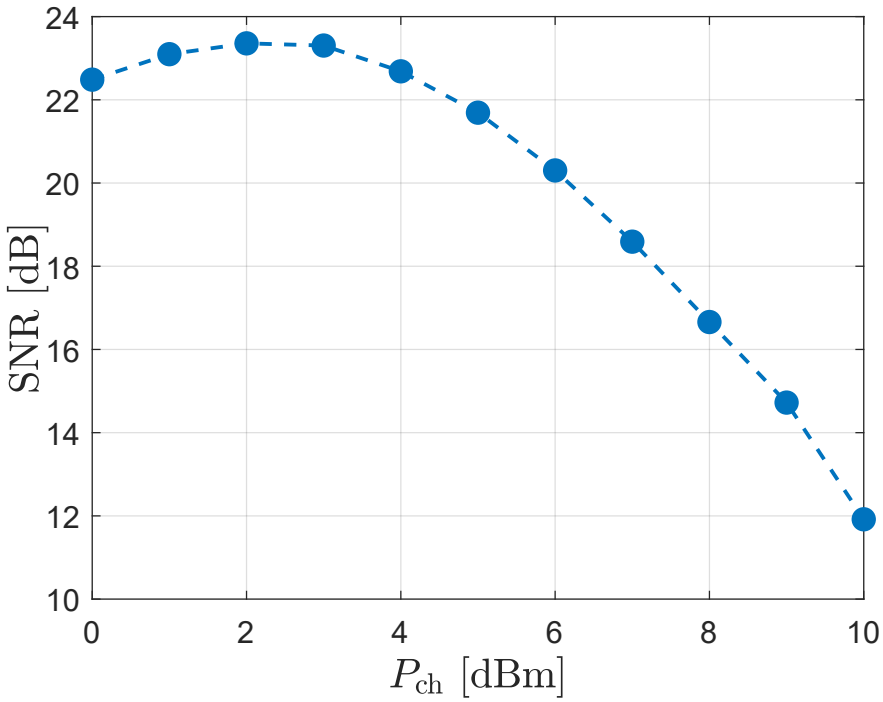

Fig. 2.4 SNR vs per-channel power for the considered setup. Optimum power around 2 dBm.

the link were kept fixed. This reflects the assumption that, in a realistic scenario, the incident SOP at the PDL elements remains relatively stable over time.

Figure 2.5 shows all the x-polarization profiles computed for a transmit power of 2 dBm and corresponding to each simulated SOP of the signal. These profiles display noticeable noise, particularly in the second half of each span. The observed noise is attributed to the LPM algorithm's sensitivity to the level of nonlinearity at the measurement position, as mentioned above: higher nonlinearity generally leads to improved accuracy in the estimation process. Thus, for such applications, it is preferable to operate at a higher power level [71]. To address this issue, a moving average operation has been performed on the estimated profiles, considering a window length of 5 samples. This post-processing step aims to mitigate the estimation noise arising from points in the link where the power is low. By averaging neighboring samples, the algorithm can partially smooth out the noise, leading to more stable and reliable estimations also at low power level, as shown by the following results.

Figure 2.6 shows the PDL indicator at different power levels, defined as the difference between the maximum and minimum values of all profiles at each position z_k. Across all powers, the indicator exhibits a clear rise around $z = 200$ km, reaching approximately 3 dB.

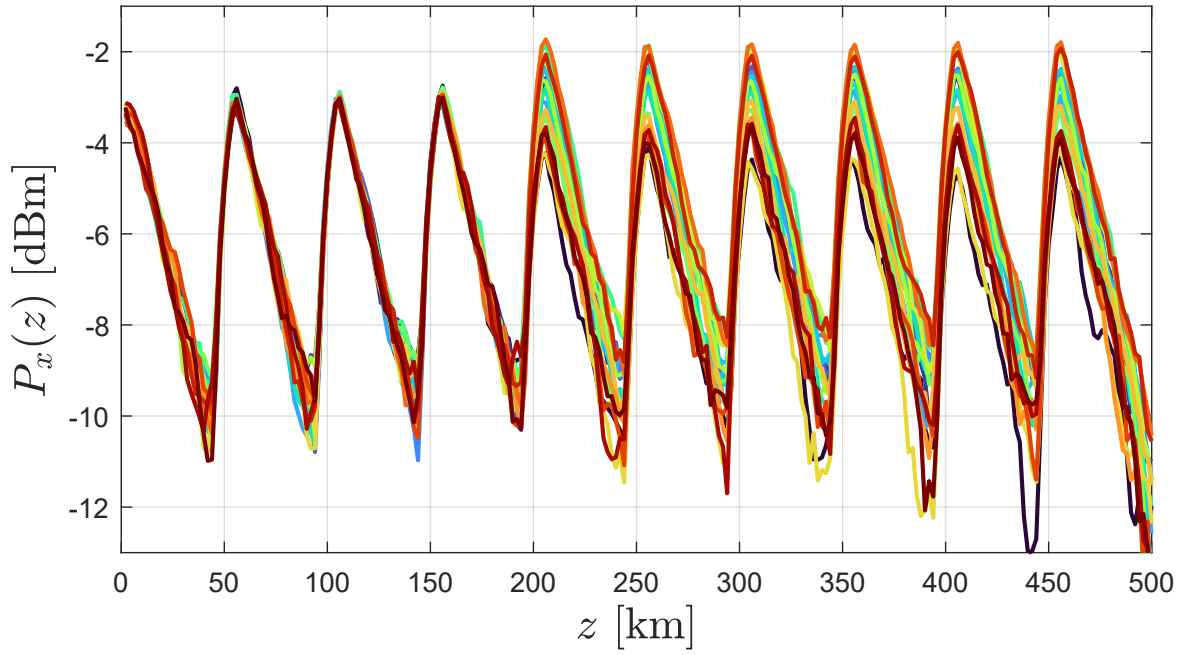

Fig. 2.5 Estimated power profiles, corresponding to all simulated SOPs, for the x-polarization at a per-channel power of 2 dBm, with a nominal PDL element of 3 dB located at $z = 200$ km from the transmitter.

This increase identifies the beginning of the 5-th span as the location of the lumped PDL element.

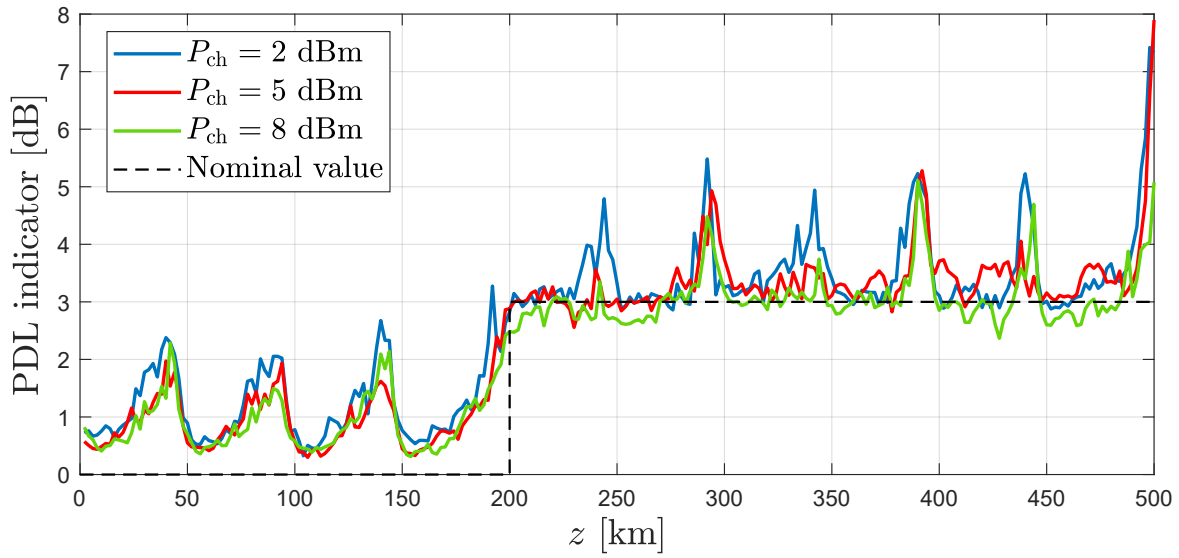

Fig. 2.6 PDL indicator at different transmit powers with a 3-dB lumped PDL element inserted at the beginning of the 5-th span. The dashed line indicates the nominal value.

To estimate the PDL value and compare the results, the mean and standard deviation of the PDL indicator are computed considering all the values between 200 km and 500 km, as reported in Table 2.1. Interestingly, the algorithm achieves comparable performance at the optimal launch power (2 dBm) and at a higher power level (8 dBm). Nevertheless, due to the accuracy limitations discussed earlier, the results at the optimal power exhibit increased noise, leading to the appearance of peaks every 50 km near the end of each span. In a practical experimental setting, the performance would likely degrade further due to additional impairments (e.g., transceiver imperfections) that are not captured in the simulation. It should be noted, however, that PDL is usually introduced by components located at the beginning of each span, where the signal power is highest and LPM operates most efficiently. Consequently, near the start of each span, the PDL indicator provides an accurate estimate of the PDL value across all power levels, including the optimal one. The initial values at the beginning of the span can therefore be used to obtain a more accurate estimate of the PDL, as demonstrated in Sec. 2.1.4.

Table 2.1 PDL estimation and standard deviation for different per-channel power levels.

$\mathbf{P_{ch}}$	2 dBm	5 dBm	8 dBm
Mean PDL	3.50 dB	3.40 dB	3.07 dB
σ_{PDL}	0.77 dB	0.63 dB	0.47 dB

Fig. 2.7 shows the PDL indicator, computed with the same procedure as in Fig.2.6, for different PDL values inserted at the beginning of the 5-th span. The estimation accuracy decreases at lower PDL levels, yet the algorithm correctly identifies both the position and the magnitude of the PDL element even for PDL values as low as 1 dB. More accurate power profile estimates can be achieved by increasing the number of samples used in the LPM algorithm [71] or by averaging multiple power profiles [118].

It is interesting to notice that when multiple PDL elements are present, the total PDL experienced by the CUT is not simply the sum of the individual contributions but rather a more complex function that depends on the relative alignment of the PDL axes [114]. To evaluate the method in a distributed-PDL scenario, two lumped PDL elements, each with a fixed value of 2 dB, were introduced into the setup of Fig. 2.3, placed at the beginning of the 4-th and 7-th span. By varying the relative orientation of their PDL axes, different end-to-end PDL values of 2, 3, or 4 dB were obtained. The algorithm was then executed for each case, yielding the estimations reported in Fig. 2.8. In all scenarios, the algorithm accurately estimated the end-to-end PDL, with lower accuracy for very high values due to the lower power affecting the LPM algorithm. The resulting PDL indicator can therefore be exploited in threshold-based schemes for the automatic detection of lumped PDL elements.

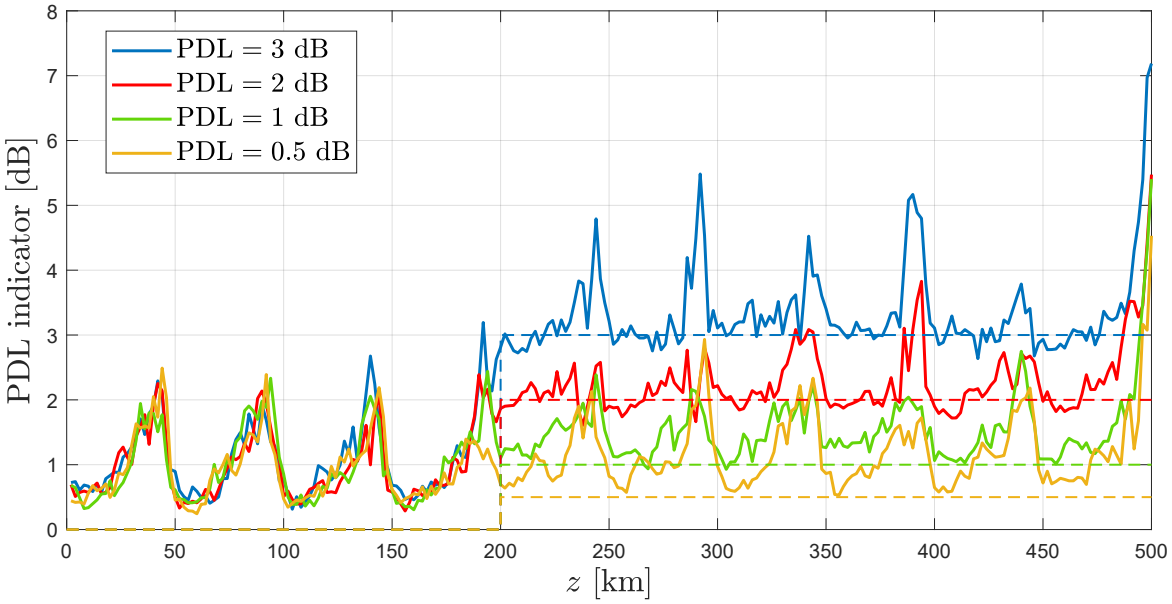

Fig. 2.7 PDL indicator for $P_{\text{ch}} = 2\,\text{dBm}$ with different PDL values, introduced by a lumped PDL element at the beginning of the 5-th span. Dashed lines indicate nominal values.

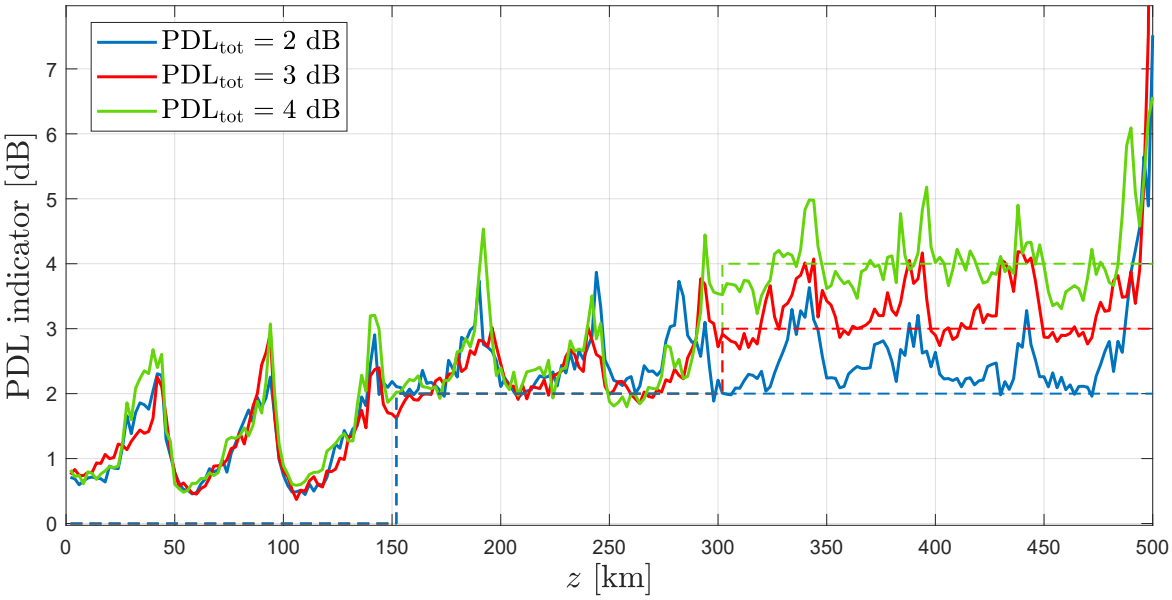

Fig. 2.8 PDL indicator with two lumped elements in the link: a fixed 2-dB PDL element at the beginning of the 4-th span and another at the beginning of the 7-th span, resulting in total link PDL values of 2, 3, or 4 dB. Dashed lines indicate nominal values.

In summary, in this section a novel PDL estimation algorithm for coherent optical links was proposed, leveraging the LLS-based LPM technique. The algorithm has been evaluated at power levels close to the optimal operating range, for different PDL values, and in scenarios

involving two PDL elements. Across all test cases, it has achieved good accuracy in estimating both the position and the magnitude of the inserted PDL. In the following, the performance of this method is compared with an alternative approach for PDL estimation and localization, based on CM-based LPM [109].

2.1.4 Comparison between LLS-based and CM-based PDL Monitoring Methods

An alternative approach to PDL estimation and localization relies on CM-based LPM. The procedure is based on an algorithm proposed for polarization-independent losses [70], later extended to include the case of PDL in [109]. It should be noted that a calibration procedure must be applied both to the transmission link and to the estimated power profiles, since CM-based LPM does not provide absolute power values. The calibration step must be carried out prior to operation and involves first computing reference power profiles, then varying the output power of the amplifiers along the link to emulate losses. For each emulated loss, a monitoring profile is estimated and used to calculate an anomaly indicator $\mathrm{AI} = \mathrm{AI}_x + \mathrm{AI}_y$, where $\mathrm{AI}_{x/y}$ denotes the anomaly indicator of the individual polarizations. A key property of these indicators is that their peak is proportional to the applied loss. This allows the estimation of a calibration factor $\hat{C}_p$ that relates correlation variations to actual power variations. Then, during operation, monitoring profiles are periodically computed and used to estimate PDL values through the calibration factor and the anomaly indicators.

While a detailed analysis of this algorithm is beyond the scope of this thesis and can be found in [109], it was implemented to allow a performance comparison with the method proposed in Sec. 2.1.2. Specifically, the setup is the same as in Fig. 2.3, with minor modifications: single-channel transmission at 5 dBm and PDL modeled using the formulation in (2.4). Moreover, the CM-based LPM is implemented as in [59] with the algorithmic modifications proposed in [60] and [109]. The nonlinear remediation parameter was set to $\varepsilon = 0.01$. The first comparison considers a lumped PDL element inserted at the beginning of the 4-th span (i.e., $z = 150$ km from the transmitter), with its value varied between 0.25 dB and 3 dB. For each PDL value, 10 estimations were carried out using both LPM algorithms, with $\sim 7 \cdot 10^5$ samples as input. In the CM-based method, calibration and reference profile estimation were performed before estimating the 10 monitoring profiles; the anomaly indicator AI was then computed, and its peak used to retrieve the inserted PDL value. In the LLS-based LPM approach, polarization rotation is required, either at the transmitter or at the receiver, to align the signal's polarization with the axes of the PDL element. To

ensure this alignment, 20 random rotations were applied at the transmitter for each estimated value, while keeping the polarization-rotating elements within the link fixed. Finally, the

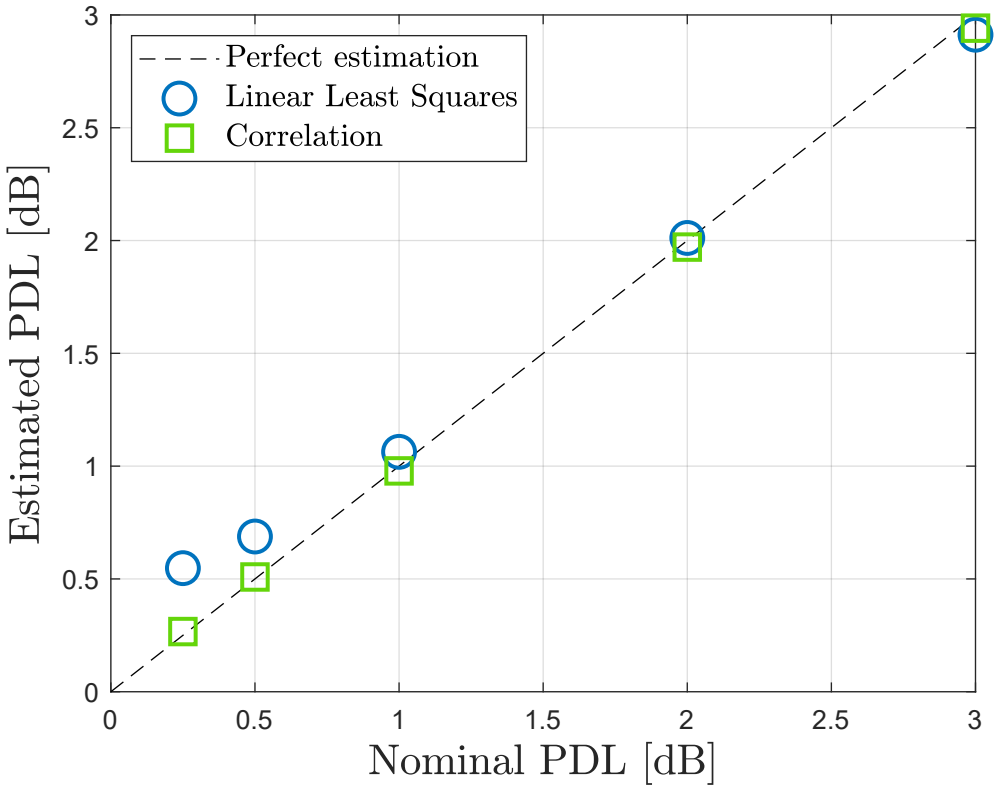

Fig. 2.9 Comparison of PDL estimation using the proposed method and the CM-based calibration method. The dashed black line indicates the nominal values.

PDL indicator enables the localization of the span where the PDL source is inserted, with its value estimated as the average of the indicator over the first half of such span. In this region, the signal power remains relatively high, allowing the LPM algorithm to provide a more accurate power estimate. The mean estimated PDL values are reported in Fig. 2.9, while the corresponding standard deviation is reported in Fig. 2.10. Both approaches achieve relatively accurate results. However, for PDL values below 1 dB, which also represent typical operating conditions, the calibration method provides highly accurate estimations, down to 0.25 dB, with a standard deviation of $\sigma_{\mathrm{PDL}} < 0.05$ dB and a maximum estimation error of 0.058 dB. In contrast, the LLS-based approach yields less accurate results. This limitation can be explained by the fact that LLS-based power profiles are obtained as deconvolved versions of the CM-based profiles, which amplifies noise and distortion. As a result, the intrinsic noise of the algorithm prevents the detection of PDL values below a certain threshold. This is confirmed by the estimation performed on the 4-th span without a PDL source, which

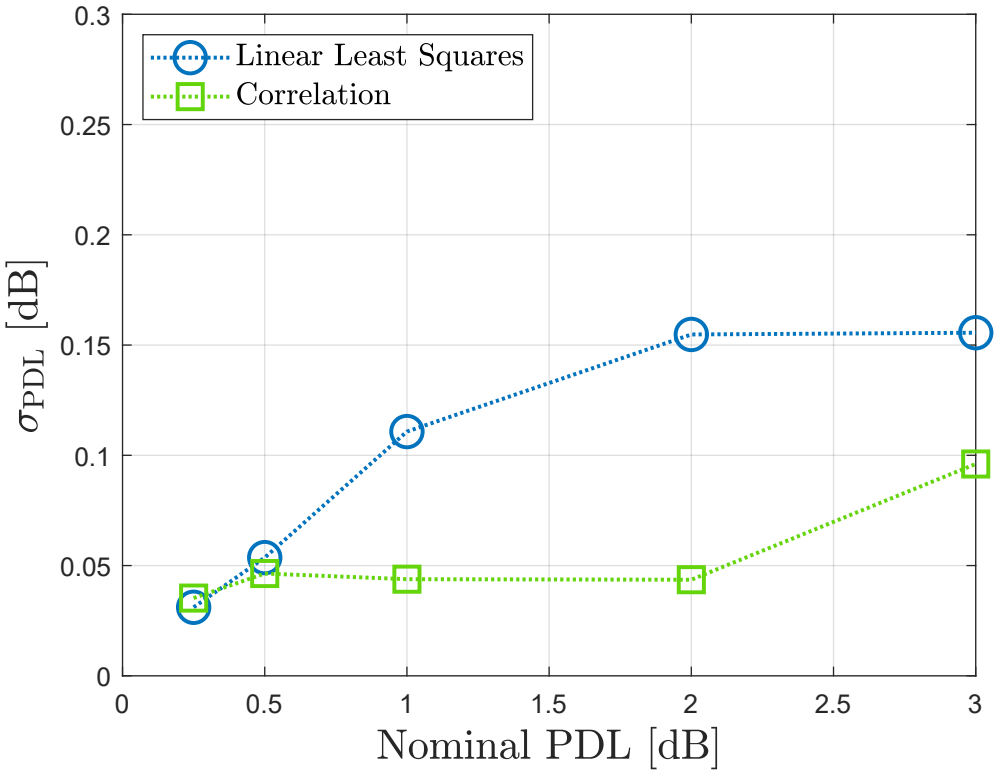

Fig. 2.10 Standard deviation of PDL estimation using the proposed method and the CM-based calibration method.

returns a value of approximately 0.5 dB, thereby defining the minimum detectable PDL under the considered conditions. Nevertheless, the reduced accuracy compared to the calibration method is counterbalanced by the lower complexity of the LLS-based approach. Unlike CM-based LPM, LLS does not require calibration on the transmission link or the computation of reference profiles for comparison. Moreover, in the CM-based method, calibration must be repeated whenever transmission parameters change, such as the symbol rate, which increases system complexity and reduces flexibility. An additional advantage of LLS-based LPM is that it directly provides the true signal power evolution, allowing PDL to be computed from its definition, i.e., as the difference between absolute power values in logarithmic units.

Another scenario considered involves multiple PDL sources within the link. In this case, two 2-dB PDL elements were inserted into the setup of Fig.2.3, at the beginning of the 4-th and 7-th spans (i.e., $z = 150\,\mathrm{km}$ and $z = 300\,\mathrm{km}$). Since the end-to-end PDL value depends on the relative orientation of the PDL axes of the individual elements, their orientations were chosen to yield a total PDL of 3 dB. The PDL and anomaly indicators obtained with the two approaches are shown in Fig.2.11. As illustrated in Fig.2.11 (top), the LLS-based approach

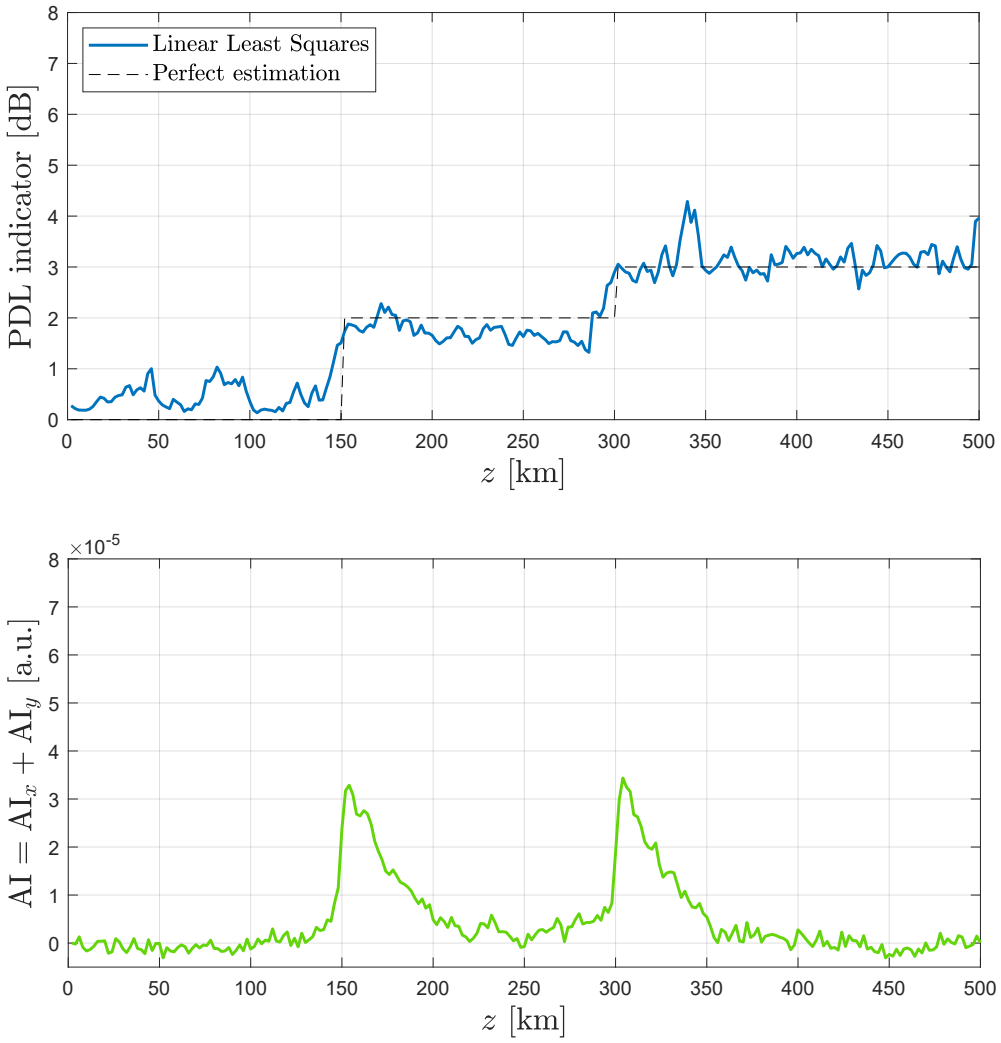

Fig. 2.11 Resulting PDL indicator (top) and anomaly indicator AI (bottom) when two 2-dB PDL elements are inserted on the link at $z = 150\,\text{km}$ and $z = 300\,\text{km}$. The end-to-end PDL is set to 3 dB.

successfully localizes both PDL elements and provides the correct cumulative value. By contrast, the CM-based approach in Fig.2.11 (bottom) can localize the PDL elements but fails to reflect the correct accumulated PDL, as both estimates remain close to 2 dB. This highlights a clear advantage of the LLS-based method over the CM-based one.

In summary, this work presented a comparison between LLS-based and CM-based LPM methods for the localization and estimation of PDL in a single-channel multi-span optical transmission link. The CM-based method demonstrated the ability to detect and estimate PDL values as low as 0.25 dB, with a maximum estimation error of 0.058 dB, but at the cost of a more complex calibration procedure. In contrast, in scenarios with multiple PDL sources

along the link, only the LLS-based method was able to both detect and correctly estimate the end-to-end PDL value.

2.2 Multi-Channel Longitudinal Monitoring

In this section, the application of LPM is extended to a different transmission scenario, namely systems employing digital subcarrier multiplexing (DSCM). The objective here is to investigate how LPM can be leveraged in the context of DSCM, assessing its capability to estimate the longitudinal power evolution in multi-subcarrier systems. This analysis highlights both the potential of LPM in enhancing monitoring functions beyond traditional single-carrier links and the specific considerations required when dealing with digitally multiplexed subcarriers.

2.2.1 Digital Subcarrier Multiplexing Systems

Subcarrier multiplexing is a technique in which multiple signals are multiplexed in the RF domain and transmitted over a single optical wavelength, generally at lower symbol rates. Initially, one of the key advantages of SCM was the maturity of microwave devices compared to their optical counterparts: microwave oscillators offered greater stability, and microwave filters provided higher frequency selectivity. Furthermore, the low phase noise of RF oscillators simplified coherent detection in the RF domain relative to optical coherent detection, while also enabling the straightforward use of advanced modulation formats [119]. In DSCM, the subcarriers are multiplexed and demultiplexed digitally in the DSP engine, and by employing a small roll-off factor, the spectral occupancy is made equivalent to that of a single-carrier signal. Thanks to digital multiplexing and demultiplexing, the analog bandwidth requirements and the ADC/DAC sampling rate remain the same as in a single-carrier system. Moreover, only one transmit laser and one local oscillator are required for coherent detection [120]. Figure 2.12 gives a representation of the power spectral density of a SCM signal compared to that of a single-carrier signal.

The use of DSCM was initially explored for its propagation advantages [121]. More recently, it has proven to provide benefits in several additional areas. For instance, DSCM is effective in mitigating the impact of nonlinear interference (NLI) [122] and represents a viable solution for point-to-multipoint transmission systems [123]. Furthermore, DSCM enables optimized DSP design to better adapt to rapid traffic evolution. In particular, the

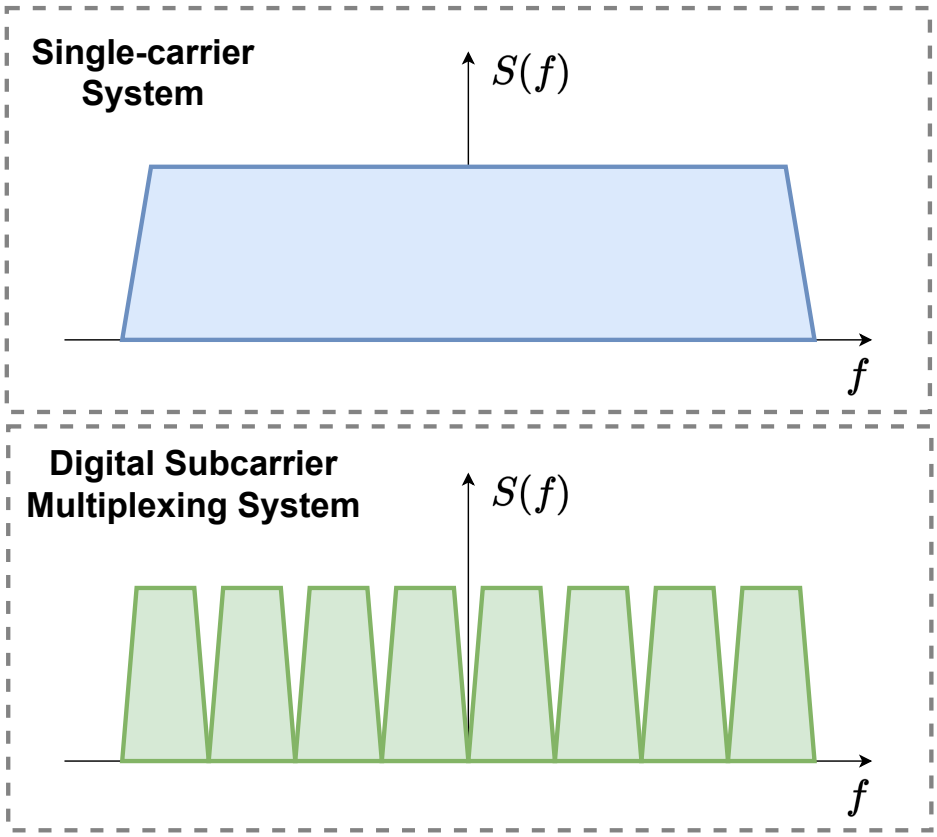

Fig. 2.12 Visualization of the power spectral density $S(f)$ of a single-carrier system (top) and a DSCM system with 8 subcarriers (bottom).

lower symbol rate associated with DSCM reduces the complexity of CD compensating filters and mitigates the impact of equalizer-enhanced phase noise [124]. These considerations highlight the relevance of applying LPM to such systems

2.2.2 Application of Longitudinal Power Monitoring to Subcarrier Multiplexing Systems

The system was simulated under four different configurations of the DSCM transmitted signal and is illustrated in Fig. 2.13. In each case, the signal consists of N_{sc} probabilistically-shaped (PS)-64QAM subcarriers, shaped according to a Maxwell–Boltzmann distribution with an entropy of 4.41 bits [125]. All subcarriers are filtered with a root-raised-cosine filter with roll-off $\rho = 0.05$ and modulated at the same symbol rate R_{s}. The frequency spacing was set to $\Delta f = 1.1 B_{\mathrm{sc}}$, where B_{sc} denotes the bandwidth of each subcarrier. Each configuration is defined by a number of subcarriers equal to a power of two, i.e., $N_{\mathrm{sc}} = 2^k$, with $k = 0, 1, 2, 3$

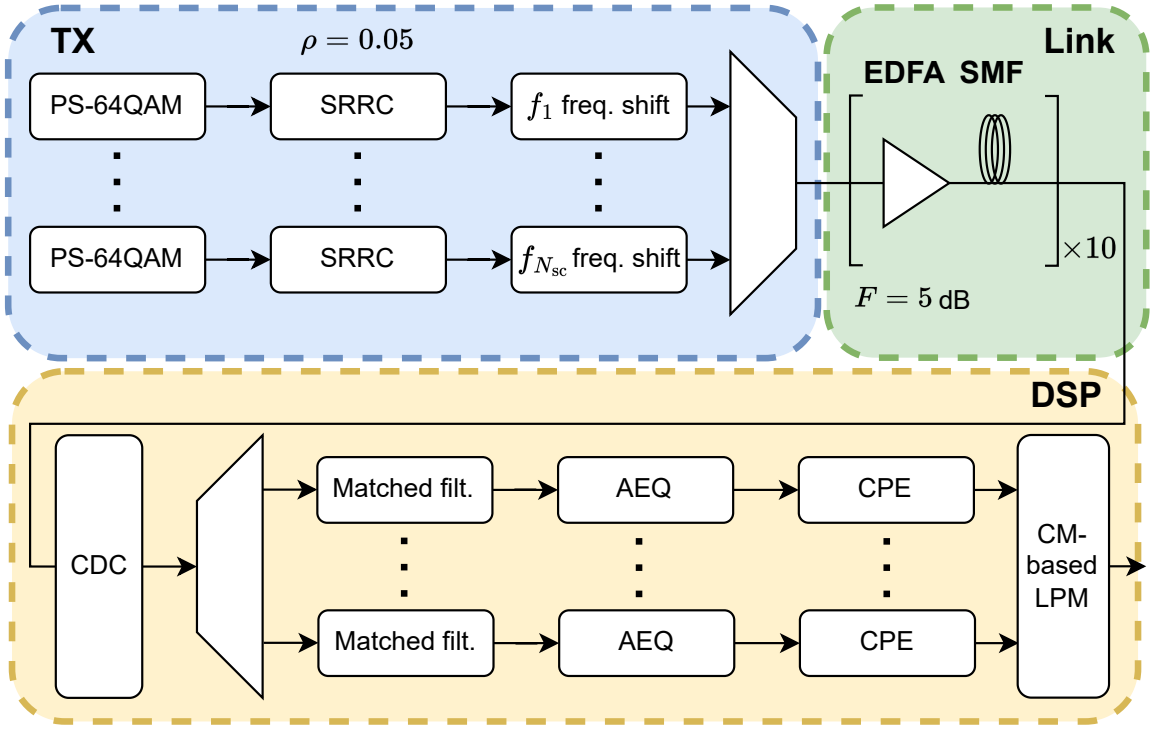

Fig. 2.13 Schematic of DSCM simulation setup.

identifying the configuration index. The corresponding symbol rate is given by $R_s = 64/2^k$ GBaud. In all cases, the subcarrier powers were set such that the total transmitted power equals $P_{TX} = 8\,\text{dBm}$, ensuring that the four signals are equivalent in terms of launch power, total symbol rate, and spectral occupancy.

The transmitted signal is then propagated over a link composed of 10×50-km spans of SMF ($\alpha_{dB} = 0.2\,\text{dB/km}$, $\beta_2 = -21.28\,\text{ps}^2/\text{km}$, and $\gamma = 1.3\,1/\text{W/km}$). At the end of each span, an EDFA with a noise figure of $F = 5\,\text{dB}$ fully compensates for the span loss. Fiber propagation is simulated using the SSFM, implementing the Manakov equation. The propagated signal is then received by a standard coherent receiver, where CD is compensated and each subcarrier is extracted and resampled at 2 samples per symbol. The subcarriers are subsequently processed independently through DSP blocks implementing matched filtering, LMS-based adaptive equalization, and BPS carrier phase recovery. The outputs of the final DSP stage are extracted and used to reconstruct the complete received signal, which serves as the input to the CM-based LPM algorithm. The implementation follows the algorithmic modifications introduced in [60], with a spatial step of $\Delta z = 2\,\text{km}$ and a nonlinear remediation parameter set to $\varepsilon = 0.0001 \cdot 2^k$, depending on the configuration. Moreover, all correlations between received and reference signals are calculated using the Pearson

correlation coefficient. Note that the reference signals that are used in the correlation operations have been reconstructed from the originally transmitted sequences, since no FEC decoding was implemented.

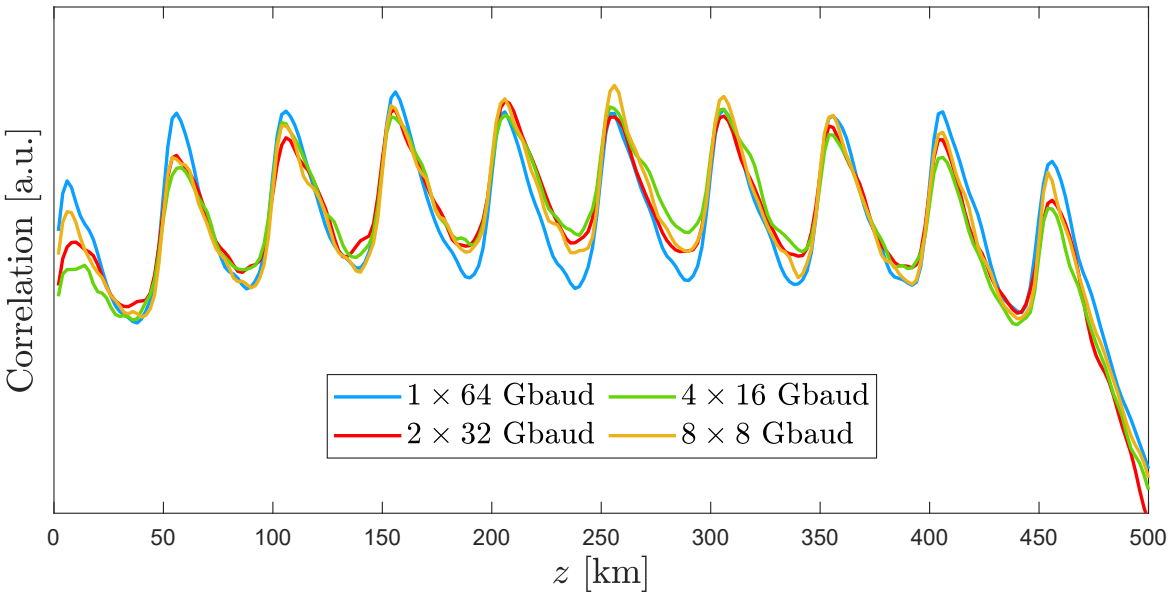

Fig. 2.14 Average CM-based power profiles for the four DSCM simulated configurations.

Figure 2.14 reports the results obtained for the four simulated configurations. Each configuration was simulated 10 times, and the corresponding estimated power profiles were averaged to reduce the impact of noise and mitigate distortions affecting the signals processed by the LPM algorithm. These distortions arise because the SCM signal undergoes several resampling and filtering operations in the DSP, required for per-subcarrier processing and subsequent reconstruction of the original received signal. For visualization and comparison purposes, the mean value of the averaged profiles was subtracted. This choice also explains the expression adopted for the nonlinear remediation parameter ε, which in the CM-based LPM algorithm governs the mitigation of nonlinear effects. While ε is usually set to a small fixed value [59], the degree of nonlinearity compensation influences the correlation and, therefore, the scaling of the estimated profiles. To facilitate visualization, ε was increased for lower symbol rates, following a heuristic rule. However, optimizing this parameter is not necessary for practical purposes and falls outside the scope of this work. Finally, probabilistic shaping was applied to the transmitted symbol sequences, primarily to enhance estimation accuracy in the initial spans of the transmission link, where accumulated CD is lower, and to avoid the need for CD pre-distortion [71]. With these considerations in mind, the LPM algorithm produced reasonably good results across all the configurations analyzed, meaning

that it successfully captures both the correct power evolution of the propagating signal and the main characteristics of the optical link in this configuration. It can be observed, however, that the estimation noise increases with the number of subcarriers. This effect is most likely caused by the distortions discussed above, which accumulate as more subcarriers are involved in reconstructing the received SCM signal. Nevertheless, this issue does not represent a significant limitation, as the averaging operation effectively mitigates it.

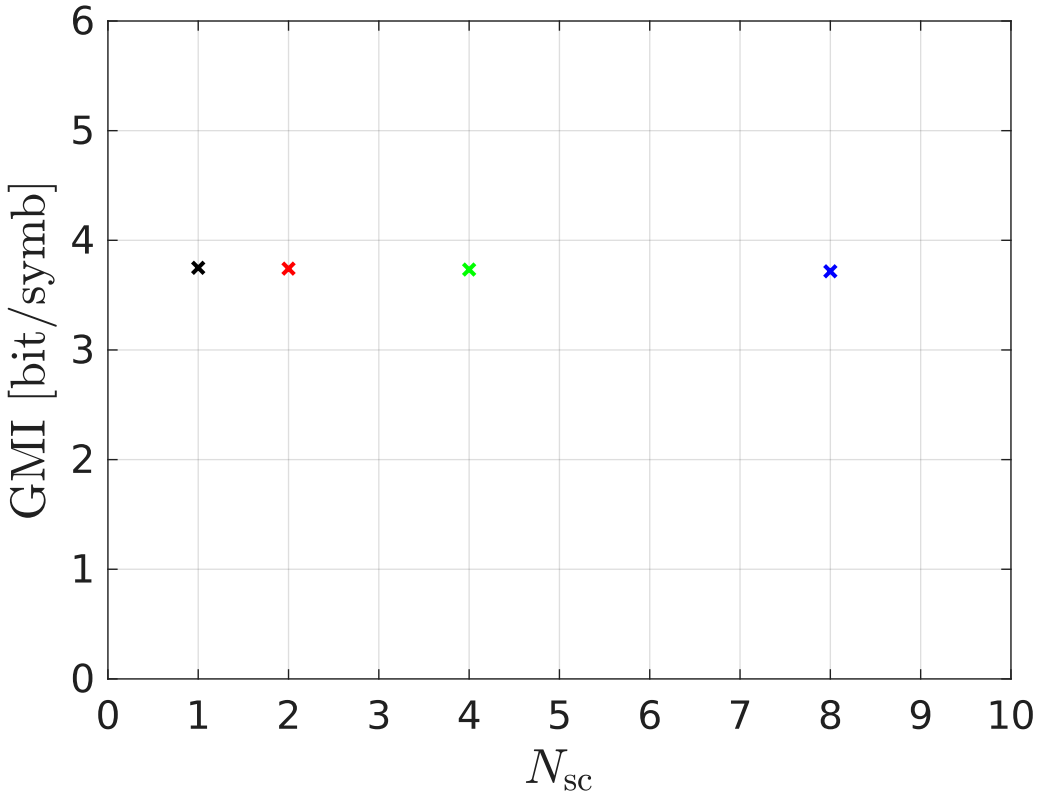

Fig. 2.15 Average generalized mutual information for different number of subcarriers.

Finally, the average generalized mutual information (GMI) is reported in order to prove that the performances of the four configurations are also equivalent. Figure 2.15 shows the average GMI as a function of the number of subcarriers N_{sc}, computed as the mean of the GMI values obtained from all processed subcarriers in a given configuration. The results are consistently around 3.74 bit/symb. These relatively low values arise because high launch powers are preferable for LPM applications ($P_{\mathrm{TX}} = 8\,\mathrm{dBm}$ in this work), whereas they are generally far from the optimal launch powers for communication purposes [71].

In conclusion, the applicability of LPM using a CM-based algorithm has been demonstrated in the context of SCM systems. Despite the noisier profiles, the performance remains

comparable to that achieved in a single-carrier scenario. It is worth noting that, after this work was published, another study [126] investigated multi-channel LPM in the context of WDM systems, where a multi-bandpass filtering approach was proposed to mitigate the impact of out-of-band NLI noise, an impairment typically absent in single-channel scenarios, and improve the esitmation of power profiles.

2.3 Monitoring of Raman-amplified Ultra-Wideband Transmission Systems

In recent years, several extensive experimental demonstrations of LPM have been reported. One particularly challenging scenario is the UWB [127] (i.e., beyond the C-band), where the choice of the amplification scheme plays a crucial role [128]. Conventional doped fiber amplifiers, such as EDFAs, cannot provide gain over the entire WDM comb, which necessitates the use of multiple parallel amplifiers, thereby increasing both system cost and complexity. To overcome this limitation, two main approaches have been considered for single-amplifier UWB systems: Raman amplification and semiconductor optical amplifiers (SOAs) [128]. While recently developed SOAs can provide substantial gain over bandwidths exceeding 100 nm, they still suffer from drawbacks such as high noise figure and polarization-dependent gain. On the contrary, Raman amplification can deliver wideband amplification with a low noise figure [129], but the design and optimization of Raman-amplified UWB links remain particularly challenging due to the interplay with inter-channel stimulated Raman scattering (ISRS) [130]. For this reason, accurate live monitoring of the per-channel power profile is critical to enable the operation and optimization of Raman-amplified UWB transmission systems.

Both simulative and experimental demonstrations of LPM in UWB scenarios have already been reported, including the monitoring of EDFA spectral gain, identification of anomalies such as gain tilt or narrowband compression [60, 74], and the assessment of ISRS [131]. However, the approaches in [60, 74] relied on a CM-based LPM technique [59], which requires CD pre-distortion and a calibration procedure [70] to recover the true optical power and perform the aforementioned operations. Moreover, these demonstrations were limited to transmission distances of up to 280 km and did not employ a fully Raman-based amplification scheme. To date, LPM has only been demonstrated in hybrid Raman-EDFA transmission scenarios, either in simulation over very short distances and with a limited number of WDM channels [132], or experimentally in a single C-band transmission [63]. For this reason, in

this work we demonstrate the application of LLS-based LPM over a fully backward Raman-amplified C+L band system, consisting of 9×60-km spans of G.652 SMF. We show that, across all power levels, the estimated power profiles closely match the power levels measured by OSAs. First, a brief introduction to the main scattering effects in optical fibers and their applications is provided. This is followed by the presentation of the experimental setup and results.

2.3.1 Raman Scattering: Principle and Applications

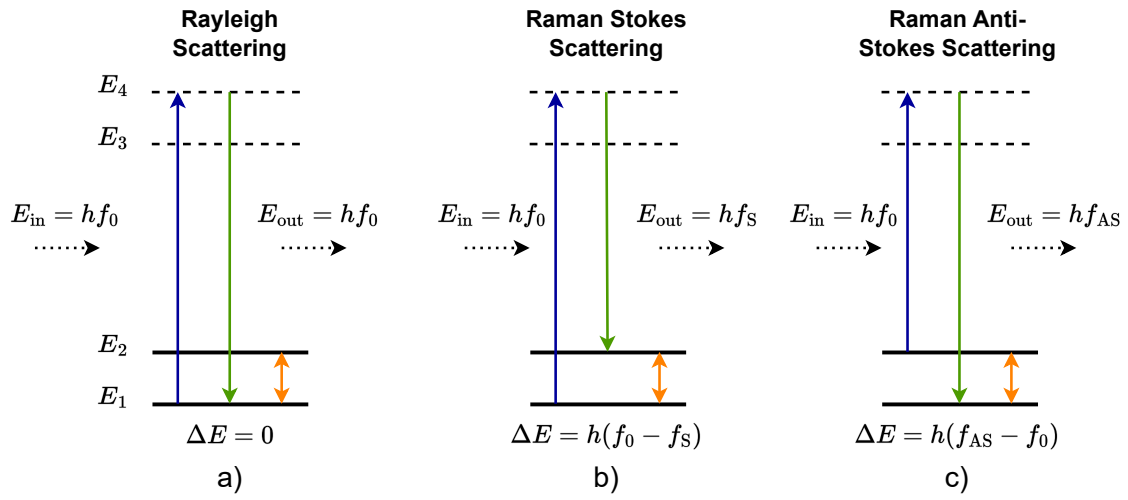

Fig. 2.16 Schematic diagram of a) Rayleigh scattering, b) Raman Stokes scattering and c) Raman anti-Stokes scattering.

In optical fibers, scattering phenomena play a fundamental role in determining both signal attenuation and opportunities for optical amplification. The two most relevant types of scattering are Rayleigh scattering and Raman scattering [133]. Rayleigh scattering is an elastic process, i.e., photons are scattered by microscopic fluctuations in the refractive index of the fiber without any change in their energy, only in direction. Raman scattering, on the other hand, is an inelastic process, in which incident photons interact with the vibrational modes of the medium material molecules, leading to a frequency shift of the scattered light. We can distinguish between two types of Raman scattering, namely Stokes scattering, where photons lose part of their energy to molecular vibrations and are re-emitted at a longer wavelength (lower frequency), and anti-Stokes scattering, which is a generally rarer effect [134] and where photons gain energy from vibrational modes and are scattered at shorter wavelengths (higher frequency). A visual representation of the main scattering effects in

optical fibers is reported in Fig. 2.16, where E denotes the energy, ΔE the energy variation, f the frequency and h the Planck's constant. Spontaneous Raman scattering is relatively weak, but under high optical power it evolves into stimulated Raman scattering (SRS), where a strong pump wave efficiently transfers energy to a weaker signal at the Stokes frequency. An exmaple of a normalized Raman gain profile versus the frequency offset from the pump is reported in Fig. 2.17.

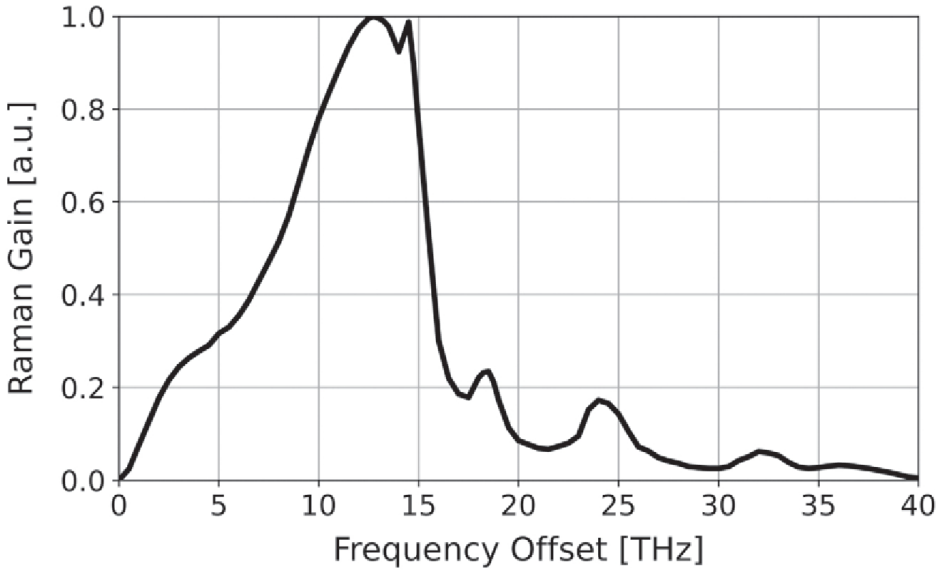

Fig. 2.17 Normalized Raman gain versus frequency offset from pump. Source: [135].

This stimulated effect is exploited in Raman amplification. By injecting one or more pump lasers into the transmission fiber, the signal wavelengths receive gain along the fiber span through energy transfer from the pump to the Stokes-shifted signals. Compared to discrete EDFAs, Raman amplification provides several advantages: the gain is distributed along the transmission line, which reduces noise accumulation and extends system reach, the spectral region of amplification can be flexibly tuned by selecting the pump wavelengths, and the achievable bandwidth can extend well beyond the conventional C-band, covering the L-band and even additional transmission windows [128]. On the other hand, their drawbacks include the difficulty of achieving stable and flat gain, eye-safety concerns, and vulnerability to multi-path interference [136]. Raman amplification can be implemented in two main configurations: forward- and backward-pumping. In forward Raman amplification, the pump light is injected in the same direction as the signal propagation. This provides amplification along the link, but also increases the amount of pump relative intensity noise that is transferred to the signal, which can degrade system performance. Moreover, forward pumping tends to increase nonlinear interactions between pump and signal. In backward

Raman amplification, the pump is injected in the opposite direction to the signal. This configuration has the advantage that the signal encounters the strongest pump power toward the end of the fiber span, where the signal is most attenuated. As a result, backward pumping offers a better SNR and significantly reduces the transfer of pump noise to the data channels [137]. Note that hybrid pumping schemes combining both forward and backward Raman amplification can also be used, mainly in unrepeteared systems. This allows balancing the benefits of higher gain efficiency from forward pumping with the noise suppression advantages of backward pumping, achieving improved overall performance [138]. Moreover, hybrid backward-Raman/EDFA amplification schemes are normally used to improve OSNR [139] .

Although good closed-form models are available to predict the behavior of UWB Raman-amplified links [140, 141], they rely on full knowledge of the link parameters and, most of all, require the computation of the power profile evolution of the propagating signals. This process generally consumes up to 95% of the computation effort to evaluate system performance [142]. The power profile computation requires to solve a set of coupled differential equations that can be formulated as [129]:

$$d_i \frac{d}{dz} P_i = -\alpha_i P_i + \sum_j (P_i + N_{ij}) g_{ij} P_j \tag{2.10}$$

$$g_{ij} = \begin{cases} g_R(f_j, f_j - f_i)/(2 \cdot A_{\text{eff}}) & f_j > f_i \\ 0 & f_j = f_i \\ -(f_i/f_j) \cdot g_R(f_i, f_i - f_j)/(2 \cdot A_{\text{eff}}) & f_j < f_i \end{cases} \tag{2.11}$$

$$N_{ij} = 2hf_i \Delta f_i (1 + n_{ij}) \tag{2.12}$$

$$n_{ij} = \left[\exp\left(\frac{h|f_j - f_i|}{k_B T} \right) - 1 \right]^{-1} \tag{2.13}$$

where the subscripts i and j run over all signals and pumps, d_i denotes the direction (i.e., ± 1 for forward/backward propagation), k_B is Boltzmann's constant, T the temperature, P the power, g_R the Raman gain coefficient, A_{eff} the effective area of the modes in the fiber and N the ASE noise. With these considerations, they are more suitable for the design phase than for monitoring. For this purpose, LLS-based LPM represents a suitable solution, as demonstrated in the following.

2.3.2 Experimental Setup

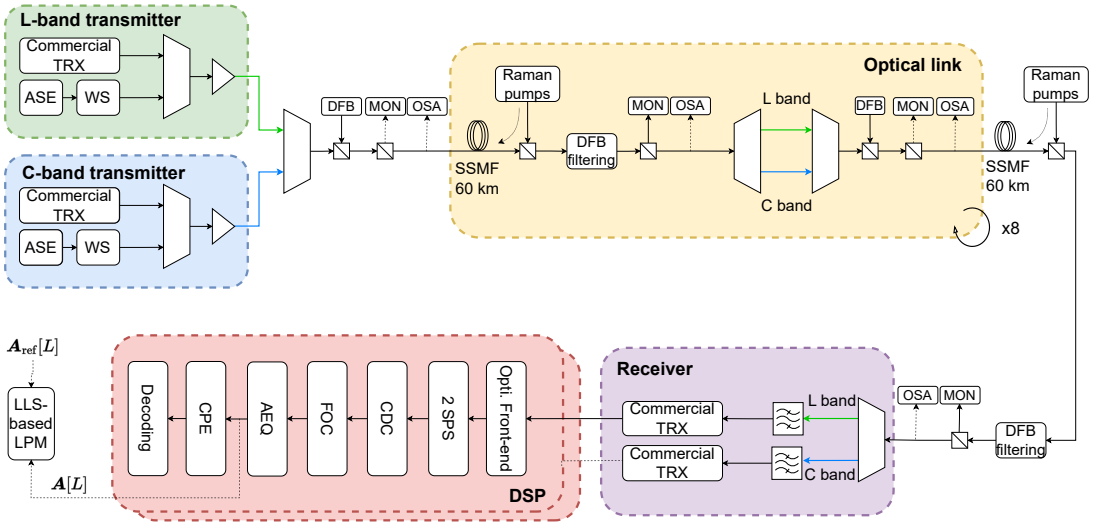

Fig. 2.18 Experimental setup. WS: WaveShaper; DFB: distributed-feedback laser; MON: monitor.

The experimental setup is illustrated in Fig. 2.18. At the transmitter, two commercial transceivers (one operating in the C-band and the other in the L-band) generated 64-Gbaud DP-QPSK signals for the channel under test (CUT). During the experiment, the transceiver wavelength was varied in order to probe different WDM channels. The remaining WDM channels were emulated using shaped ASE noise, resulting in a total of 36 channels (18 per band), spaced by 200 GHz. A relatively large spacing was chosen to enable accurate channel-resolved in-line OSNR measurements with the OSA and to support potentially high per-channel launch powers. Two booster EDFAs set the total launch power, adjusted to 0, 4, and 8 dBm per channel with a flat power profile. The WDM signal was transmitted over nine spans, each consisting of 60 km of G.652 SMF, and amplified with five counter-propagating Raman pumps, whose wavelength and power are listed in Tab. 2.2.

Table 2.2 Raman pumps configuration

Wavelength [nm]	Power [mW]
1423.81	306
1435.29	280
1450.25	178
1465.91	121
1494.82	173

At the beginning of each span, the C-band and L-band signals were combined, and at the output they were separated. A monitoring system, together with an OSA, measured

the per-channel power and channel-resolved OSNR at both span input and output. No gain equalization was applied, leading to significant power variations among channels, which allowed testing the LPM algorithm under different operating conditions. In addition, light from a distributed feedback (DFB) laser was multiplexed with the transmitted signal to serve as a monitoring channel for the Raman modules, enabling pump ON/OFF control.

At the end of the 9-th span, the WDM comb was demultiplexed and received by a commercial transceiver. Instead of relying on the real-time DSP, raw ADC samples were extracted and processed offline. The offline DSP chain included resampling at two samples per symbol, blind FOC, CD estimation and compensation [143], LMS-based 2×2 MIMO fractionally spaced equalization, and Viterbi–Viterbi (4-th power) phase estimation. Finally, the received constellation was compared with the transmitted sequence to compute the SNR.

Measurements were carried out on a total of six channels: three in the L-band (channels 3, 9, and 15, centered at 187.06, 188.26, and 189.46 THz, respectively) and three in the C-band (channels 3, 9, and 15, centered at 191.90, 193.10, and 194.30 THz, respectively). For each channel, 25 sequences of 2^{17} samples were captured from the ADCs, sampled at 96 Gsamp/s. LLS-based LPM was then applied with a spatial resolution of $\Delta z = 2\,\text{km}$, and the resulting 25 profiles were averaged to mitigate estimation noise.

The results presented in the following refer to the $P_{\text{ch}} = 0$ dBm transmission condition, although similar results were obtained for the other tested scenarios.

2.3.3 Experimental Results

Fig. 2.19 shows the spatial and spectral evolution of the optical power for each measured WDM channel. It should be noted that the LLS-based algorithm estimates $\gamma' = \frac{8}{9}\gamma\mathbf{P}$, which implies that knowledge of the nonlinear fiber parameter γ is required to recover the absolute optical power. In the UWB scenario, γ exhibits a weak wavelength dependence that must be considered for accurate results. For this reason, γ was estimated using the method described in [144, 145], taking into account only the SCI contribution, since this is the sole term exploited by LPM for power profile estimation.

The power profiles in Fig. 2.19 clearly reveal the effect of Raman scattering induced by both the Raman pumps and the other WDM channels. This explains the observed evolution of the profiles, which show a general increase in power toward the L-band and a ripple-like structure across the spectrum. Figure 2.20 illustrates the power distribution over the frequency–distance plane, providing a clearer visualization of this behavior.

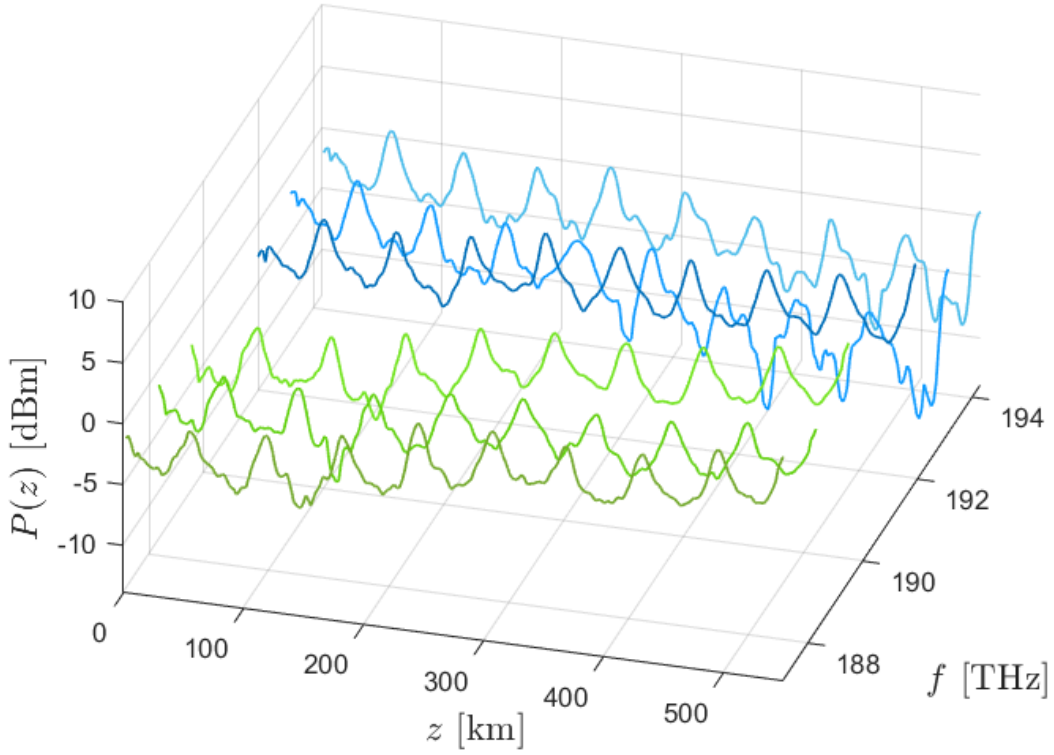

Fig. 2.19 Estimated power profiles after 25-profile averaging for the measured channels in L (green) and C (blue) bands with $P_{\text{ch}} = 0$ dBm.

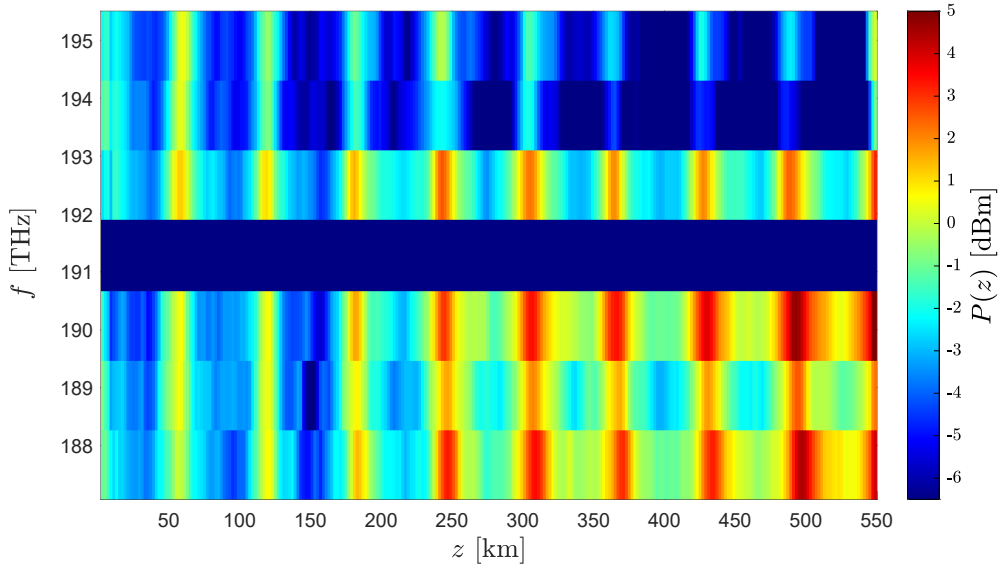

Fig. 2.20 Spectral and spatial optical power evolution over the link.

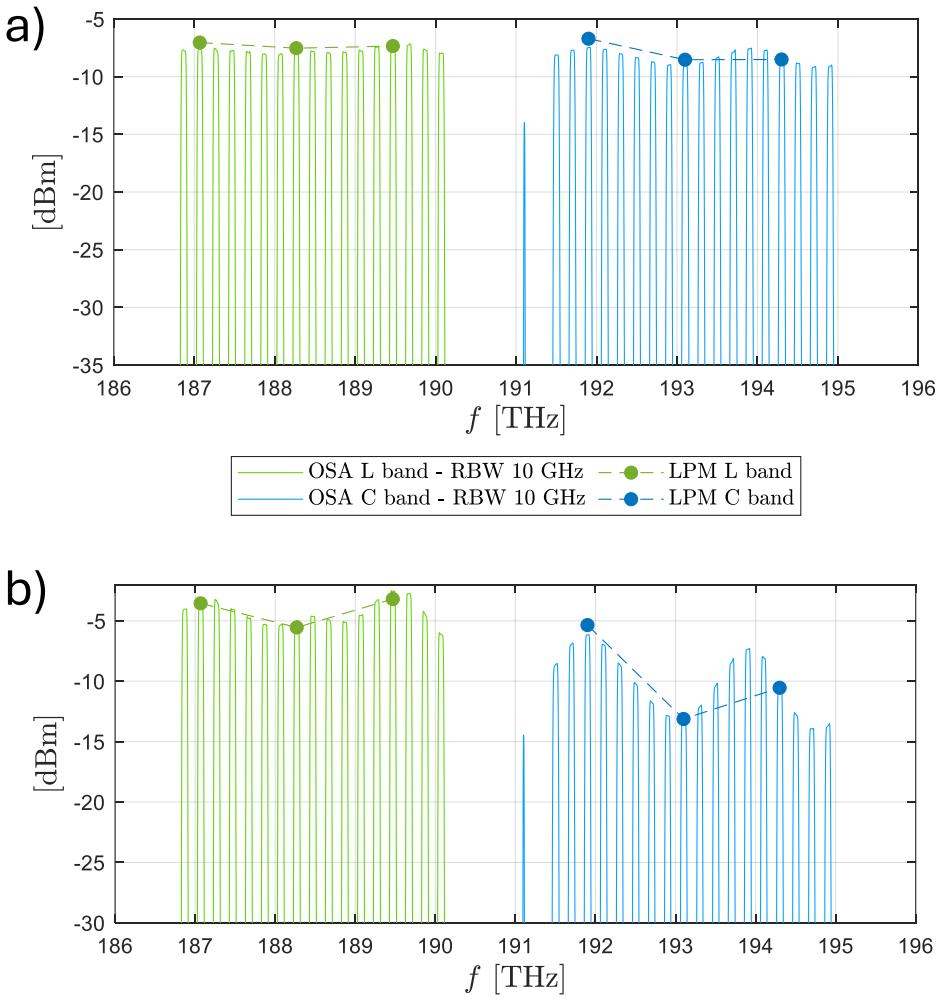

Fig. 2.21 OSA power spectrum vs. LPM power estimates at the input of the a) 3-rd and b) 9-th span.

To validate the results, the power values estimated by LPM were compared with the spectra measured by the OSA at the input of each span. Since the OSA integrates power over a reference bandwidth (RBW) of 10 GHz, the LPM estimates were normalized accordingly. Figure 2.21 reports the comparisons at the input of the 3-rd and 9-th span, respectively. The estimated values closely match the OSA measurements and correctly reproduce the power evolution of the monitored channels across the link. At the input of the 3-rd span, the spectrum remains relatively flat; however, after propagation, a pronounced ripple appears, creating a power imbalance among the measured channels. This imbalance is approximately 2 dB for channels 3–9 and 9–15 in the L-band, while it increases to about 8 dB and 3 dB for the corresponding channels in the C-band. In all cases, the LPM algorithm successfully tracks these variations.

The absolute estimation error between the rescaled LPM values and the OSA measurements was also evaluated. At the input of the 3-rd span, the errors remain below 0.77 dB, with a mean of 0.43 dB. At the 9-th span, the maximum error slightly increases to 0.83 dB, while the mean value remains unchanged at 0.43 dB.

To conclude, in this work LLS-based LPM was applied to a C+L band transmission system consisting of a 9×60 km SMF link with full Raman amplification. The results show that LPM can accurately track the power evolution of channels in both the C- and L-bands, with a maximum absolute error below 0.83 dB, as confirmed by comparison with OSA measurements. Such information is valuable for the design and optimization of Raman-amplified ultra-wideband transmission systems.

2.4 Conclusions

In this chapter, several novel applications of LPM were presented and analyzed, with a particular focus on PDL estimation and localization, and applications to DSCM and UWB transmission scenarios. First, a new PDL estimation algorithm for coherent optical links was proposed, leveraging the LLS-based LPM technique. The method was evaluated at power levels close to the optimal operating range, for different PDL values, and in configurations involving multiple PDL elements. Across all test cases, the algorithm demonstrated good accuracy in estimating both the position and the magnitude of the inserted PDL. A comparison with the approach in [117] showed similar performance, with slightly better accuracy at low PDL values, likely due to the use of more samples and a shorter transmission link. That work also provided an experimental demonstration, further supporting the feasibility of this class of methods. The LLS-based approach was then compared with an alternative PDL estimation method relying on CM-based LPM [109]. The CM-based method proved capable of detecting and estimating PDL values as low as 0.25 dB with very high accuracy (maximum estimation error of 0.058 dB), but at the expense of a more complex calibration procedure. In scenarios with multiple PDL sources, however, only the LLS-based method was able to correctly detect and estimate the end-to-end PDL value, underlining its advantage in practical multi-span links. The applicability of LPM was further extended to DSCM systems, where a CM-based algorithm was implemented. Despite producing noisier profiles compared to single-carrier transmission, the method was shown to achieve comparable performance, confirming the potential of LPM in more flexible transmission architectures. After the completion of this work, a related study [126] investigated multi-channel LPM for WDM systems and proposed

a multi-bandpass filtering strategy to mitigate out-of-band NLI noise, further highlighting the relevance of extending LPM to more complex transmission scenarios. Finally, the use of LPM was experimentally demonstrated in a C+L band transmission system with full backward Raman amplification over a 9×60 km SMF link. The LLS-based method was shown to track the power evolution of both C- and L-band channels with a maximum absolute error below 0.83 dB, in close agreement with measurements obtained from OSAs. This confirms the capability of LPM to provide accurate channel-resolved monitoring in Raman-amplified UWB links, thus offering valuable information for the design, optimization, and real-time operation of next-generation optical transmission systems.

Chapter 3

Nonlinear Interference Estimation for Transmit Power Optimization

In this chapter, a novel method for Kerr-induced nonlinear interference monitoring is proposed, based on the LLS-based LPM algorithm. In Sec. 3.1, an overview of the main approaches that have been proposed so far for NLI monitoring is presented. The proposed method is then introduced in Sec. 3.2, demonstrating how LLS-based LPM can inherently estimate NLI, supported by a preliminary numerical analysis. Next, strategies to mitigate estimation biases caused by XCI are discussed, with an emphasis on minimizing the amount of system knowledge required. In Sec. 3.3, the method is validated in a more realistic numerical setup that better models practical transmission conditions. In Sec. 3.4, experimental validation is provided in two scenarios: first, a 300-km link, representing conditions where LPM typically performs well; and second, a more challenging 1100-km link, where NLI monitoring is carried out over multiple WDM channels to assess the ability of the algorithm to track NLI evolution across the different WDM channels. Moreover, an example of how these results can be used for transmit power optimization is provided. Finally, in Sec. 3.5, the main implementation penalties associated with LPM and the proposed method are discussed, together with experimentally-validated mitigation strategies. The methodologies, simulations, and experimental results discussed in this chapter have also been reported in the following publications:

- L. Andrenacci, G. Bosco, Y. Jiang, A. Nespola, S. Piciaccia and D. Pilori, "DSP-Based Nonlinear Interference Estimation Using Linear Least Squares Longitudinal Power Moni-

toring," in Journal of Lightwave Technology, vol. 43, no. 8, pp. 3536-3546, 15 April15, 2025, doi: 10.1109/JLT.2025.3532100.

- L. Andrenacci, G. Bosco, Y. Jiang, A. Nespola, S. Straullu, S. Piciaccia and D, Pilori, "Nonlinear Noise Estimation using Linear Least Squares-based Longitudinal Power Monitoring," ECOC 2024; 50th European Conference on Optical Communication, Frankfurt, Germany, 2024, pp. 172-175;

- L. Andrenacci, A. Nespola, S. Straullu, Y. Jiang, S. Piciaccia, G. Bosco and D. Pilori, "Implementation Penalties for Nonlinear Interference Estimation with Linear Least Squares Longitudinal Power Monitoring," 2025 Optical Fiber Communications Conference and Exhibition (OFC), San Francisco, CA, USA, 2025, pp. 1-3.

- G. Bosco, L. Andrenacci, A. Nespola, S. Straullu, Y. Jiang, S. Piciaccia and D. Pilori, "DSP-Based Nonlinear SNR Estimation via Longitudinal Power Monitoring in Commercial Coherent Receivers," 2025 25th Anniversary International Conference on Transparent Optical Networks (ICTON), Barcelona, Spain, 2025, pp. 1-5, doi: 10.1109/ICTON67126.2025.11125018.

3.1 Overview of Nonlinear Interference Monitoring

The DSP modules embedded in commercial coherent transceivers already provide valuable telemetry information [146]. Parameters such as accumulated CD, SOP, and PDL [12, 147] are inherently estimated by the DSP to enable proper data decoding, as already discussed. Additional metrics, including PMD and the presence of interfering WDM channels [148], can be extracted through relatively simple post-processing, either online or offline, of DSP output data. Moreover, these insights can be obtained without the use of external monitoring equipment such as OSAs or OTDRs, enabling a cost-effective and continuous flow of telemetry from every transceiver across the network. Among the various telemetry data, the constellation SNR or equivalently the error vector magnitude (EVM), is one of the most important. Since the coherent optical channel can be accurately modeled as an additive white Gaussian noise (AWGN) channel [149], this metric provides a direct means to estimate the BER or the GMI. These, in turn, are closely tied to the achievable information rate (AIR) of the system after hard-decision (HD) or soft-decision (SD) FEC [150]. In optically amplified coherent links, three main noise sources must be considered: transceiver noise, amplified spontaneous emission (ASE) noise introduced by optical amplifiers, and NLI arising from

the Kerr nonlinearity of the fiber. Segregating these contributions is essential for system optimization, since the per-span optimal transmit power depends on the ratio between NLI and ASE noise [149]. While transceiver noise can be quantified through factory calibration (e.g., back-to-back measurements), separating ASE from NLI remains a significantly more challenging task.

A variety of approaches have been proposed in the literature to estimate the contribution of NLI. One line of work exploits the observation that *a fraction* of NLI does not behave as AWGN [81]. Under this assumption, NLI power can be inferred from the CPE algorithm [151] or from time-domain correlations in the received constellation [152–154], with regression techniques then used to retrieve the actual NLI value. However, these methods generally provide accurate results only in controlled scenarios, such as simulations without phase noise or experiments with strong NLI, and they require prior knowledge of the link and transmission parameters.

An alternative strategy was proposed in [155], where a calibration factor based on amplitude noise correlation is incorporated into the EVM calculation to suppress the effect of NLI and estimate the OSNR. The drawback is that this approach requires a calibration procedure, and the calibration factor depends on link length and modulation format. Other methods introduce notches either in the time domain [156] or in the frequency domain [157] of the transmitted signal. These techniques tend to be more robust and effective, but they still require modifications at the transmitter and calibration steps, preventing purely passive estimation from the receiver DSP. More recently, [158] proposed leveraging the distinct spectral properties of ASE and NLI and their correlation to jointly estimate the two contributions. Although this method still requires calibration, it avoids transmitter modifications and typically relies on smaller datasets than machine learning approaches. Nevertheless, its calibration parameters remain sensitive to frequency offsets, shaping filter roll-off, and WDM channel positioning.

A further family of approaches employs deep learning techniques to infer NLI directly from the received constellation [159–161] or from SNR fluctuations induced by PDL [162]. While promising, these methods are not grounded in physical models, which makes their interpretation and generalization across different network scenarios challenging. Moreover, although they can reduce computational complexity, this advantage is offset by the substantial effort required for prior data collection. Fundamentally, the limitations of all these approaches stem from two key factors: (1) under typical operating conditions, NLI is relatively weak, and (2) most of its non-AWGN components are effectively mitigated by standard DSP blocks, such as CPE [163, 164]. This motivates the search for alternative solutions.

In recent years, DLM has emerged as a promising technique for monitoring optical links along the propagation direction [55, 59, 66]. Demonstrated applications include the estimation of power profiles, CD maps, amplifier gain spectra and tilt, filter impulse responses [63], and PDL (see Sec. 2.1). Moreover, DLM requires only the information already available in the receiver DSP, making it highly suitable for integration into coherent transceivers [165]. In particular, LLS-based LPM [66] enables estimation of the absolute power evolution of the signal along the link. When combined with simplified NLI models such as the GN model [149], this capability allows accurate estimation of NLI power. By integrating this estimate with transceiver calibration data and overall SNR measurements, the three major noise sources can be effectively segregated. A first suggestion in this direction was presented in [63], while an initial implementation in [132] applied the SSFM using power profiles estimated through LPM. However, this approach requires re-propagation of all WDM channels, which are generally unavailable at the receiver, leading to high complexity. Another possibility is to leverage LPM to estimate link parameters for use in analytical NLI models (e.g., GN or EGN models). While possible in principle, this is an indirect estimation method, meaning that inaccuracies in link parameters can propagate into the NLI model and degrade its performance. The simplified model proposed in [166] can provide a quick assessment of how such inaccuracies impact system-level metrics.

3.2 Proposed method

For the reasons above, this work proposes an alternative and more direct approach, showing that the estimation of NLI power is inherently embedded within LLS-based LPM. It is useful to recall that, after propagation through a coherent optical link, the overall SNR, in linear units, evaluated on the received constellation after DSP can be written as [149]:

$$\mathrm{SNR} = \left(\mathrm{SNR}_{\mathrm{TRX}}^{-1} + \mathrm{OSNR}^{-1} + \mathrm{SNR}_{\mathrm{NL}}^{-1}\right)^{-1}, \tag{3.1}$$

where $\mathrm{SNR}_{\mathrm{TRX}}$ accounts for transceiver noise, OSNR for ASE noise (evaluated over a reference bandwidth equal to the symbol rate), and $\mathrm{SNR}_{\mathrm{NL}}$ for Kerr-induced NLI. The focus of our estimation is precisely $\mathrm{SNR}_{\mathrm{NL}}$.

3.2.1 Nonlinear Interference Estimation with LLS-based LPM

In the LLS-based LPM algorithm, the information on NLI is contained in the term $\mathbf{A}_1[L]$ of (1.19). According to the eRP1 formulation, the accumulated NLI at the receiver can be expressed as the sum of all local contributions $\mathbf{g}(z)\gamma'(z)$ along the link, after propagation through the residual chromatic dispersion (i.e., each nonlinear branch in Fig. 1.7):

$$\mathbf{A}_1(L,t) = \int_0^L \mathbf{g}(z,t)\gamma'(z), \mathrm{d}z, \tag{3.2}$$

where t denotes the continuous time variable. The discretized form of (3.2) is provided in Sec. 1.4.3, where $\mathbf{g}_k = \mathbf{g}(z_k, n)$, $\gamma'_k = \gamma'(z_k)$, and $\Delta z_k = \mathrm{d}z$.

The core idea of the proposed estimation method is to recover this perturbation term and use it to infer the corresponding $\mathrm{SNR}_{\mathrm{NL}}$. Importantly, this estimation is already embedded within the LLS-based LPM algorithm. Specifically, the optimization problem in (1.18) estimates the γ' that minimizes, in the least-squares sense, the difference between $\mathbf{A}_1[L]$ and $\mathbf{A}_{\mathrm{ref},1}[L]$. Thus, computing $\hat{\gamma}'$ from (1.22) and multiplying it by $\mathbf{G}$ directly provides a discrete-time estimate of (3.2):

$$\hat{\mathbf{A}}_1[L] = \mathbf{G}\hat{\gamma}'. \tag{3.3}$$

From this expression, $\mathrm{SNR}_{\mathrm{NL}}$ can be readily computed. Let the power spectral densities (PSDs) of (3.3) and the reference signal be denoted by $G_{\hat{A}1}(f)$ and $G_{A_{\mathrm{ref}}}(f)$, respectively. Assuming a flat PSD within the bandwidth of interest, the nonlinear SNR can be written as:

$$\mathrm{SNR}_{\mathrm{NL}} = \frac{G_{A_{\mathrm{ref}}}(0)}{G_{\hat{A}_1}(0)}. \tag{3.4}$$

An example of this computation is displayed in Fig. 3.1. Equations (3.3) and (3.4) offer several advantages. First, they provide closed-form expressions, avoiding the need for SSFM simulations or other computationally intensive numerical techniques to estimate nonlinear noise. Second, the impact of ASE noise is limited, as it only influences $\hat{\gamma}'$ in (3.3) and its effect can be mitigated by averaging multiple estimated profiles and/or increasing the number of samples used in the LPM algorithm [66]. Finally, the required system knowledge is minimal: apart from the accumulated chromatic dispersion, which is typically available from the coherent transceiver's CDC stage or can be straightforwardly estimated [143].

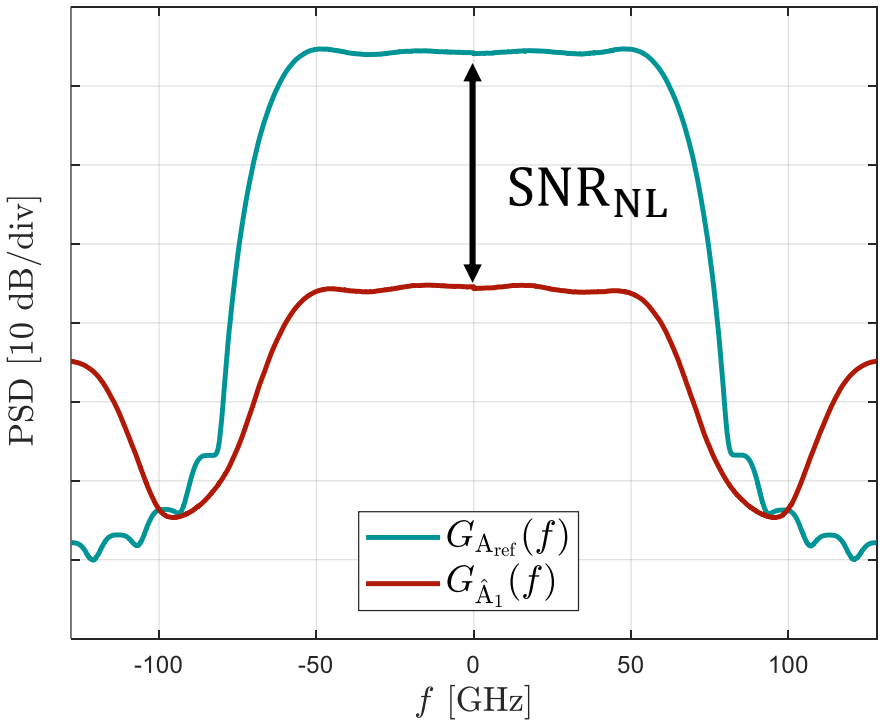

Fig. 3.1 Visualization of $\mathrm{SNR}_{\mathrm{NL}}$ computation with proposed method from $\hat{\mathbf{A}}_1$ and $\mathbf{A}_{\mathrm{ref}}$ PSDs.

3.2.2 Preliminary Numerical Analysis

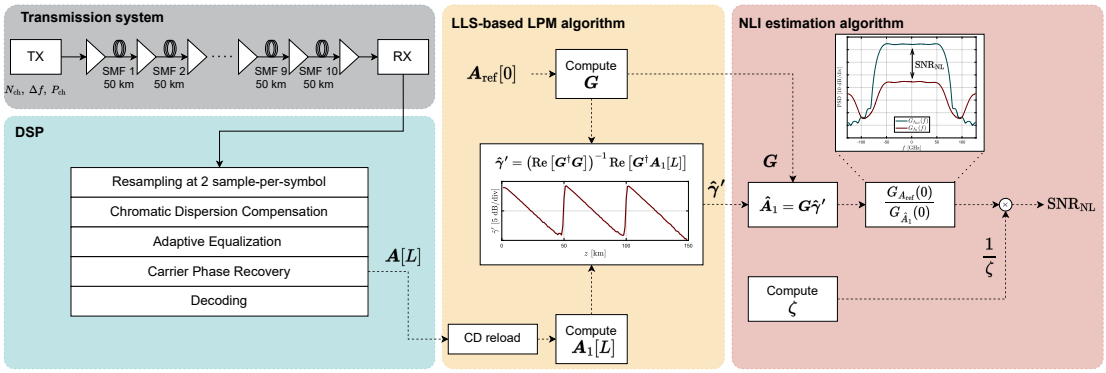

Fig. 3.2 Schematic of the simulation setup and DSP used to validate the proposed method. Moreover, the fundamental equations to implement LLS-based LPM and NLI estimation are also displayed.

A preliminary numerical analysis is carried out using the setup shown in Fig. 3.2, where all fundamental steps for implementing LLS-based LPM and NLI estimation are also illustrated. Note that the parameter ζ is set equal to 1 for this preliminary step and its meaning will be explained in the following. The test signal consists of a WDM comb of DP-64QAM channels, each modulated at a symbol rate of $R_s = 128$ Gbaud and shaped

with a square-root raised-cosine filter with roll-off $\rho = 0.1$. The simulations span over a range of system parameters: number of channels $N_{\text{ch}} \in \{1, 5, 11, 21\}$, per-channel power $P_{\text{ch}} \in [-2, \ldots, +5]$ dBm, and channel spacing $\Delta f \in \{150, 175, 200\}$ GHz. Unless otherwise specified, the channel of interest (COI) is the central channel.

The transmission link consists of 10×50-km spans of standard G.652 SMFs, with attenuation $\alpha_{\text{dB}} = 0.2\,\text{dB/km}$, chromatic dispersion coefficient $\beta_2 = -21.28\,\text{ps}^2/\text{km}$, and nonlinearity coefficient $\gamma = 1.3\,1/\text{W/km}$. Each span is followed by an EDFA with a noise figure of $F = 5\,\text{dB}$, operated in constant output power mode. Fiber propagation is simulated using SSFM [85]. At the receiver, the signal is processed through a standard DSP chain performing resampling at two samples per symbol, CDC, adaptive equalization, and CPE. The output of the CPE stage is then extracted and provided as input to the LLS-based LPM block and the subsequent NLI estimation algorithm. An example of estimated power profiles for the single-channel scanario is displayed in Fig. 3.3.

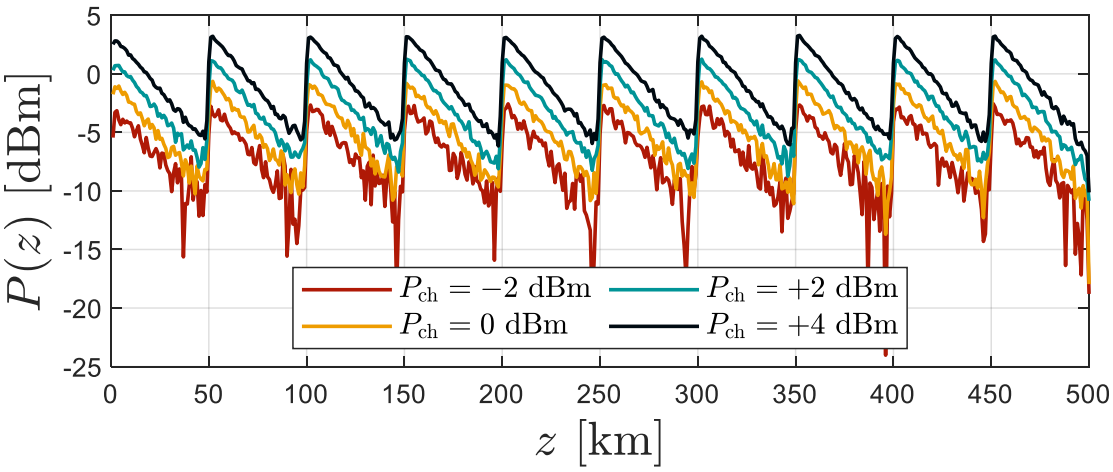

Fig. 3.3 Example of estimated power profiles in the single-channel scenario.

All results are compared to those obtained from a GN model [82], run in parallel to the simulations and used as a reference. It should be noted that this GN model implementation does not include modulation-format effects. For the validation, all combinations of N_{ch} and P_{ch} were tested, while fixing the channel spacing at $\Delta f = 200\,\text{GHz}$.

The results for NLI estimation are reported in Fig.3.4(a). For the single-channel scenario, the estimation proves to be highly accurate. However, as the number of WDM channels increases, a systematic bias emerges in the estimation, as illustrated in Fig. 3.4(b). This limitation stems from the intrinsic properties of the LPM algorithm itself: LPM relies solely on SCI for power profile estimation. All other impairments, including stochastic noise

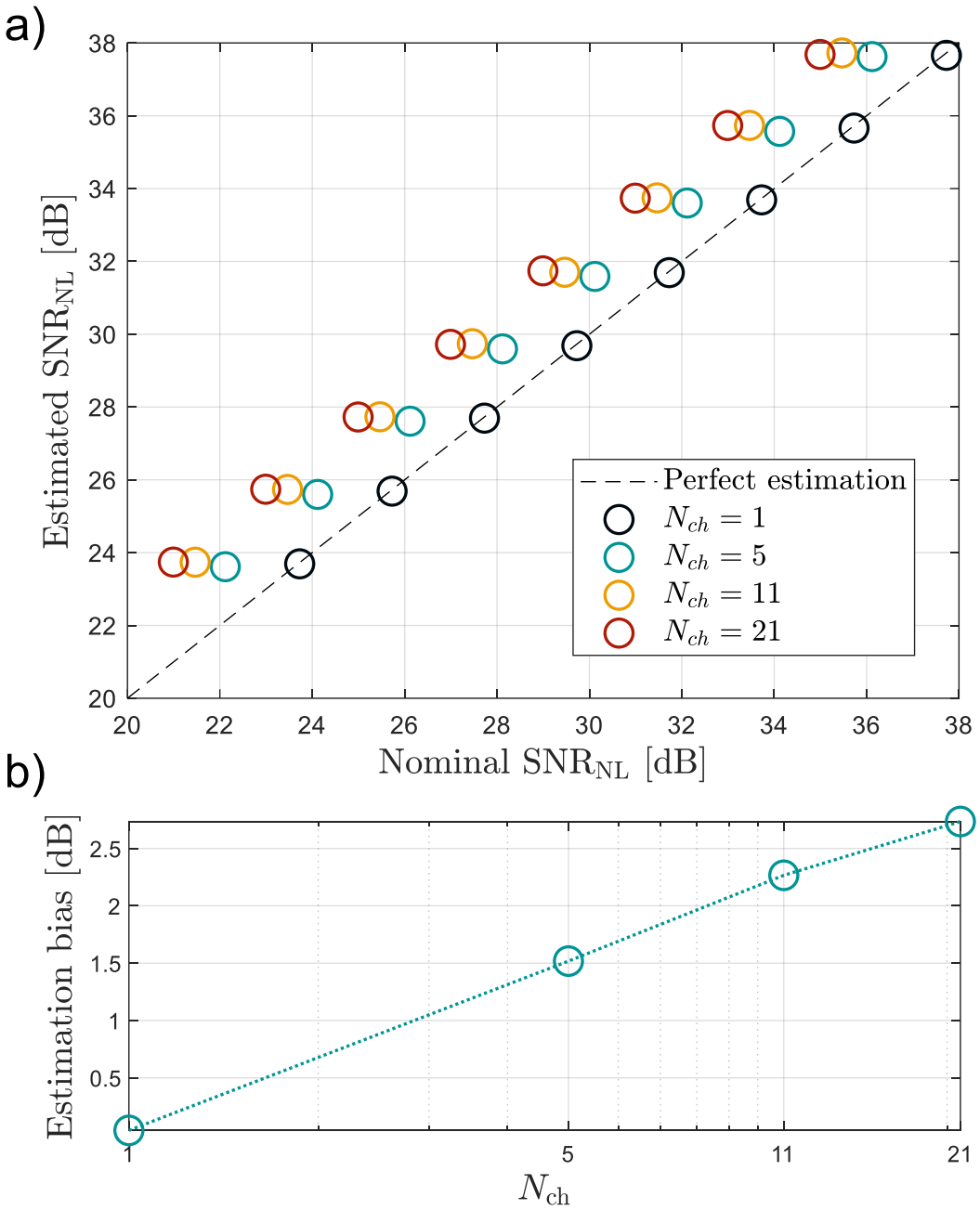

Fig. 3.4 a) Results of SNR$_{\mathrm{NL}}$ estimation using (3.4) (circles) and the GN model (black dashed line) over a 10×50-km SMF link at 128 GBaud per channel and $\Delta f = 200$ GHz for a varying number of WDM channels N_{ch} and P_{ch} spanning from -2 dBm to 5 dBm, with step 1 dB. b) Mean estimation bias with respect to nominal SNR$_{\mathrm{NL}}$ computed with GN model.

sources such as ASE or laser phase noise, as well as static distortions from transceiver implementation, are interpreted as noise by LPM. More in detail, XCI is also included in this category. Since information about interfering WDM channels is generally unavailable

at the receiver, and only the COI is virtually propagated in the LPM algorithm, the XCI contribution to the overall NLI cannot be directly estimated.

3.2.3 XCI-induced Bias Correction

As shown in the preliminary numerical analysis, the LLS-based algorithm estimates only the portion of NLI power arising from the nonlinear beating of the COI with itself, i.e., the SCI contribution. However, two additional NLI components must also be considered: XCI and MCI. In the case of long-haul, high-symbol-rate (i.e., ≥ 60 Gbaud) multi-channel transmission over uncompensated SMF links, MCI is generally negligible [57, 83, 84], whereas XCI remains significant and cannot be ignored. Consequently, to estimate the total NLI power, it is necessary to account for the XCI contribution. Without any loss of generality, we can define an XCI correction factor ζ as:

$$P_{\mathrm{NLI}} \approx P_{\mathrm{SCI}} + P_{\mathrm{XCI}} = P_{\mathrm{SCI}} \left(1 + \frac{P_{\mathrm{XCI}}}{P_{\mathrm{SCI}}}\right) = P_{\mathrm{SCI}} \cdot \zeta \tag{3.5}$$

With the knowledge of ζ and P_{SCI}, the full NLI power P_{NLI} can be estimated, obtaining a full segregation of the noise source. Moreover, including ζ into (3.4), the expression for $\mathrm{SNR}_{\mathrm{NL}}$ becomes:

$$\mathrm{SNR}_{\mathrm{NL}} = \frac{1}{\zeta} \frac{G_{A_{\mathrm{ref}}}(0)}{G_{\hat{A}_1}(0)}. \tag{3.6}$$

If all link parameters are known, the factor ζ can be directly obtained from any NLI model. For example, when the COI is the central channel of a homogeneous WDM comb with N_{ch} channels, each modulated at a symbol rate R_{s} and spaced by Δf, the simple closed-form approximation provided by the GN model [82, Eq. (15)] can be applied, yielding

$$\zeta \approx \frac{\operatorname{asinh}\left(\frac{\pi^2}{2}\beta_2 L_{\mathrm{eff,a}} R_{\mathrm{s}}^2 N_{\mathrm{ch}}^{\frac{2R_{\mathrm{s}}}{\Delta f}}\right)}{\operatorname{asinh}\left(\frac{\pi^2}{2}\beta_2 L_{\mathrm{eff,a}} R_{\mathrm{s}}^2\right)}. \tag{3.7}$$

This expression depends on the symbol rate and the frequency spacing of the channel, as well as on the fiber's dispersion (β_2) and attenuation ($L_{\mathrm{eff,a}} = 1/2\alpha$, where α is the field attenuation parameter). Then, assuming standard conditions (i.e., transmission over SMF of

modern coherent optical channels), in [166, Eq. (23)] the authors provided an even simpler approximation:

$$\Gamma_{\mathrm{NLI}} \cong \frac{1.5 \cdot 10^{24}}{E_{\mathrm{ph}}^2} \frac{B_{\mathrm{opt}}^{1/4} \cdot \gamma^2}{K_{\mathrm{S}} \cdot \alpha_{\mathrm{dB}} \cdot D^{5/6}} \tag{3.8}$$

where Γ_{NLI} is the normalized NLI efficiency, $\mathrm{B_{opt}}$ is the overall occupied optical bandwidth and, in the case of homogeneous configuration of the WDM comb, can be written as $\mathrm{B_{opt}} = \mathrm{N_{ch}}\Delta f$. A more detailed definition of the parameters can be found in [166], as they are not required for the present derivation. This allows to compute ζ as the ratio between (3.8) evaluated in the multi-channel and the single-channel scenarios, i.e.,

$$\zeta \approx \sqrt[4]{N_{\mathrm{ch}}}\,. \tag{3.9}$$

The error introduced by this approach is relatively large, as it relies on a higher level of approximation. Nevertheless, it remains effective while requiring knowledge of only one additional transmission parameter (the number of propagating WDM channels). A comparison of the two methods is shown in Fig. 3.5, which reports the mean estimation bias from (3.4) across different combinations of N_{ch} and Δf.

It should be emphasized that both (3.7) and (3.9) are derived under the assumption of homogeneous WDM combs. This assumption is considered valid in the preliminary numerical analysis, as well as in all subsequent sections. Such an assumption is reasonable for terrestrial WDM networks, where ASE noise loading [167] and the use of ROADMs ensure power equalization among channels along the link. For specific cases requiring alternative power loading strategies and/or coarsely spaced WDM channels, more general NLI models should be adopted to account for these conditions.

It is worth noting that none of these approximations require knowledge of the nonlinear parameter γ, which is generally difficult to estimate. Both formulations, however, assume the COI corresponds to the central WDM channel. In principle, expressions for ζ associated with non-central channels could be derived from closed-form NLI equations, though these would become considerably lengthy despite remaining analytical. As will be demonstrated in the next sections, for the specific purpose of noise segregation in modern high-symbol-rate ($\geq$ 60 Gbaud) coherent systems, precise estimation of ζ is not critical. Instead, a coarse approximation can be obtained by introducing a correction term to (3.9), yielding

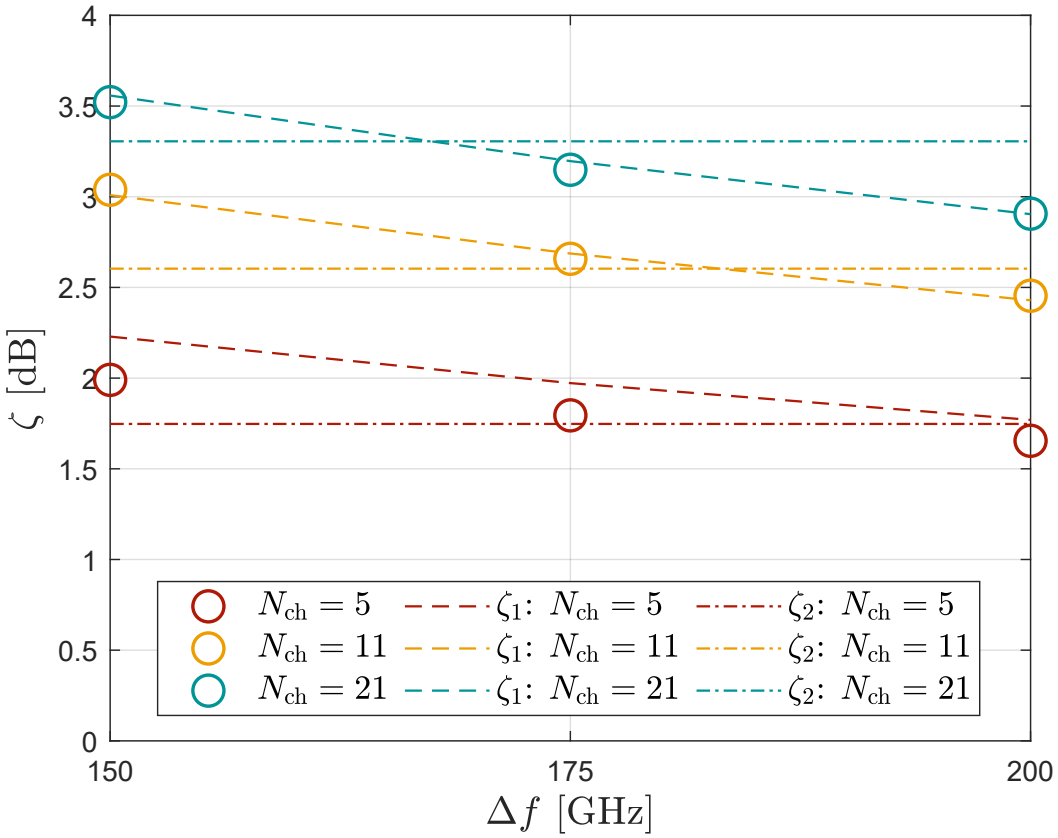

Fig. 3.5 Accuracy of ζ from (3.7) (dashed line), here indicated as ζ_1, and (3.9) (dash-dotted line), here indicated as ζ_2, for varying number of channels N_{ch} and channel spacing Δf compared to previously computed estimation bias arising from (3.4) (circles).

$$\log_{10}(\zeta) \approx \frac{1}{4}\log_{10}(N_{\mathrm{ch}}) + a\left[\log_{10}\left(\frac{B_{\mathrm{L}}}{B_{\mathrm{R}}}\right)\right]^2. \tag{3.10}$$

In this equation, B_{L} and B_{R} are, respectively, the optical bandwidth at the left and right of the COI. These quantities allow to introduce a dependence of ζ on the position of the channel within the WDM comb. The parameter a can be estimated through a simple linear regression from a dataset of results, similar to the procedure followed in [166]. To do this, we built a dataset comprising 1 440 different scenarios, by changing the number of 64-Gbaud WDM channels from 3 to 45, and the number of SMF spans from 1 to 20. For each span in each scenario, the length L_s, attenuation and dispersion were randomly selected, assuming a Gaussian distribution with a standard deviation of 5% relative to the nominal values of $L_s = 70\,\mathrm{km}$, $\alpha_{\mathrm{dB}} = 0.2\,\mathrm{dB/km}$ and $\beta_2 = -22.77\,\mathrm{ps}^2/\mathrm{km}$.

All scenarios were simulated using the closed-form model (CFM) NLI model [145], and the value ζ was extracted for each of them. After applying a linear regression on (3.10), we obtained $a \approx -0.0475$.

It is worth noting that, although this constitutes a relatively rough approximation of ζ, it offers the advantage of being a simple linear expression that requires only a minimal set of parameters. Its applicability, however, is restricted to C-band transmissions, as in UWB scenarios, such as C+L systems, the effect of ISRS becomes non-negligible. Moreover, the proposed approximations do not include the dependence on modulation , since they are based on the GN model. The effectiveness of this approximation will be assessed in the following section under more realistic simulation conditions. As previously mentioned, whenever a more accurate estimation of ζ is needed, standard NLI models can be employed, provided that the required parameters are either known or can be reliably estimated.

3.3 Numerical Validation

This section presents an extensive numerical validation of the proposed method under two distinct system configurations. In particular, the analysis includes non-central WDM channels, employs a more realistic fiber propagation model, and considers transmission distances representative of the typical reach of the chosen modulation format.

3.3.1 Simulation Setup

The first configuration of the transmitted DP-16QAM WDM signal consists of $N_{\text{ch}} = 30$ channels at $R_s = 64$ Gbaud with channel spacing $\Delta f = 100\,\text{GHz}$, while the second configuration uses $N_{\text{ch}} = 15$ channels at $R_s = 128$ Gbaud with spacing $\Delta f = 200\,\text{GHz}$. In both cases, the pulses are shaped with an SRRC filter with roll-off $\rho = 0.1$. To evaluate different SNR_{NL} values, the per-channel launch power P_{ch} is varied from $-1\,\text{dBm}$ to $5\,\text{dBm}$ in $2\,\text{dB}$ steps, covering the optimal operating power for both configurations.

In addition, transmitter phase noise with linewidth $\Delta\nu = 50\,\text{kHz}$ is included and modeled as a Wiener process. The signal is propagated over a 17×65-km SMF link, with each span followed by an EDFA with a noise figure $F = 5\,\text{dB}$, operated in constant output power mode to equalize the per-channel power. Frequency-dependent power attenuation α_{dB} and chromatic dispersion β_2 are considered, with values obtained from experimental characterization of four G.652 SMF fiber spans, shown in Fig.3.6. These four spans are cyclically alternated

in the numerical setup, effectively emulating a recirculating loop. ISRS is also modeled, although its impact is negligible due to the relatively narrow optical bandwidth of 3 THz. At the receiver, the signal is resampled at 2 sample/symbol and processed by a standard

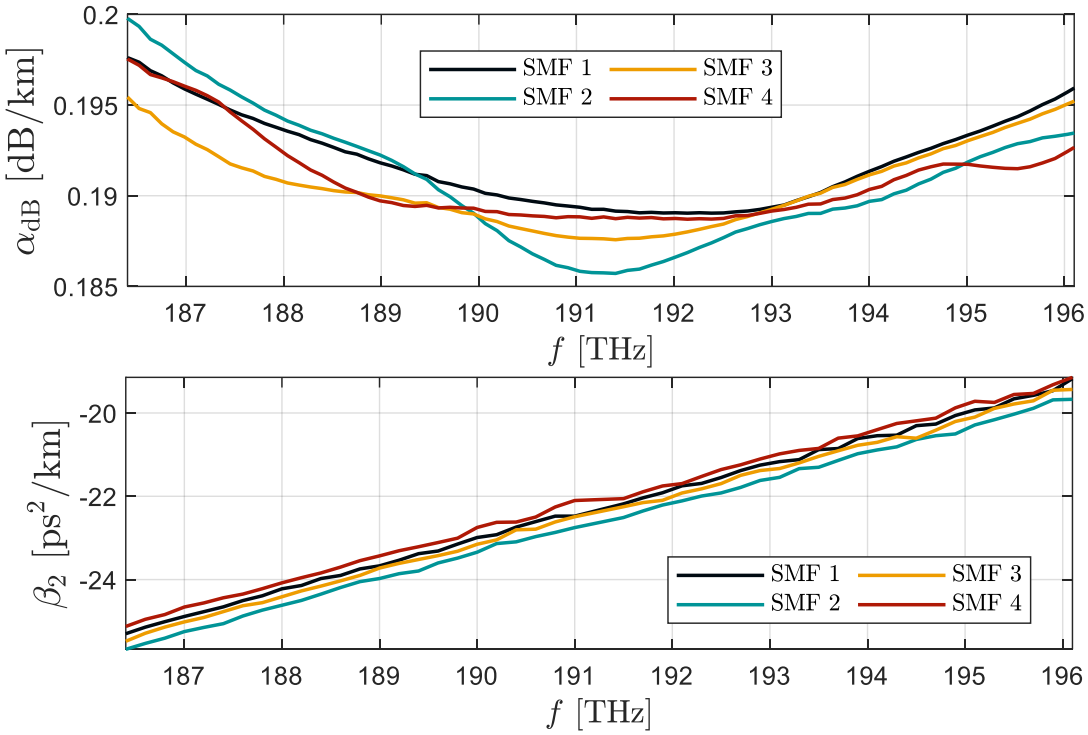

Fig. 3.6 Measurements of frequency-dependent power attenuation coefficient α_{dB} and chromatic dispersion coefficient β_2 of the four SMF fibers used in the simulation setup.

DSP chain, including CD compensation, LMS-based adaptive equalization, and BPS for CPE. The CPE output is then used as input for LPM and the subsequent NLI estimation algorithm. Approximately 2^{17} samples are employed for LPM, with spatial steps $\Delta z = 2\,\mathrm{km}$ and $\Delta z = 1\,\mathrm{km}$ in the two configurations. $\mathrm{SNR}_{\mathrm{NL}}$ is estimated using (3.6) and (3.10), from subsets of 7 and 6 channels, respectively. Since all transmission parameters are known, the GN model [82] is used in parallel to provide reference values for comparison against the proposed NLI estimation method.

3.3.2 Numerical Results

The results for the 64-Gbaud and 128-Gbaud configurations are shown in Fig. 3.7(a) and Fig. 3.7(b), respectively.

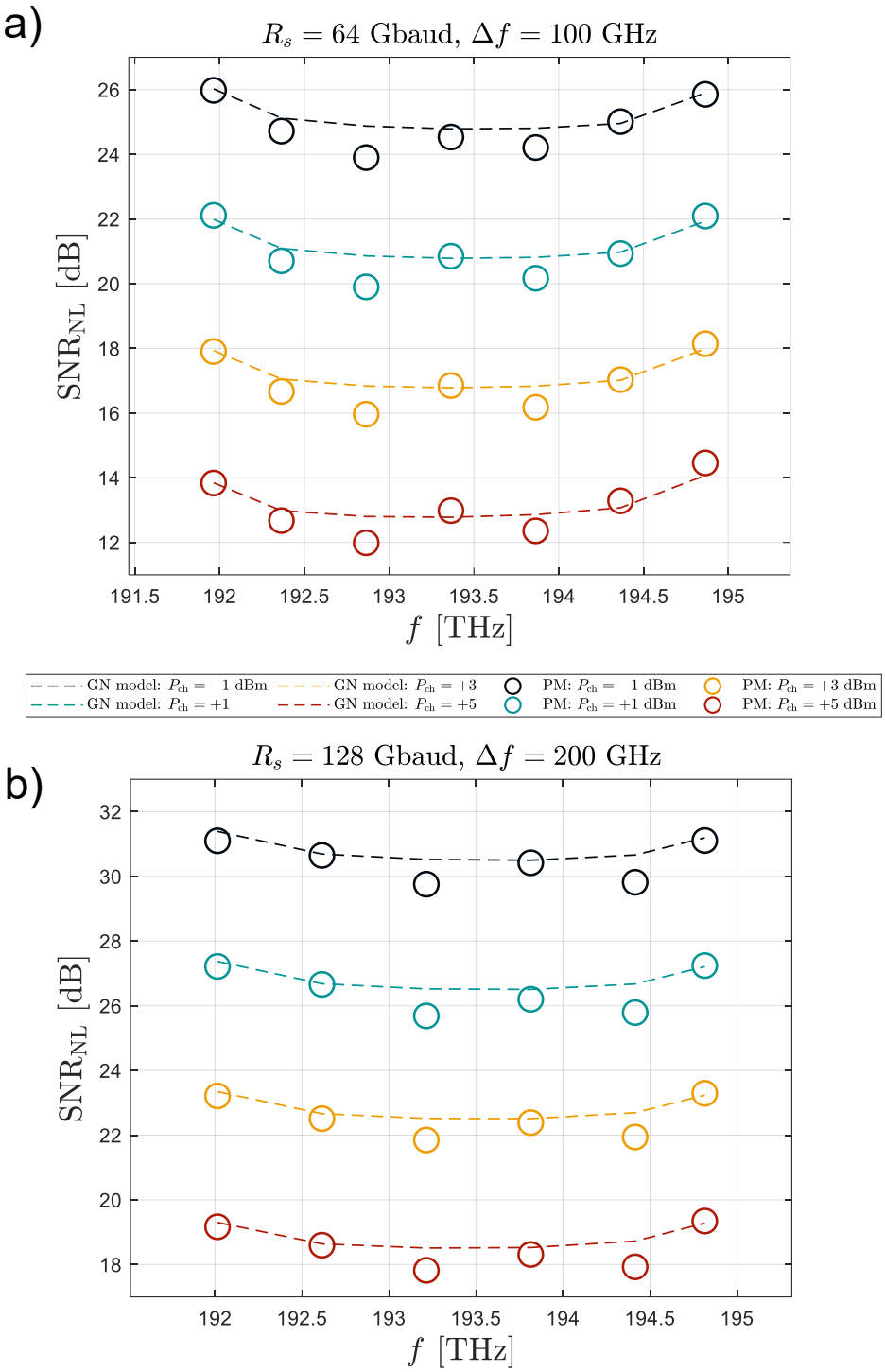

Fig. 3.7 Numerical results of $\mathrm{SNR}_{\mathrm{NL}}$ estimation over a 17×65-km SMF link under two system configurations: a) $N_{\mathrm{ch}} = 30$, $R_s = 64$ Gbaud and $\Delta f = 100$ GHz; b) $N_{\mathrm{ch}} = 15$, $R_s = 128$ Gbaud and $\Delta f = 200$ GHz. In both configurations, $P_{\mathrm{ch}} \in \{-1, +1, +3, +5\}$ dBm. PM: proposed method.

In both cases, the estimated $\mathrm{SNR}_{\mathrm{NL}}$ values align well with those obtained from the GN model, used as a reference. Some oscillations are visible, likely due to the more challenging conditions under which the LPM algorithm operates. The power profiles used in (3.3) are highly noisy because of the significant ASE accumulation during propagation. Additional impairments, such as phase noise, further degrade these profiles. Nevertheless, the reduced quality of the profiles does not significantly compromise the accuracy of the proposed method: the mean absolute error relative to the reference remains around 0.3 dB in both configurations, while the maximum errors are 0.97 dB and 0.88 dB, respectively. Importantly, the estimated values track the correct NLI evolution across all tested conditions and COIs. This also validates the correction in (3.10), which effectively compensates for XCI in non-central channels, typically less affected by XCI because of their fewer neighboring channels. Further validation will be provided in the following, where the same setup is used in an experimental scenario.

It is worth noting that the accuracy required by the XCI correction factor decreases as the symbol rate increases. In this section, results were obtained at 64 and 128 Gbaud, corresponding to 30 and 15 WDM channels, respectively. For central channels, those most impacted by XCI, the corresponding ζ values are 3.7 dB and 2.9 dB. This indicates that the relative contribution of XCI compared to SCI diminishes with higher symbol rates (or equivalently, with fewer channels) [122]. Given the current industrial trend toward higher symbol rates (e.g., 200-Gbaud transceivers [168]), the XCI-to-SCI ratio, expressed by ζ, is expected to further decrease. While these observations are made on a ~ 3 THz WDM bandwidth scenario, the same reasoning extends to full C-band transmissions using (3.10).

3.4 Experimental Validation

Following the numerical validation, the accuracy of the proposed algorithm was investigated in two experimental scenarios. The first experiment was conducted over a transmission link operating under conditions that are generally favorable to LPM algorithms [55], namely short propagation distance, high per-channel launch power, and limited optical bandwidth. The second experiment was designed to represent a more realistic and challenging scenario, with a transmission distance approaching the maximum reach of the employed modulation format.

In both cases, the experiments were carried out using commercial coherent transceivers over two different point-to-point transmission lines. The algorithm was implemented offline, while the resulting estimates were compared against the SNR values provided by the real-time

DSP of the transceivers, thus enabling a realistic assessment of the accuracy achievable in practical network conditions.

3.4.1 Transmission over a 300-km Link

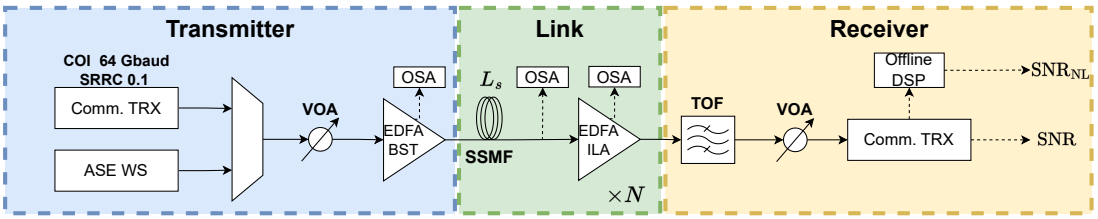

Fig. 3.8 Experimental setup. WS: wave shaper; VOA: variable optical attenuator; BST: booster; OSA: optical spectrum analyzer; ILA: in-line amplifier; TOF: tunable optical filter.

The experimental setup is reported in Fig. 3.8. The COI is a DP-QPSK 64-Gbaud signal, shaped with an SRRC filter with roll-off 0.1 and centered at $f = 193.3\,\mathrm{THz}$. Interfering WDM channels are generated by filtering ASE noise with a WaveShaper (WS) [169], resulting in an 18-channel WDM comb with a spacing of 100 GHz across the C band. The signal is amplified by a first booster EDFA (BST) and transmitted over an optical link consisting of $N = 5$ spans of SSMF, each of nominal length $L_s = 60\,\mathrm{km}$. At the end of each span, an in-line EDFA (ILA) operating in automatic gain control mode compensates for the span loss. OSAs are connected to the monitoring ports of the EDFAs and to 90/10 splitters placed after each span to track the PSD evolution of the propagating WDM signal.

At the receiver, the COI is isolated by a tunable optical filter (TOF) and its power adjusted with a variable optical attenuator (VOA) before being received by a commercial transceiver. The signal is sampled at 96 GSa/s by the transceiver's ADC and the acquired samples are downloaded for offline processing. After front-end corrections and resampling at 2 samples per symbol, the DSP chain performs CDC, FOC, LMS-based 2×2 MIMO fractionally-spaced equalization, and Viterbi–Viterbi (4th power) CPE. The output of the CPE stage is extracted, CD is reloaded, and the signal is fed to the LPM algorithm. The number of samples used as input is 2^{17}, with the spatial resolution set to $\Delta z = 2\,\mathrm{km}$.

To span a wide range of $\mathrm{SNR}_{\mathrm{NL}}$ values, the per-channel power P_{ch} was varied between 0 dBm and +10 dBm, in 2 dB steps, using a VOA placed before the BST EDFA. For each condition, 100 power profiles were estimated and employed in the computation of (3.3) and (3.6), with the resulting values subsequently averaged.

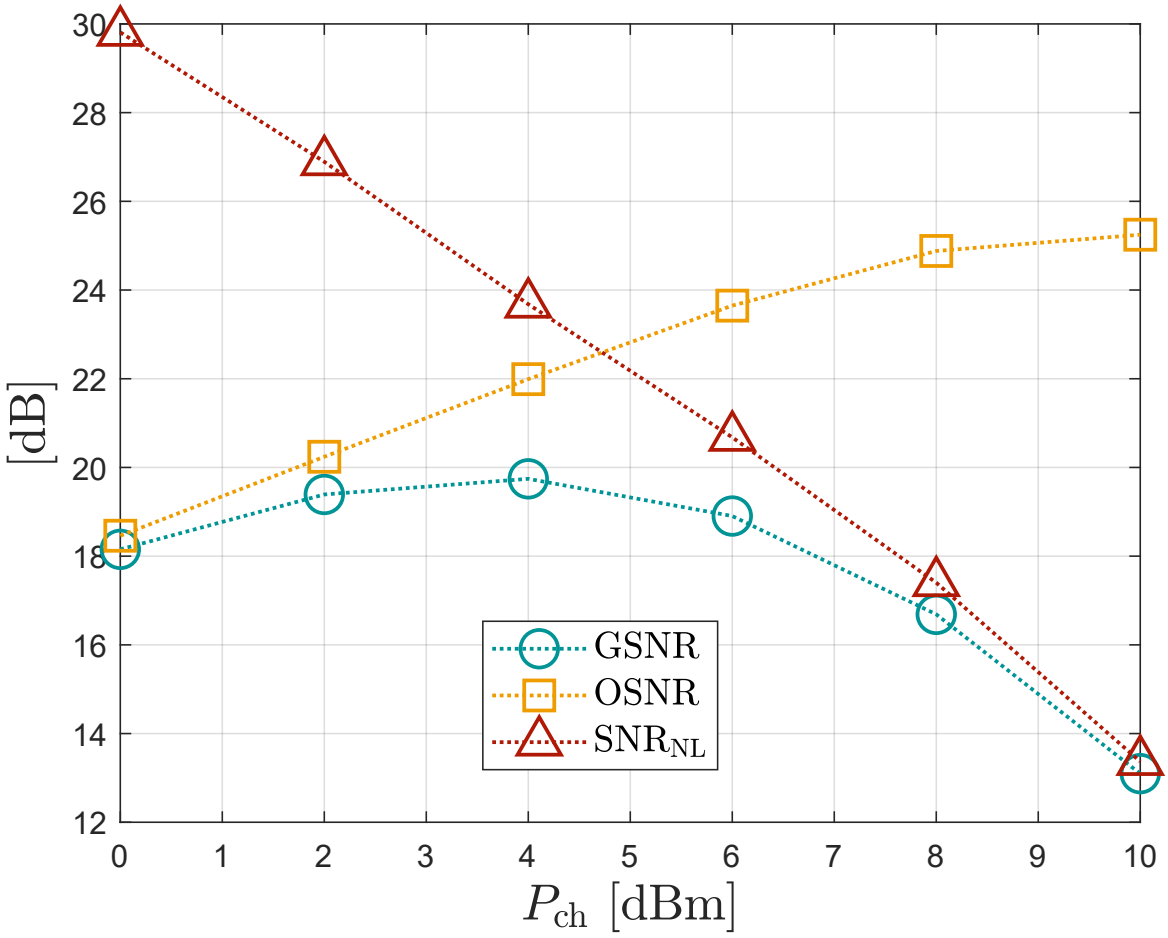

Fig. 3.9 Measured GSNR, OSNR and $\mathrm{SNR_{NL}}$ for each tested per-channel power P_{ch}.

Experimental measurements of the nonlinear SNR were also performed for validation. The overall SNR was extracted from the real-time DSP of the transceiver for each power level, while OSNR and $\mathrm{SNR_{TRX}}$ were obtained from OSA measurements and back-to-back acquisitions, respectively. The procedure in [170] yielded $\mathrm{SNR_{TRX}} = 19.77\,\mathrm{dB}$. The nonlinear contribution $\mathrm{SNR_{NL}}$ was then computed using (3.1). The corresponding results are shown in Fig. 3.9, where the generalized SNR (GSNR) [171] is defined as $\mathrm{GSNR} = (\mathrm{SNR}^{-1} - \mathrm{SNR_{TRX}}^{-1})^{-1}$. Note that OSNR tends to saturate around 26 dB at high powers, due to noise added by the transceiver and by the booster and pre-amplifier EDFAs.

The estimated values of $\mathrm{SNR_{NL}}$ are compared with the measured ones in Fig. 3.10, together with the absolute estimation error. The results confirm the consistency of the proposed method with the experimental measurements. The absolute error remains below 0.6 dB across all cases, with a root-mean-square error (RMSE) of approximately 0.4 dB.

Furthermore, the simple correction factor in (3.9) is shown to be effective in compensating for the estimation bias induced by XCI in the considered transmission system.

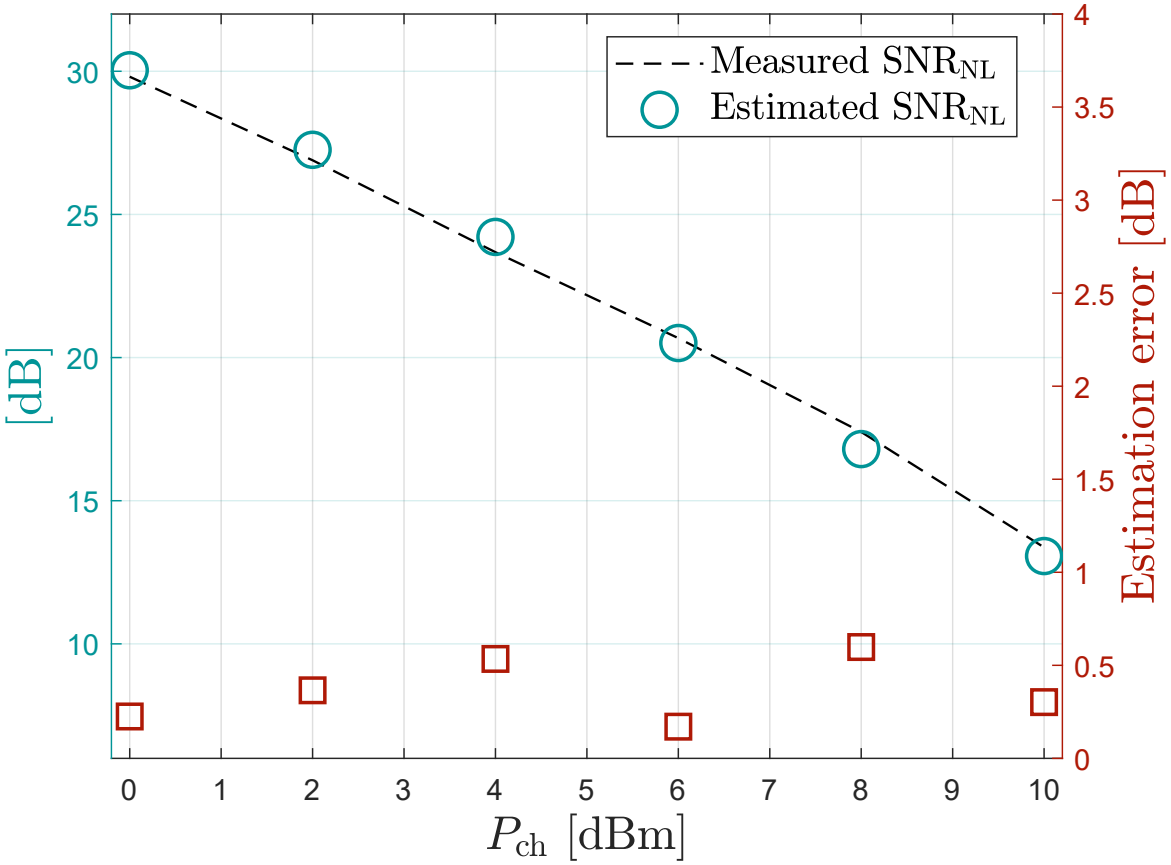

Fig. 3.10 Comparison between measured (dashed black) and estimated (blue circles) $\mathrm{SNR}_{\mathrm{NL}}$ with corresponding absolute estimation error (red squares).

3.4.2 Transmission over a 1100-km Link

The setup employed for this experiment is similar to that shown in Fig. 3.8, with minor modifications to the system configuration. A DP-16QAM 64-GBaud WDM signal composed of $N_{\mathrm{ch}} = 30$ channels spaced by $\Delta f = 100\,\mathrm{GHz}$ is transmitted. The per-channel power P_{ch} is varied between $-1\,\mathrm{dBm}$ and $5\,\mathrm{dBm}$, in $2\,\mathrm{dB}$ steps. The proposed method is applied to three COIs, located at $191.8\,\mathrm{THz}$, $193.2\,\mathrm{THz}$, and $194.7\,\mathrm{THz}$, corresponding to one central channel and the two outermost channels of the WDM comb. These COIs are selected to provide an experimental validation of (3.10), as they experience the most diverse XCI contributions to NLI during propagation. The signal is propagated over $N = 17$ spans of SSMF, each with a nominal length of $L_s = 65\,\mathrm{km}$. At the receiver, the DSP chain is implemented as in

the previous experiment, with the only difference being that CPE is implemented as BPS. Approximately 2^{17} samples are processed at the input of the LPM algorithm, with a spatial resolution of $\Delta z = 2\,\text{km}$. For each tested channel and power level, 100 profiles are estimated and averaged to obtain the final SNR_{NL}. Averaged power profiles for the first WDM channel are shown in Fig. 3.11.

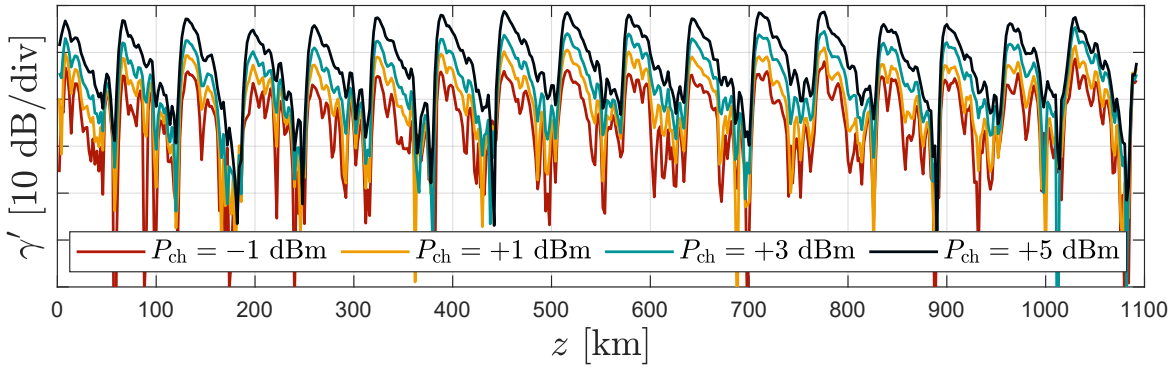

Fig. 3.11 Average relative power profiles γ' for all tested per-channel power levels.

Two approaches are adopted for validation. The first consists of a direct comparison between the estimated values and those obtained from the CFM model [145]. Unlike the model versions used in the numerical validations, this implementation accounts for modulation-format dependence. To this end, all fiber parameters required by the model, i.e., attenuation α, dispersion β_2, and nonlinear coefficient γ, were measured span by span: α and β_2 with an OTDR, and γ with the method of [170]. This strategy was chosen because the higher measurement uncertainties of the setup prevented a reliable measurement of SNR_{NL}, as done in the previous experiment. The results, shown in Fig. 3.12, indicate a mean absolute error of $\sim 0.5\,\text{dB}$ and an RMSE of $0.6\,\text{dB}$ across all conditions, with maximum errors consistently below $0.9\,\text{dB}$. The correction introduced in (3.10) effectively captures the diverse NLI evolution of the COIs even in this challenging scenario.

The second validation approach focuses on the practical accuracy of launch-power optimization enabled by noise segregation using the estimated SNR_{NL}. For this purpose, noise segregation is performed on the first WDM channel by combining the constellation SNR from the transceiver, SNR_{TRX} from back-to-back measurements ($\text{SNR}_{\text{TRX}} = 19.59\,\text{dB}$), SNR_{NL} from (3.6), and OSNR obtained by inverting (3.1). It should be emphasized that the latter represents an indirect estimate, and thus its accuracy depends on the reliability of the other terms. To further validate SNR_{NL}, the same analysis is repeated using OSNR values measured directly by an OSA and by the commercial transceiver, the latter being capable

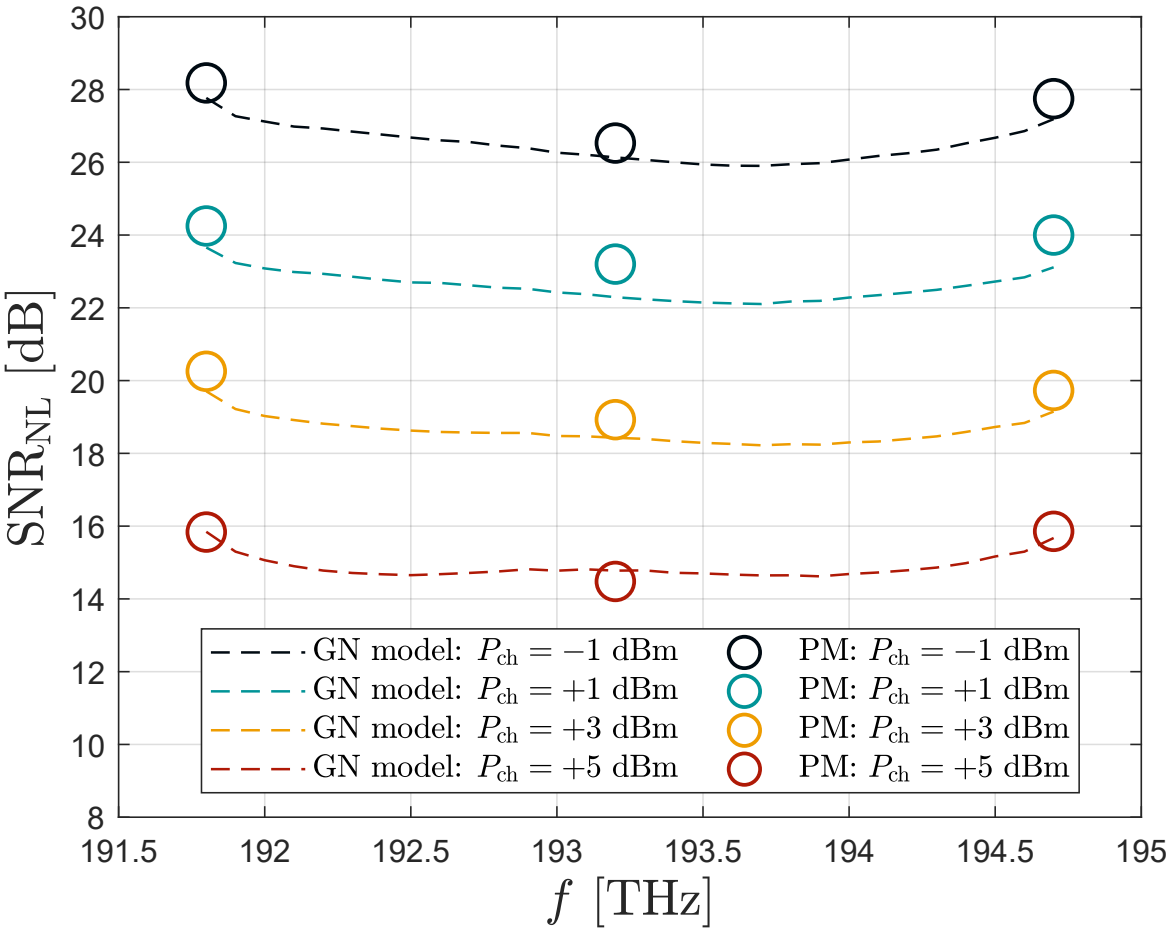

Fig. 3.12 Comparison between estimated $\mathrm{SNR}_{\mathrm{NL}}$ (circles) and the CFM GN model (dashed line) after propagation over the 17×65-km link. PM: proposed method.

of providing inline OSNR estimates [156]. This comparison highlights how the accuracy of launch-power optimization is influenced by the precision of the parameters involved

Using these quantities, the optimal power offset from the operating point can be estimated in logarithmic units with the so-called 3-dB rule [172–174], according to:

$$P_{\mathrm{opt}} - P_{\mathrm{ch}} = \frac{1}{3}\left(\mathrm{SNR}_{\mathrm{NL}} - \mathrm{OSNR} - 3\right). \tag{3.11}$$

Formally, the 3-dB rule is optimal only when applied to a single span, or to the end-to-end system in the case of all identical, equally-spaced channels, and identical spans [172, 173]. However, it proved to work relatively well and be quasi-optimal also under more general conditions, including standard C-band transmissions and more recently UWB transmissions (e.g., C+L+S+E systems) [174]. Given its simplicity, it will be the launch power optimization

strategy employed in this work. This expression in (3.11) provides a practical tool, as all required parameters are either estimated by the proposed method or directly available from the transceiver. Moreover, the $1/3$ factor reduces the sensitivity to errors in $\mathrm{SNR}_{\mathrm{NL}}$ and OSNR [149]. Results are shown in Fig. 3.13, where (3.11) is evaluated with OSNR values from (3.1), the transceiver, and the OSA. An inset reports the BER curve, with the optimum operating point identified at $P_{\mathrm{opt}} \simeq +1\,\mathrm{dBm}$. At this point, the distance predicted by (3.11) is approximately 0 dB, confirming the reliability of the $\mathrm{SNR}_{\mathrm{NL}}$ estimates. As expected, the use of indirect OSNR values slightly degrades the accuracy, reinforcing the preference for direct measurements when available. Nonetheless, this analysis demonstrates the practical applicability of the proposed method to optimize transmission parameters in realistic network scenarios.

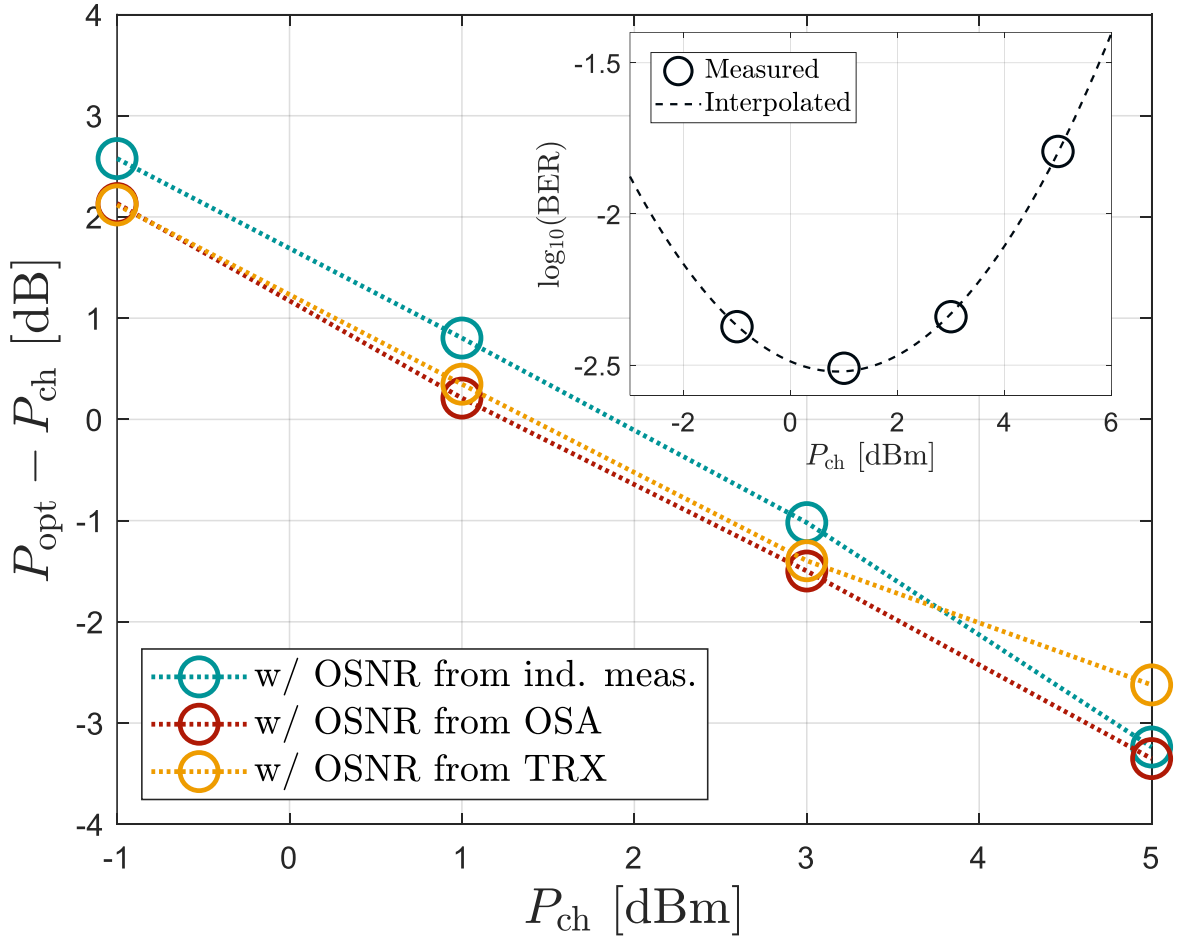

Fig. 3.13 Distance from optimal per–channel power P_{opt} – computed starting from estimated $\mathrm{SNR}_{\mathrm{NL}}$ and considering the OSNR from (3.1) (i.e., indirect measurement), that provided by the commercial transceiver and that measured from OSA – based on the 3-dB rule. In the inset, the real optimal power based on the BER supplied by the commercial transceiver is reported.

3.5 Implementation Penalties for LPM-based NLI Estimation

This section discusses the main implementation penalties associated with NLI estimation using LPM and presents both numerical and experimental validations.

3.5.1 Practical Implementation Limitations

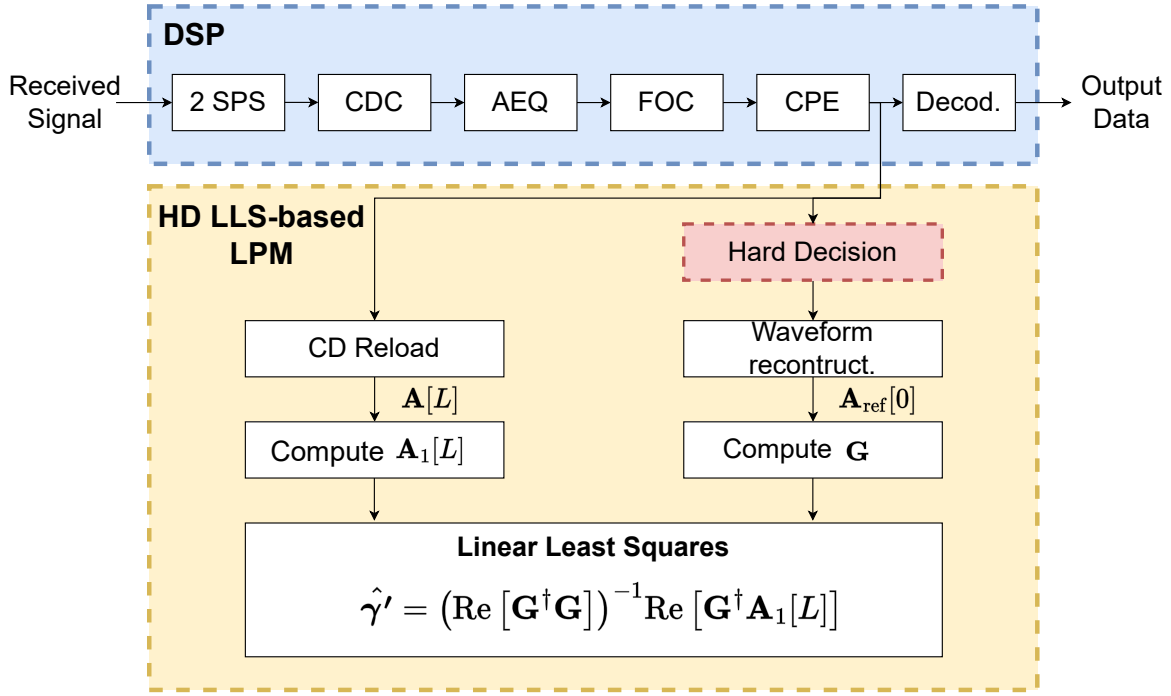

Fig. 3.14 Schematic of LLS-based LPM with the reference signal reconstructed from hard-decision symbols prior to FEC decoding

To compute the power profile, the LLS-based LPM algorithm requires only limited information from the receiver DSP [66]. The essential inputs are the received (noisy) constellation symbols and the corresponding noise-free transmit symbols. In a real-time receiver, however, direct access to the latter is not straightforward. The noise-free transmit sequence is required to construct the reference signal employed in the LPM algorithm. This sequence can be obtained through different approaches, such as using a priori knowledge (e.g., a pilot sequence) or reconstructing it after FEC decoding. Both strategies, however, present drawbacks: the former reduces the spectral efficiency of the transmission, while the latter is generally impractical due to the presence of large interleavers. Previous work

in [165], employing a correlation-based LPM algorithm, demonstrated that the transmit sequence can be replaced by a simple hard-decision (HD) of the received constellation. These modifications are illustrated in Fig. 3.14, which shows the schematic of the HD-based implementation of LLS-LPM.

This substitution was shown to introduce only a constant offset in the estimated power profile, which can be readily compensated. This offset originates from the fact that errors in the reference symbols introduce, in the LLS solution, an effect analogous to Tikhonov regularization, similar to [68]. This regularization induces a low-pass effect, which leads to an underestimation of the recovered power. The impact of this power offset on NLI estimation within the context of noise segregation is investigated, specifically using the LLS-based LPM approach. This aspect is critical, as the Kerr effect in optical fibers is intrinsically power-dependent, and any offset in the estimated power profile directly impacts the accuracy of Kerr-induced NLI estimation with the proposed method. A preliminary assessment is performed in a controlled simulation scenario, and the findings are subsequently validated through an experimental transmission over a 17×65-km SSMF link.

3.5.2 Numerical Investigation

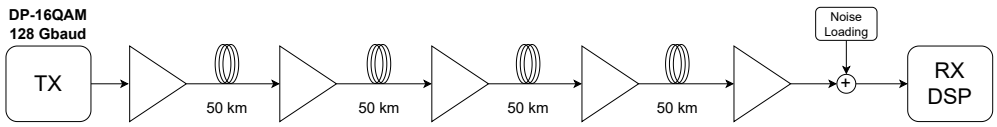

Fig. 3.15 Numerical setup used in the simulation investigation.

The performance penalty associated with using HD symbols for LLS-based LPM is first investigated through numerical simulations. The setup, shown in Fig. 3.15, consists of a WDM signal with $N_{\text{ch}} = 11$ DP-16QAM channels, spaced by 150 GHz, modulated at $R_s = 128$ Gbaud, and shaped by an SRRC filter with roll-off 0.1. The per-channel power is set to $P_{\text{ch}} = 5\,\text{dBm}$, with the central channel selected as the COI. The optical link is composed of 4×50-km identical SMF spans, with attenuation $\alpha_{\text{dB}} = 0.2\,\text{dB/km}$, dispersion coefficient $\beta_2 = -21.28\,\text{ps}^2/\text{km}$, and nonlinear coefficient $\gamma = 1.3\,1/\text{W/km}$. Each span is followed by a noiseless EDFA, fully compensating for the span loss. Fiber propagation is modeled with the SSFM. Before reception, noise loading is applied to the propagated signal. To cover a wide BER range, the OSNR is varied between 10 dB and 30 dB in steps of 1 dB. At the receiver, the signal undergoes CD compensation, adaptive equalization, CPE, and decoding. The CPR output is extracted and used for LPM, employing 2^{20} input samples and a spatial

step of $\Delta z = 1\,\text{km}$. Examples of power profiles estimated using HD sequences are shown in Fig. 3.16. When no errors are present in the HD sequence, the resulting PPE is consistent with the theoretical curve. However, as the OSNR decreases and the BER increases, an estimation offset emerges, degrading the PPE accuracy. This offset is quantified in Fig. 3.17

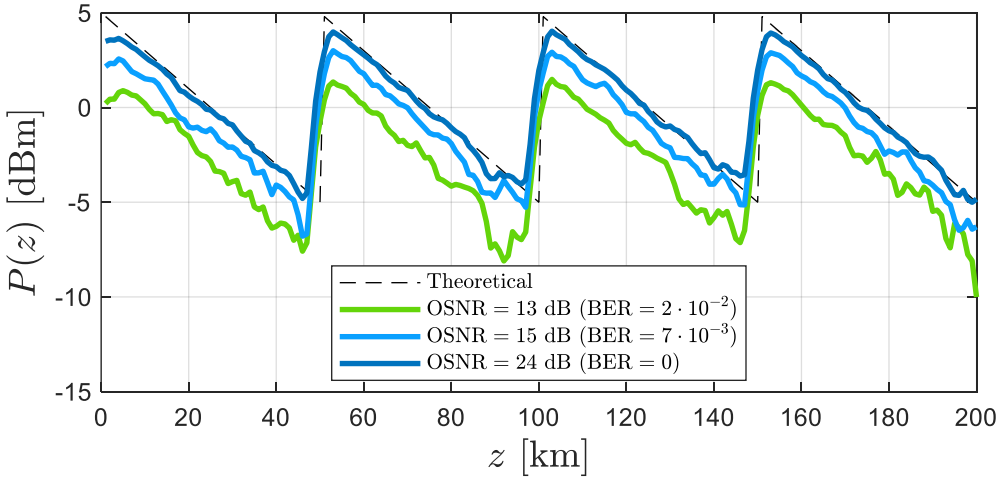

Fig. 3.16 Power profiles computed starting from HD sequences for varying OSNR (and BER) values.

for all tested BER values. It is defined as the difference in estimated power at the beginning of the third span ($z = 100\,\text{km}$) between the PPE obtained with an error-free sequence and that obtained with the HD sequence (referred to as HD-PPE). A simple linear relation between the offset and BER has been identified through fitting, expressed as a scaling factor

$$\psi\,[\text{dB}] = k \cdot \text{BER} \tag{3.12}$$

with $k \simeq 100$ for the considered setup and BER in linear units. This formula can be applied to correct HD-PPEs and improve the accuracy of NLI estimation.

3.5.3 Experimental Validation

The experimental validation is carried out using the same setup described in Sec. 3.4.2. In this case, the COI corresponds to the central WDM channel, which is the only channel analyzed. Equivalent results are expected for the other WDM channels. Figure 3.18 reports the power profiles obtained with LPM using both error-free (ideal) sequences and hard-decision (HD) sequences for the reconstruction of the reference signals. The complete profiles are shown in the upper plot, while a zoomed view is provided in the lower plot. This

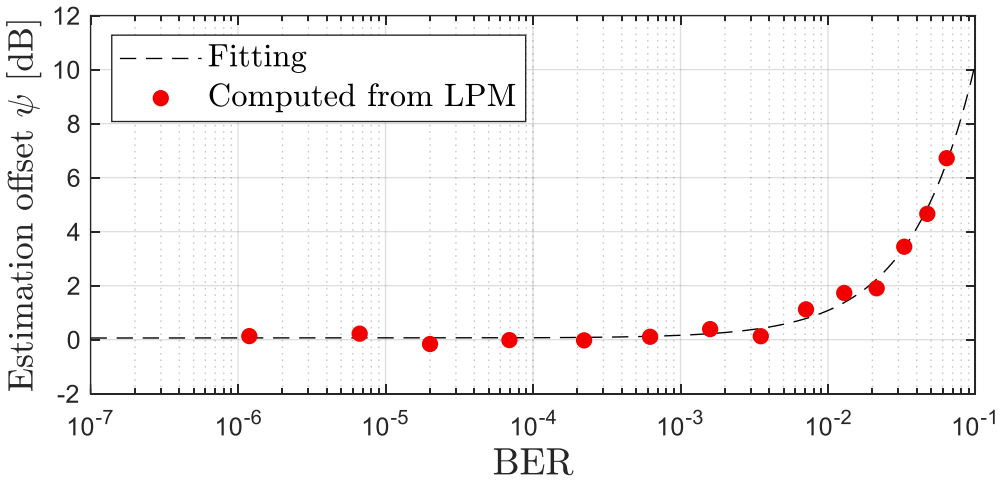

Fig. 3.17 Estimation offset for varying values of OSNR and BER.

representation facilitates the visualization of the impact of using HD sequences, highlighting the corresponding power offset discussed earlier.

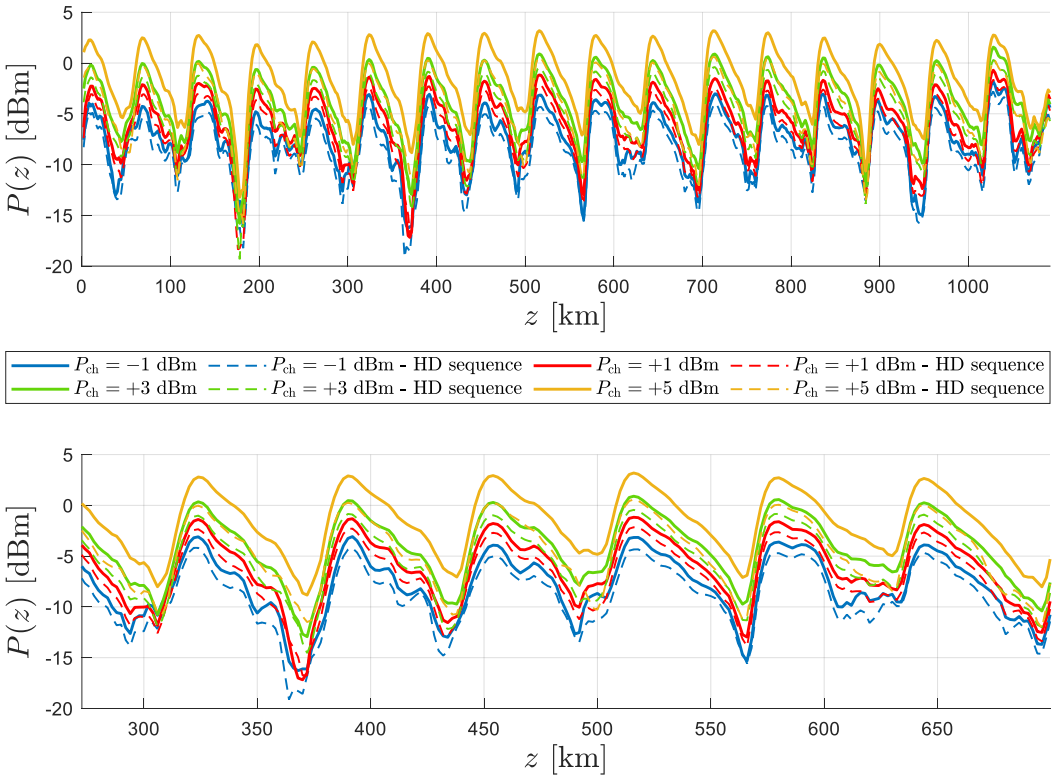

Fig. 3.18 Experimental power profiles computed starting from both error-free and HD sequences for different per-channel power levels. Full profiles (top) and zoom (bottom).

The NLI estimation is carried out according to (3.6). To evaluate the impact of HD, $\mathrm{SNR}_{\mathrm{NL}}$ is estimated under three conditions: (i) using PPEs computed with error-free sequences, (ii) using HD-PPEs without BER-based offset correction, and (iii) using HD-PPEs with offset correction. As a benchmark, the theoretical $\mathrm{SNR}_{\mathrm{NL}}$ is computed with the CFM [145]. The results, reported in Fig. 3.19, show that the error-free case achieves relatively accurate performance, with a mean absolute error of 0.5 dB with respect to CFM predictions. In contrast, using HD sequences at high BER (a reference range of BER values is shown in the inset of Fig. 3.13) significantly degrades the estimation, increasing the mean absolute error to 3.5 dB. Applying BER-based offset correction before computing (3.6) significantly improves the results, reducing the mean absolute error to 0.8 dB. The residual error is attributed to the fact that only the offset is corrected, while the PPEs remain affected by noise present in the reference sequence.

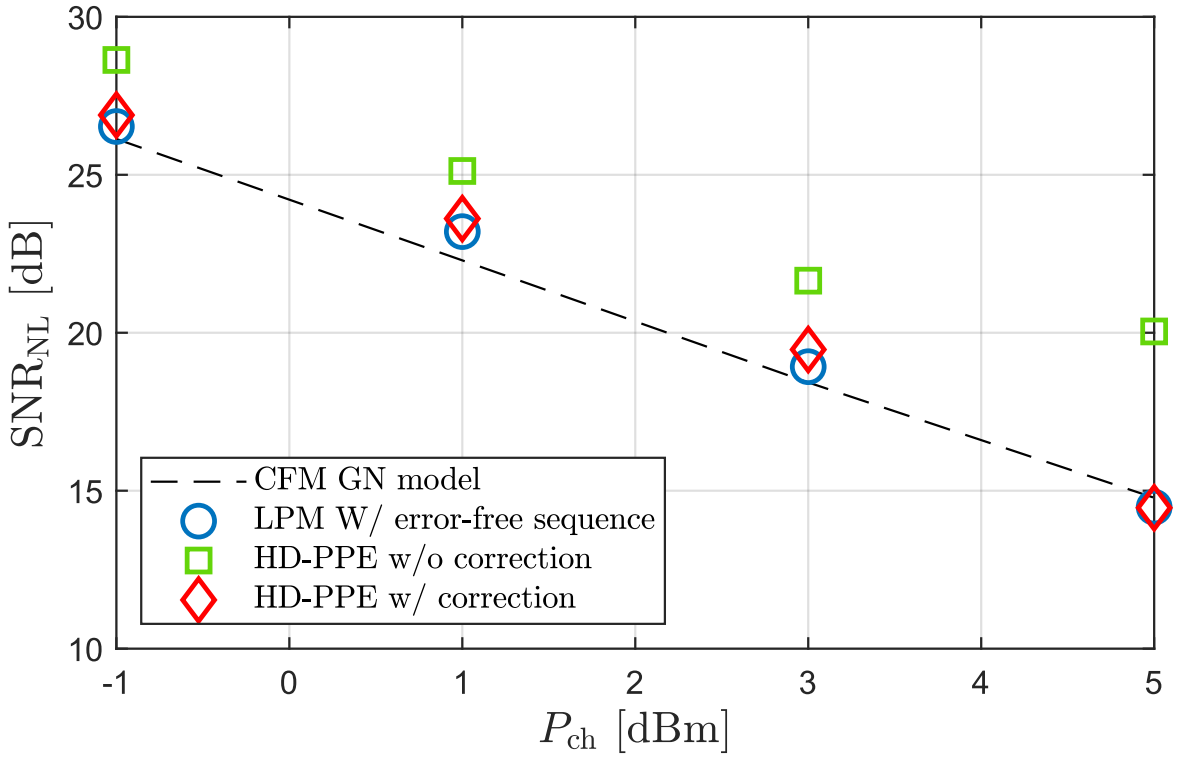

Fig. 3.19 Nonlinear SNR computed with CFM, PPE with error-free sequence, HD-PPE with and without offset correction for each tested power value.

3.6 Conclusions

In this chapter, a novel method for estimating the power of Kerr-induced NLI during coherent optical transmissions has been introduced. The method is fully embedded within the LLS-based LPM algorithm and relies exclusively on data already available at the receiver's DSP. Beyond NLI estimation, the approach also provides information on the power evolution of WDM channels, offering valuable input for higher-layer network optimization. The proposed technique was validated through extensive numerical simulations and two experimental scenarios with transmission distances of 300 km and 1100 km. Across all tested conditions, it provided accurate NLI estimates over a wide range of launch powers, including both optimal operating points and regimes where LPM typically encounters difficulties. Its accuracy was benchmarked against predictions of analytical NLI models as well as direct experimental measurements, consistently confirming the effectiveness of the approach. Furthermore, the method proved effective in predicting the optimal launch power, a key parameter for system and network optimization. Two main limitations were identified. First, the algorithm inherently estimates only the SCI contribution to NLI. To account for the total NLI, simple analytical correction factors were derived, requiring only limited knowledge of system parameters. Second, a relatively large dataset is necessary for reliable operation, particularly at low launch powers. However, in practical networks, both NLI power and launch power are expected to remain relatively stable over time, making it feasible to run the algorithm offline by periodically extracting telemetry from the receiver DSP. Future developments should focus on extending the evaluation of the method's accuracy to a broader set of transmission scenarios and investigating its potential for network optimization in UWB systems, where launch-power optimization remains an active area of research [174–176]. In addition, practical implementation aspects have been considered. Specifically, the penalties introduced when reconstructing the reference signal for LPM using HD symbols, instead of error-free sequences (e.g., pilots or post-FEC data), have been analyzed. Numerical simulations showed that the power offset in HD-based power profile estimates can be related to the pre-FEC BER through a simple scaling law. Experimental validation over a 17×65-km SSMF link confirmed that, once this BER-based correction is applied, the additional penalty in NLI estimation accuracy remains limited to approximately 0.3 dB. Overall, the presented work demonstrates the feasibility of LPM-based NLI estimation as a practical and accurate solution for live network monitoring, while also highlighting the main limitations, corrective strategies, and implementation trade-offs.

Chapter 4

DSP-based Fiber Sensing Applications in Metropolitan Networks

This chapter analyzes various aspects of DSP-based fiber sensing. Specifically, Sec. 4.1 presents an experimental analysis of the intrinsic accuracy of state of polarization estimation from the DSP of commercial coherent transceivers, focusing on angular uncertainty on the Poincaré sphere as a function of received OSNR for sensing applications. The section also demonstrates how applying a moving average significantly improves estimation accuracy. Then, Sec. 4.2 presents an experimental comparison between SOP- and phase-based signal extraction for vibration sensing, carried out under identical system conditions over a deployed 32-km unamplified metropolitan fiber link using coherent receivers. The methodologies, simulations, and experimental results discussed in this chapter have also been reported in the following publications:

- S. Pellegrini, L. Minelli, L. Andrenacci, G. Rizzelli, D. Pilori, G. Bosco, L. Della Chiesa, C. Crognale, S. Piciaccia and R. Gaudino, "Overview on the state of polarization sensing: application scenarios and anomaly detection algorithms," in Journal of Optical Communications and Networking, vol. 17, no. 2, pp. A196-A209, February 2025, doi: 10.1364/JOCN.537881;
- S. Pellegrini, L. Andrenacci, L. Minelli, D. Pilori, G. Bosco, L. Della Chiesa and R. Gaudino, "Estimation Accuracy of Polarization State from Coherent Receivers for Sensing Applications," 2023 IEEE Photonics Conference (IPC), Orlando, FL, USA, 2023, pp. 1-2, doi: 10.1109/IPC57732.2023.10360574;

- L. Andrenacci, D. Pilori, S. Pellegrini, L. Minelli, G. Bosco, C. Crognale, S. Piciaccia and R. Gaudino, "Comparison between Phase and Polarization Sensing using Coherent Transceivers over Deployed Metro Fibers," 2024 Optical Fiber Communications Conference and Exhibition (OFC), San Diego, CA, USA, 2024, pp. 1-3;

4.1 Estimation Accuracy of DSP-based State of Polarization Monitoring

This section presents an experimental investigation of the physical-layer factors affecting the accuracy of SOP estimation when using standard coherent transceivers. The analysis is based on numerical simulations and measurements obtained from a commercial transceiver that outputs the received light's SOP via its internal DSP, which represents a typical scenario in SOP-based sensing.

4.1.1 DSP-based State of Polarization Estimation

SOP-based sensing represents an interesting alternative to traditional distributed sensing techniques, since it can be implemented using the digital infrastructure already present in coherent optical communication systems. Specifically, it operates entirely within the receiver's DSP chain, allowing polarization changes to be monitored without the need for specific and possibly expensive external hardware. This approach not only reduces implementation costs but also simplifies system design and deployment. By extracting the state of polarization information directly from the adaptive equalizer coefficients in the coherent receiver, the system continuously tracks polarization dynamics with high sensitivity. As a result, SOP-based sensing is particularly attractive for large-scale and cost-sensitive applications, where conventional distributed sensing methods like DAS may be impractical due to their hardware requirements and higher complexity.

Let us consider a 2×2 complex-valued adaptive equalizer implemented in a coherent receiver with N_{tap} taps. To simplify the following equations, the notation from [93] will be employed. The relationship between the input signal $\mathbf{s}_{\text{in}}[n] = [\mathbf{x}_{\text{in}}[n], \mathbf{y}_{\text{in}}[n]]^T$ and the output signal $\mathbf{s}_{\text{out}}[n] = [\mathbf{x}_{\text{out}}[n], \mathbf{y}_{\text{out}}[n]]^T$ is described by $\mathbf{s}_{\text{out}}[n] = \mathbf{W}[n] \cdot \mathbf{s}_{\text{in}}[n]$, where the convolution operation is implemented by means of matrix multiplications [6]. In this context, n is the discrete-time index and $\mathbf{W}[n]$ is the equalization matrix expressed as in:

$$\mathbf{W}[n] = \begin{bmatrix} \mathbf{w}_{11}^{(m)}[n] & \mathbf{w}_{12}^{(m)}[n] \\ \mathbf{w}_{21}^{(m)}[n] & \mathbf{w}_{22}^{(m)}[n] \end{bmatrix} \tag{4.1}$$

Here, m denotes the tap index, and each element $\mathbf{w}_{ij}^{(m)}[n]$ corresponds to an $N_{\text{tap}} \times 1$ vector of filter coefficients, with $i, j = 1, 2$. The DC component of these vectors, denoted by $\bar{w}_{ij} = \sum_{m=1}^{N_{\text{tap}}} w_{ij}^{(m)}[n]$, captures the steady-state behavior of the equalizer.

The DC component of each column in $\mathbf{W}[n]$ represents a Jones vector, which can be used to compute the associated Stokes parameters. For example, using the first column of the matrix in (4.1), the Stokes parameters are given by:

$$\begin{aligned} S_0[n] &= |\bar{w}_{11}[n]|^2 + |\bar{w}_{21}[n]|^2 \\ S_1[n] &= |\bar{w}_{11}[n]|^2 - |\bar{w}_{21}[n]|^2 \\ S_2[n] &= 2 \cdot \text{Re}(\bar{w}_{11}[n] \cdot \bar{w}_{21}^*[n]) \\ S_3[n] &= -2 \cdot \text{Im}(\bar{w}_{11}[n] \cdot \bar{w}_{21}^*[n]),. \end{aligned} \tag{4.2}$$

In these expressions, $(\cdot)^*$, $\text{Re}(\cdot)$, and $\text{Im}(\cdot)$ denote the complex conjugate, real part, and imaginary part, respectively. For compact representation and practical use in polarization analysis, we define the normalized Stokes vector as $\vec{S}[n] = [S_1[n], S_2[n], S_3[n]]$, where each component is normalized by $S_0[n]$. This allows to map the signal's polarization state onto the unit Poincaré sphere. The whole process is illustrated in Fig. 4.1.

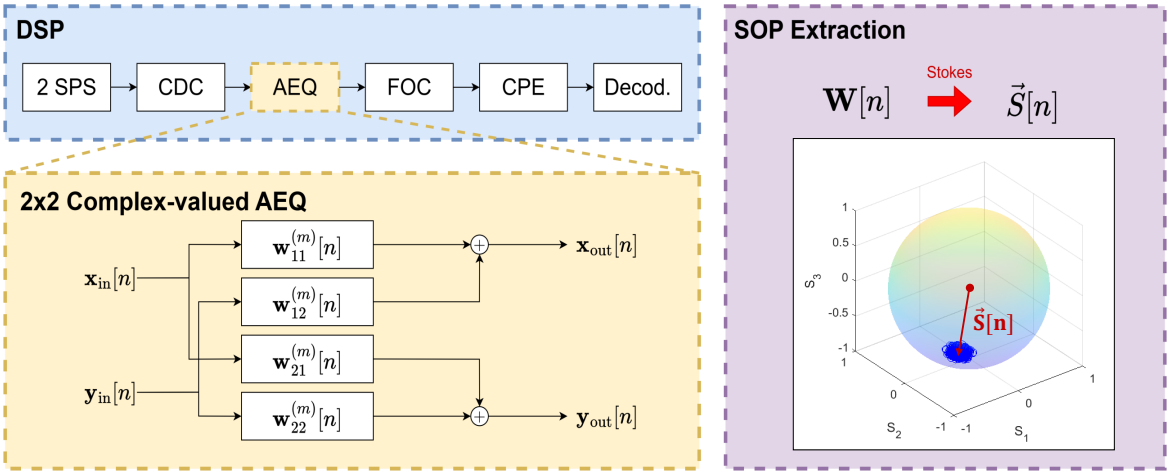

Fig. 4.1 Schematic of SOP extraction from 2×2 complex-valued adaptive equalizer within the DSP of a coherent receiver.

4.1.2 Numerical and Experimental Setup

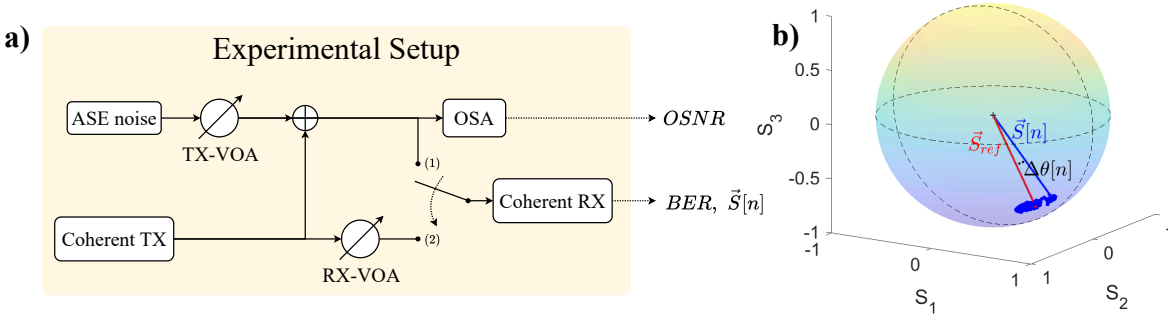

Fig. 4.2 (a) Experimental setup. When connection (1) is selected, the coherent RX considers ASE noise injected in the system. When instead connection (2) is selected, ASE noise is excluded. (b) Poincaré sphere showing the $\vec{S}_{\text{ref}}$ (in red) and $\vec{S}[n]$ (in blue) vectors and the angular deviation $\Delta\theta[n]$.

A numerical analysis was conducted to evaluate the intrinsic accuracy of SOP extraction performed leveraging the DSP stage of an optical transceiver. The analysis focused on quantifying the standard deviation of the estimated SOP under the assumption of constant fiber birefringence and operation at a fixed OSNR. A DP-QPSK signal was simulated at a symbol rate of 34.7 Gbaud, shaped with a square-root raised-cosine filter with roll-off factor $\rho = 0.2$, in a back-to-back configuration where ASE noise was the only impairment. Receiver OSNR values ranging from 6 dB to 12 dB were considered, assuming a noise bandwidth equal to the symbol rate. By introducing ASE noise loading, the scenario emulates long-haul, optically amplified transmission systems operating with sufficiently high received optical power. SOP estimation was carried out using a standard coherent receiver DSP chain sampled at 2 samples per symbol. The estimation relied on the tap coefficients obtained from an LMS-based 2×2 adaptive equalizer with $N_{\text{tap}} = 16$ taps, following the procedure introduced in Sec. 4.1.1. In the numerical simulations, equalizer tap coefficients (and the corresponding SOP sample) were extracted every 200 ns while processing a total of $20 \cdot 10^6$ samples, resulting in a SOP sampling frequency of $f_s = 5$ Msample/s. This process was repeated across various received OSNR levels.

An equivalent transmission scenario was subsequently investigated experimentally using a commercial coherent transceiver in a back-to-back configuration with fixed fiber birefringence. ASE noise loading was employed to emulate different OSNR conditions, yielding BER values ranging from 10^{-2} down to the error-free regime. The corresponding OSNR values spanned from 6 dB to 18 dB and were measured using the same noise bandwidth as that adopted in the numerical analysis.The transceiver extracts SOP samples at around 20 sample/s. The experimental setup is shown in Fig. 4.2(a).

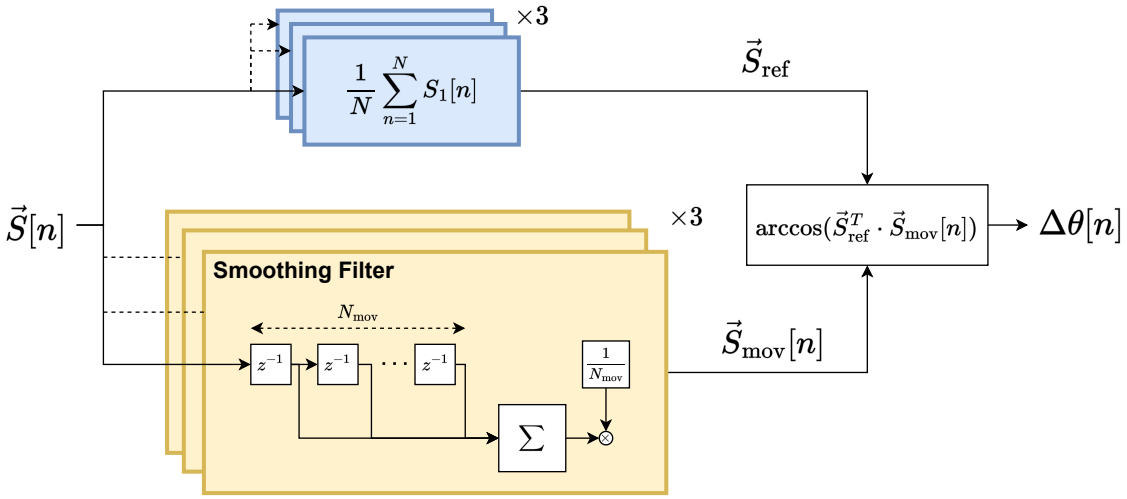

Fig. 4.3 Post-processing scheme employed to compute the angular deviation $\Delta\theta[n]$. A long-term average of N samples over the whole $\vec{S}[n]$ time series is employed to obtain $\vec{S}_{\text{ref}}$ vector. A smoothing filter is applied over each single Stokes parameter time evolution to obtain instead $\vec{S}_{\text{mov}}[n]$. The last block shows how the angular deviation $\Delta\theta$ is computed.

The accuracy of the SOP estimation was assessed by calculating the angular deviation of each Stokes vector from a reference vector $\vec{S}_{\text{ref}}$. As illustrated in Fig. 4.2(b), the blue points represent the time evolution of the vector $\vec{S}[n]$, extracted either from the commercial coherent receiver or from the equalizer in the numerical simulations. The red vector, $\vec{S}_{\text{ref}}$, serves as the reference for computing the angular deviation, denoted as $\Delta\theta[n]$. The associated post-processing procedure is detailed in Fig. 4.3. In this process, each Stokes parameter, i.e., $S_1[n]$, $S_2[n]$, and $S_3[n]$, is passed through a moving average filter, referred to as the smoothing filter in Fig. 4.3, with a window length of N_{win}. The case with $N_{\text{win}} = 1$ corresponds to the unfiltered case. The output of this filtering stage is a smoothed representation of the Stokes vector sequence, denoted as $\vec{S}_{\text{mov}}[n]$. In parallel, a long-term average of the entire $\vec{S}[n]$ acquisition is computed by averaging each Stokes parameter over N samples, where N typically ranges in a few hundreds. This averaging yields the reference vector $\vec{S}_{\text{ref}}$, depicted in red in Fig. 4.2(b), which serves as a ground-truth estimate positioned at the center of the SOP noise distribution on the Poincaré sphere. It is worth noting that, in this particular experiment, fiber birefringence was intentionally kept constant over time. For this reason, the observed SOP variations originate exclusively from estimation noise within the coherent receiver.

The angular deviation is then computed as $\Delta\theta[n] = \arccos(\vec{S}_{\text{ref}}^{T} \cdot \vec{S}_{\text{mov}}[n])$, where $(\cdot)^T$ denotes the transpose operation. This metric provides a quantitative measure of the SOP noise

dispersion on the Poincaré sphere surface and offers insight into the underlying estimation noise conditions [177].

4.1.3 Analysis of SOP Angular Deviation

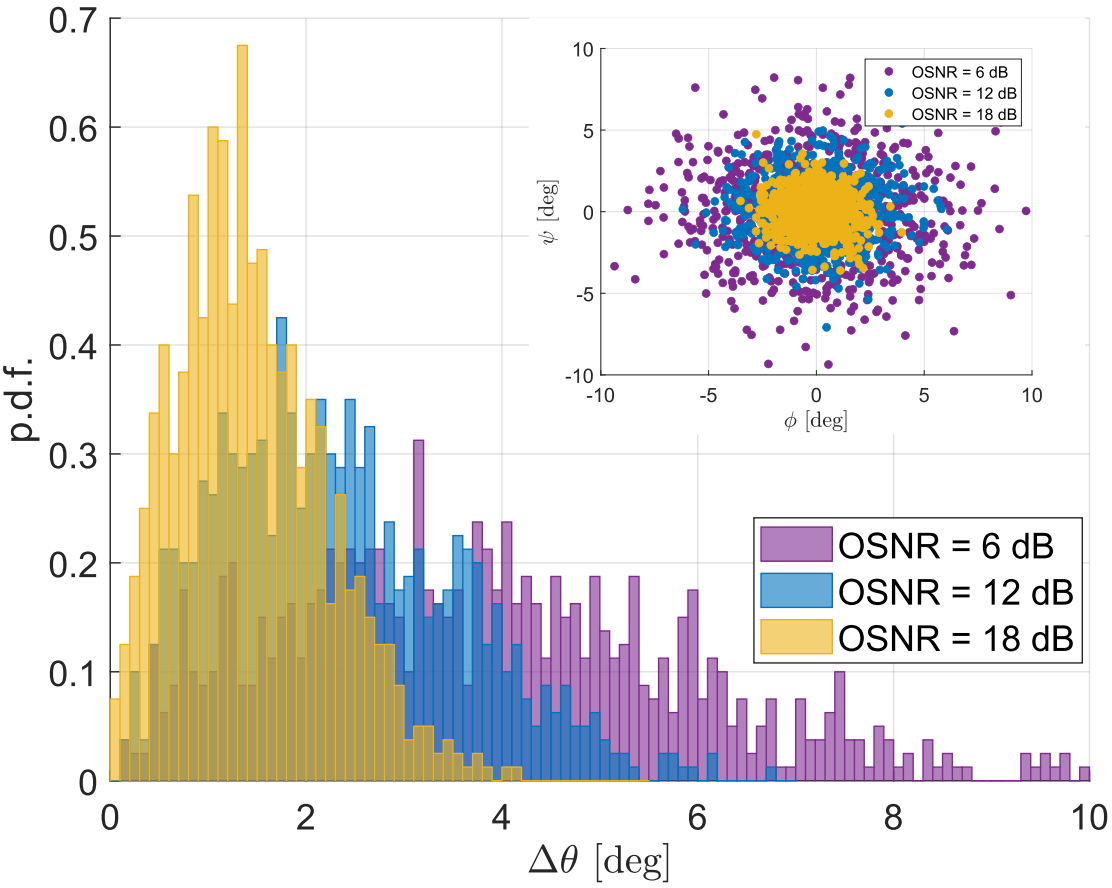

Fig. 4.4 $\Delta\theta[n]$ histograms at three different OSNR levels. The inset reports the cloud distribution of the SOP points over the Poincaré sphere surface, in angular coordinates.

In this configuration, the coherent receiver is connected through path (1) in the experimental setup illustrated in Fig. 4.2(a), enabling the transmitter-side VOA to regulate the level of injected ASE noise. The OSNR values, spanning from 6 dB to 18 dB, were measured using an OSA. Simultaneously, the corresponding SOP samples were acquired from a commercial coherent transceiver in the form of Stokes vector time sequences. Figure 4.4 presents the probability density functions (PDFs) of $\Delta\theta[n]$ for three representative OSNR levels, namely 6, 12, and 18 dB, using a DP-QPSK modulation format and a smoothing window length of $N_{\text{win}} = 1$. The inset provides a visualization of the SOP cloud dispersion mapped in angular

coordinates, projected onto two orthogonal rotation axes. As anticipated, the histograms demonstrate that higher OSNR values lead to reduced statistical spread in the $\Delta\theta[n]$ distribution. This implies that, in practical sensing scenarios, mechanical perturbations resulting in significant SOP deviations would be more easily distinguishable under low-noise conditions.

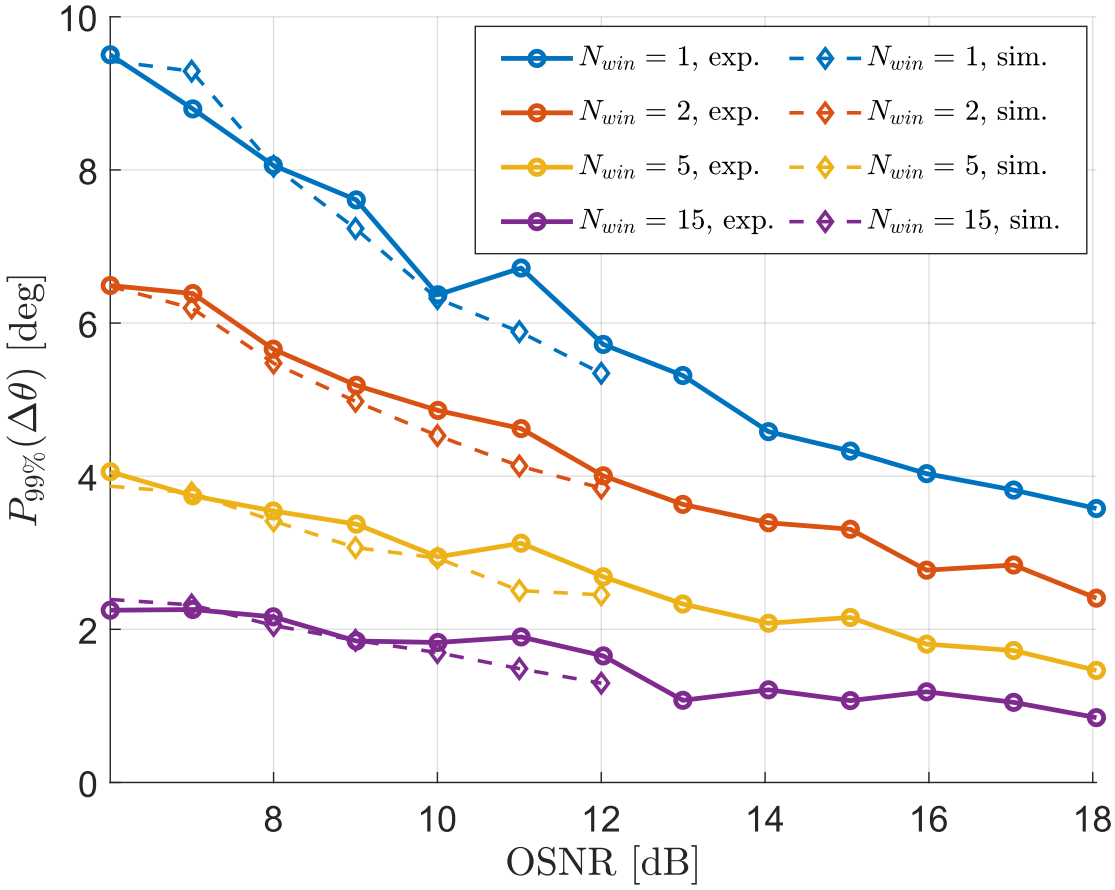

Fig. 4.5 $P_{99\%}(\Delta\theta)$ vs. OSNRs for different moving average windows N_{win} (experiments and numerical simulation).

To provide a quantitative metric for this observation, the 99-th percentile of the angular deviation, denoted as $P_{99\%}(\Delta\theta)$, is introduced. This value represents the angular threshold exceeded by only 1% of the $\Delta\theta[n]$ samples. Given the strictly positive nature and asymmetry of the angular deviation distributions, this percentile-based measure offers a more appropriate characterization of the spread than conventional metrics such as the mean or standard deviation. Figure 4.5 reports the evolution of $P_{99\%}(\Delta\theta)$ as a function of OSNR for various values of N_{win}. Experimental results are indicated by circle-marked lines, while the dashed lines with diamond markers correspond to time-domain simulations. The strong agreement between the two datasets highlights that the simulation model, despite its idealized

assumptions, accurately reflects the experimental behavior. This suggests that the observed trends are largely independent of specific implementation details within the receiver DSP. The simulation data is limited to an OSNR of 12 dB, which represents the upper bound at which reliable BER values (approximately 10^{-4}) could be obtained without incurring excessive computational costs or simulation time. The results indicate that increasing N_{win} leads to a marked reduction in $P_{99\%}(\Delta\theta)$. For example, with $N_{\text{win}} = 15$, angular deviations fall below 2° across all measured OSNR levels. This effect is further illustrated by examining the PDFs shown in Fig. 4.6, corresponding to the case of OSNR $= 12\,$dB. The moving average used to compute $\vec{S}_{\text{mov}}[n]$ can be implemented with minimal additional DSP overhead, making it an effective strategy to suppress SOP noise. The main trade-off associated with this approach is the reduction in effective SOP sampling rate as N_{win} increases. However, this limitation is not critical, given that the mechanical disturbances targeted in SOP-based sensing typically exhibit low-frequency components, ranging from a few Hz to several tens of Hz [16, 178]. As a result, the system requirements for high-speed signal processing and data storage can be relaxed.

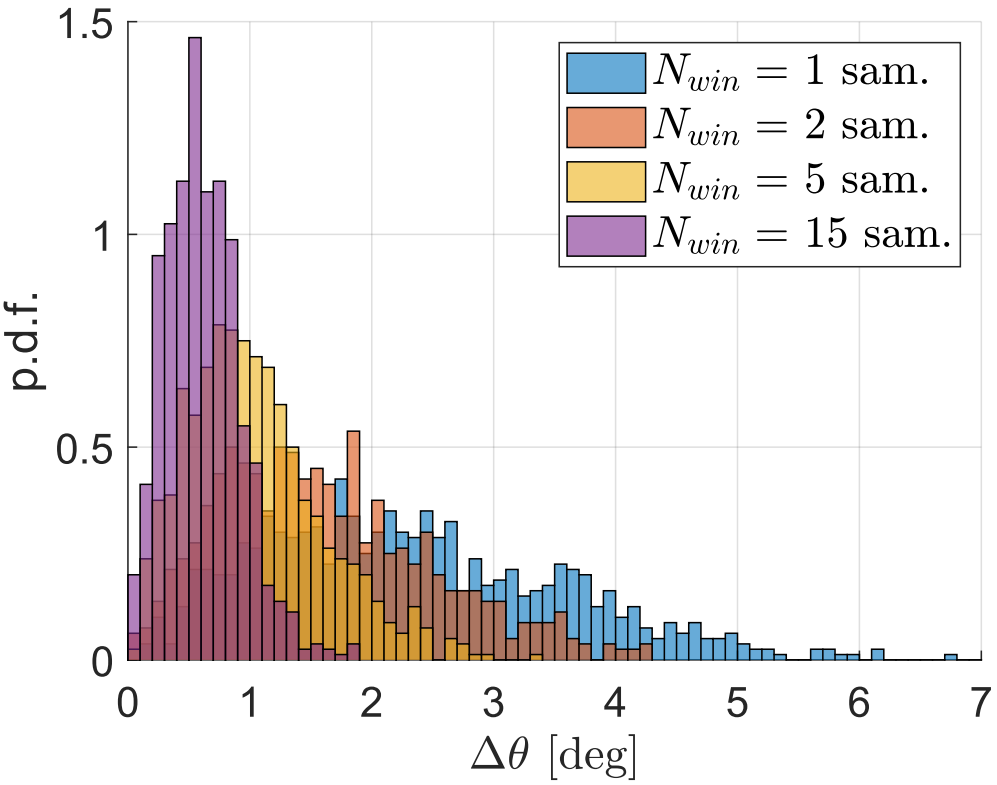

Fig. 4.6 Probability distribution of angular deviation $\Delta\theta[n]$ for OSNR $= 12\,$dB.

The findings indicate that SOP-based sensing enables reliable detection of external perturbations, such as mechanical vibrations, when these induce angular deviations on the Poincaré sphere on the order of several degrees. To improve sensitivity and reduce estimation noise, a post-processing strategy based on a moving average across N_{win} samples of the Stokes vector $\vec{S}[n]$ was introduced. This method effectively reduced angular noise, bringing the 99th percentile deviation $P_{99\%}(\Delta\theta)$ below 2 degrees across all tested OSNR levels. Experimental results obtained using a commercial coherent transceiver were consistent with simulation outputs, confirming that the observed estimation performance represents an intrinsic limit of SOP accuracy, largely independent of specific DSP implementation details.

4.2 Comparison between Length-integrated Sensing Techniques using Coherent Transceivers

This section presents an experimental evaluation of the sensing capabilities of SOP-based fiber sensing in a real-world metropolitan environment. The objective is to assess its practical effectiveness for detecting external perturbations, such as vibrations, that may impact the optical link. In addition, the performance of SOP-based sensing is compared with an alternative DSP-based technique, i.e., optical phase-based sensing, which has also gained attention for sensing applications. By conducting a comparative analysis under identical transmission conditions, the strengths and limitations of each approach are highlighted, providing insights into their suitability for various fiber sensing scenarios.

4.2.1 DSP-based Optical Phase Estimation

As previously discussed in Sec. 1.5.1, SOP-based sensing represents just one possible approach among various length-integrated fiber sensing techniques. Indeed, the state of polarization is not the only optical signal property influenced by external perturbations. In recent years, the optical phase of light propagating through fiber has gained increasing attention as a valuable parameter for sensing applications. External perturbations, such as mechanical vibrations, acoustic disturbances, or seismic events, induce localized variations in the optical path length of the fiber, which manifest as phase shifts in the transmitted optical signal. This fundamental relationship can be expressed as [179]

$$\phi_{\text{vib}} = 0.78\frac{2\pi n}{\lambda}\Delta z \tag{4.3}$$

where λ denotes the wavelength of the optical signal, n the refractive index and Δz the change in optical path. The factor 0.78, instead, accounts for the strain-optic effect.

Initial approaches to phase-based sensing were based on interferometric techniques [95], which achieved high sensitivity by measuring differential phase shifts over long optical paths. However, these systems require dedicated channels or high transmit power, making them unsuitable for large-scale or field-deployable applications, particularly in the context of existing telecommunications networks.

The DSP in modern transceivers has opened new possibilities for phase sensing. In such systems, the phase of the received optical signal can be estimated directly in the digital domain, using data already available from standard receiver operations. Hence, the optical phase of the signal can be reconstructed in a similar way to that employed for SOP estimation, by exploiting the DSP blocks responsible for tracking the phase during signal processing. These include frequency offset compensation, adaptive equalization, and carrier phase recovery stages. Using the same notation as in Sec. 4.1.1, the FOC stage performs a phase rotation expressed as

$$\mathbf{s}_{\text{out}}[n] = \exp\left(-j2\pi\Delta\Omega n\right)\mathbf{s}_{\text{in}}[n] \tag{4.4}$$

where $\Delta\Omega = \Delta f T$ denotes the digital frequency offset, Δf the laser frequency offset and T the sampling rate. Afterwards, the signal undergoes CDC and enters the adaptive equalizer, whose expression is again

$$\mathbf{s}_{\text{out}}[n] = \mathbf{W}[n] \cdot \mathbf{s}_{\text{in}}[n] \tag{4.5}$$

where $\mathbf{W}[n]$ is the same as in (4.1). Finally, carrier phase estimation is performed and phase is rotated as

$$\mathbf{s}_{\text{out}}[n] = \exp\left(-j\Delta\Psi[n]\right)\mathbf{s}_{\text{in}}[n] \tag{4.6}$$

where $\Delta\Psi[n] = [\Delta\psi_1[n],\ \Delta\psi_2[n]]^T$ is the vector of CPE phase rotations for each polarization. Overall, the total optical phase tracked by these DSP stages can be expressed as [93]

$$\hat{\theta}[n] = -2\pi\Delta\Omega n + \arg\left\{\sum_{ij} \bar{w}_{ij}^{(n)} e^{-j\Delta\psi_i[n]}\right\}, \quad i,j = 1,2 \tag{4.7}$$

A visual representation of this process is reported in Fig. 4.7.

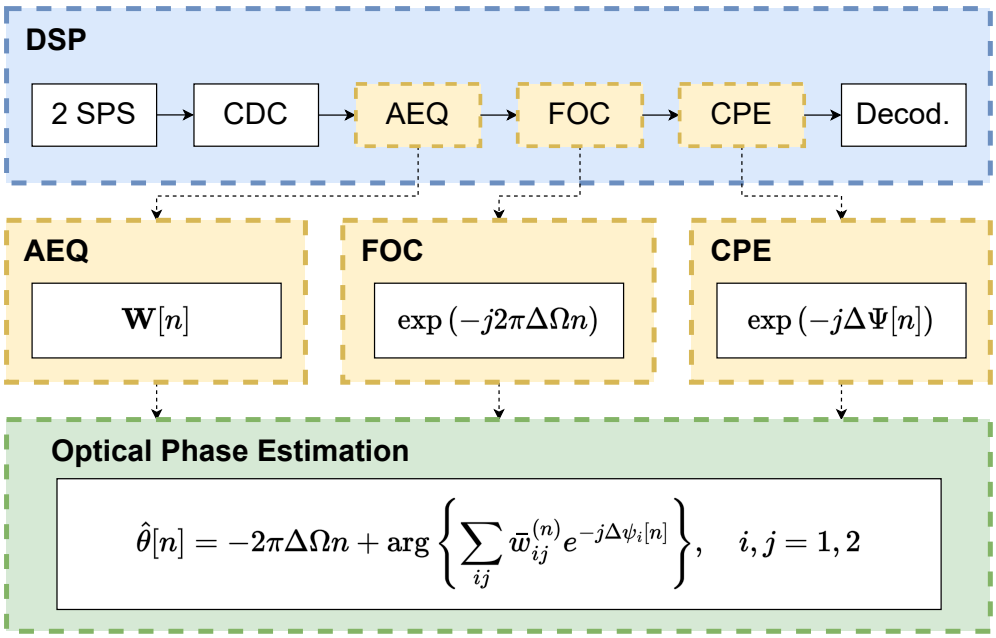

Fig. 4.7 Schematic of DSP-based optical phase extraction.

This development enables phase-based sensing to be implemented with minimal additional hardware, leveraging the infrastructure of deployed coherent transceivers. Nonetheless, a major challenge arises from the fact that the recovered phase is influenced not only by external perturbations but also by impairments such as laser phase noise. Segregating the contribution of environmental perturbations from intrinsic system effects is not easy and requires potentially expensive system modifications, such as the employment of low-phase-noise laser sources.

4.2.2 Experimental Setup

The experimental setup is depicted in Fig. 4.8. At the transmitter side, an ultra-low noise OE4040-VLN laser, centered at 1545.17 nm with a spectral linewidth < 7 Hz, was used to modulate a 32-Gbaud DP-16QAM signal shaped by a square-root raised-cosine filter with a roll-off factor of 0.2. The experiments were conducted over a 32-km underground fiber link located in the metropolitan area of Turin, as shown in the inset in Fig. 4.8. For comparison,

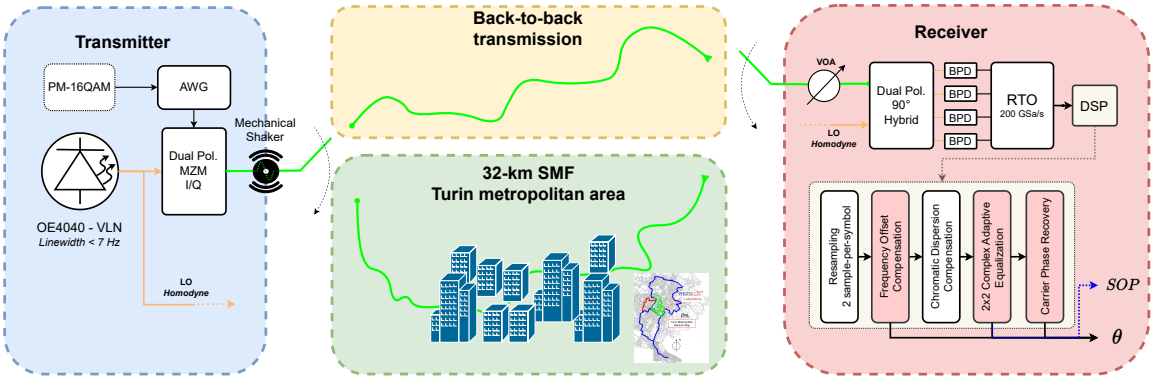

Fig. 4.8 Experimental setup for SOP- and phase-based sensing experiments. Both back-to-back and metropolitan network configurations are used.

measurements were also performed in a back-to-back configuration. Since the metropolitan link was unamplified, i.e., it did not include EDFAs, the BER and the accuracy of SOP and phase estimation were influenced exclusively by the internal noise of the coherent receiver. At the receiver, signal acquisition was performed using a real-time oscilloscope (RTO) operating at 200 Gsample/s, with data processed offline through a standard DSP chain used in coherent optical receivers. The RTO captured bursts of 200 ns duration every 1 ms, enabling long-term acquisitions spanning several tens of seconds, which is in line with the typical time constants of mechanical vibrations.

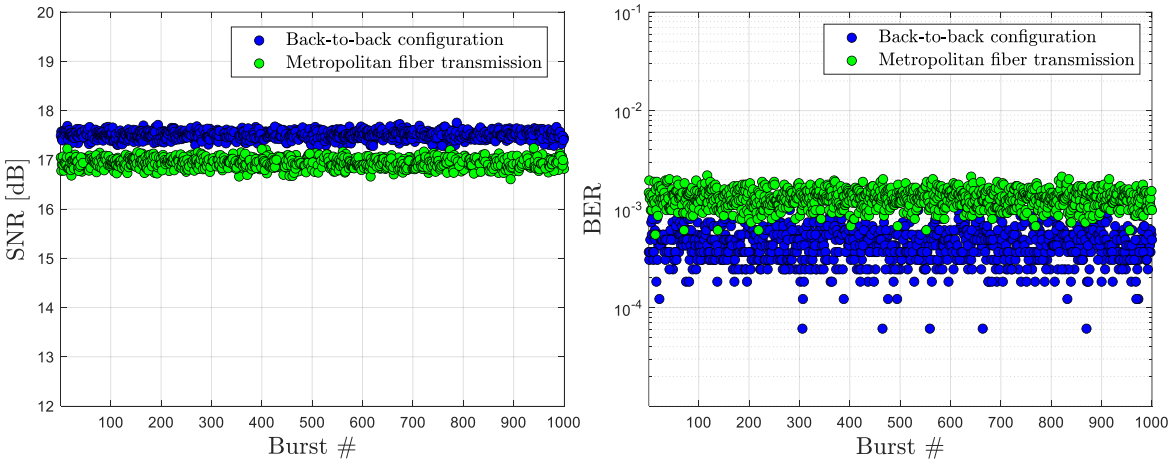

Fig. 4.9 SNR and corresponding BER for each processed burst, measured in both the back-to-back and the 32-km metropolitan fiber link transmission scenarios.

Each burst was processed through front-end correction functions, 2-sample-per-symbol resampling, FOC, CDC, data-aided adaptive equalization, and CPE. Equalization is performed

using a LMS-based 2×2 complex-valued equalizer with 16 taps. The DSP chain consistently converged within the burst duration, achieving a mean SNR exceeding 17 dB in both test configurations. The corresponding BER measured over 1000 bursts is shown in Fig. 4.9, together with the SNR. This post-processing methodology enables the extraction of both SOP and phase information from each burst at a sampling rate of $f_s = 1000$ samples/s following the procedures presented in the previous sections.

4.2.3 Comparative Analysis: SOP and Optical Phase

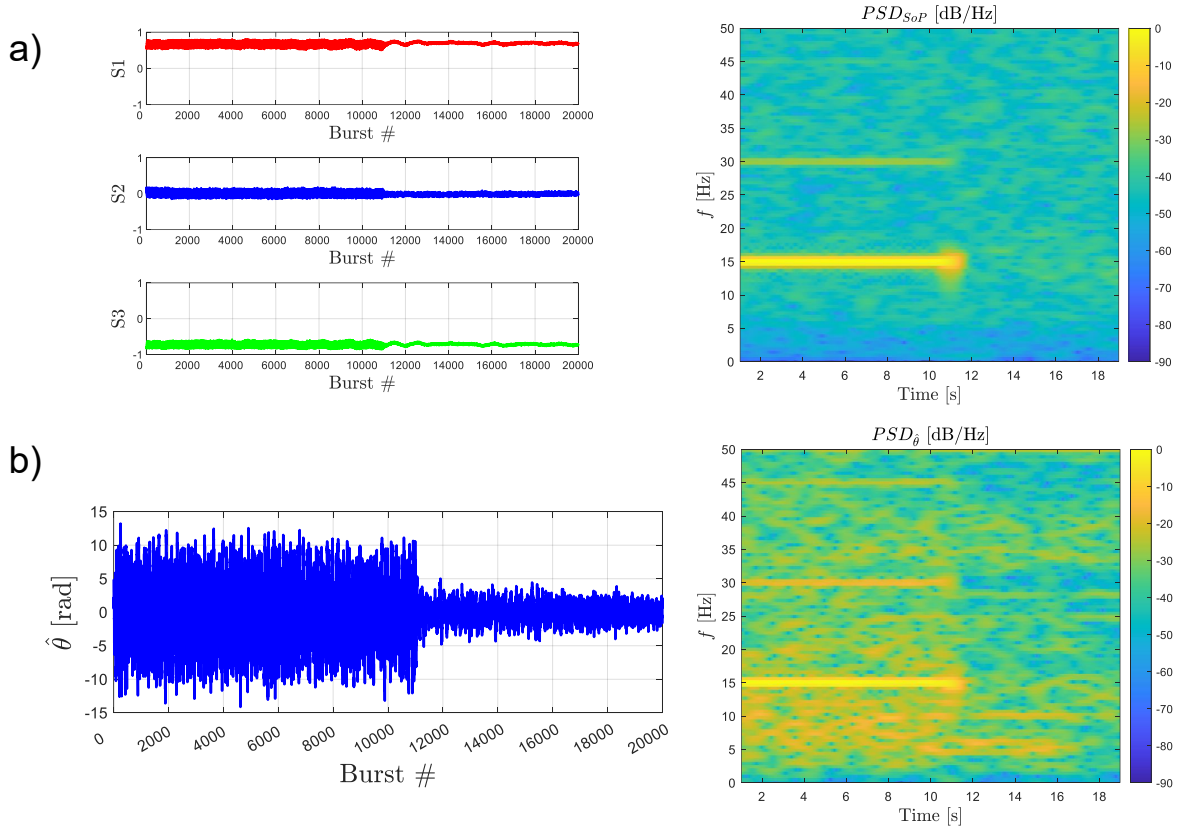

Fig. 4.10 Back-to-back results for a 10-second induced sinusoidal vibration of 15 Hz. a) Stokes parameters and corresponding spectrogram. b) Optical phase after DC component removal and corresponding spectrogram.

To assess the sensing capabilities of the extracted parameters, controlled mechanical vibrations were introduced along the fiber links using a shaker positioned immediately after the transmitter (see Fig. 4.8). The shaker was driven by a low-frequency signal generator, operating in the few-hertz range, to apply a tunable sinusoidal vibration to the fiber. The impact of mechanically induced vibrations on the fiber is analyzed using spectrograms

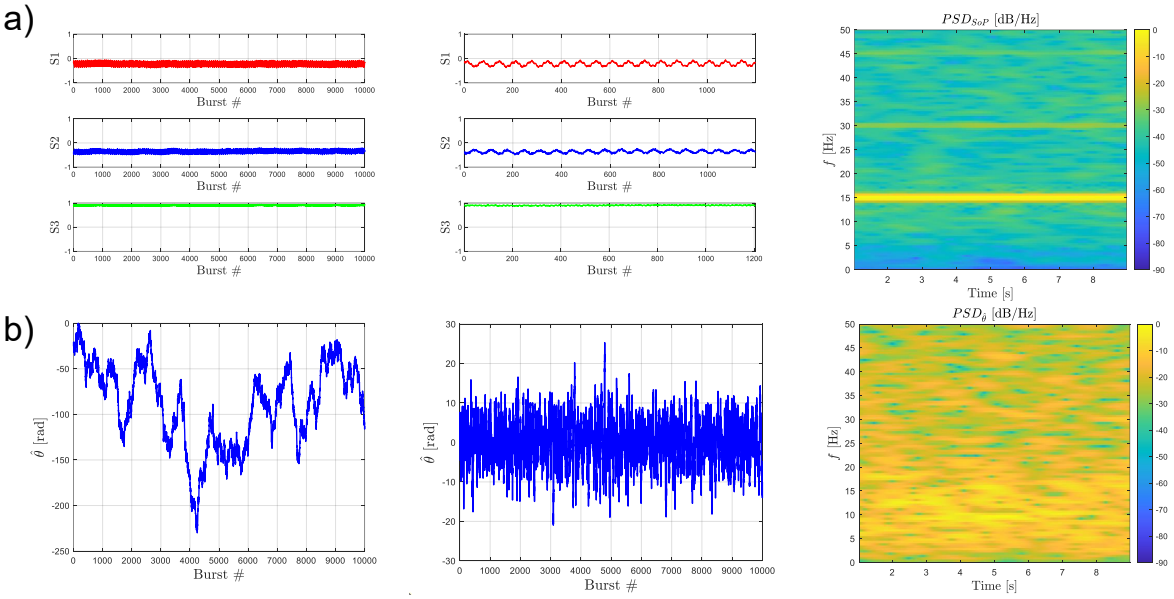

Fig. 4.11 Experimental results using both the SOP-based and phase-based sensing approaches over the 32-km metropolitan fiber link when a constant induced vibration of $f = 15\,\text{Hz}$ is applied to the fiber. a) The Stokes parameters, a zoom and the spectrogram are reported. b) The optical phase, before and after DC component removal, and the spectrogram are reported.

derived from both the optical phase and the SOP, following the same procedure. Initially, the DC component of each signal is removed by applying a high-pass filter, implemented through the subtraction of a moving average version of the original signal, with a sliding window of $T_{\text{win}} = 100\,\text{ms}$. Afterwards, the PSD is computed and smoothed using another moving average filter with the same time window. To enhance visualization, all spectra are normalized to emphasize the relative power contrast between regions affected by vibrations and the surrounding noise floor. For SOP-based analysis, the PSDs of the three individual Stokes parameters are first summed and then averaged, in accordance with the method adopted in [88].

The results obtained from a 20-second acquisition in the back-to-back configuration are presented in Fig. 4.10. During this measurement, the mechanical shaker was driven by a sinusoidal signal at a frequency $f_{\text{vib}} = 15\,\text{Hz}$, applied for the initial ~ 10 seconds of the acquisition period before being turned off. The induced vibration is clearly identifiable in the PSD of both the optical phase and the SOP signals, albeit with varying levels of sensitivity. Specifically, the spectral component at $f = 15\,\text{Hz}$ emerges as the dominant component during the time interval in which the shaker is active. For the optical phase, this component is approximately 20 dB above the noise floor, while for the SOP, it reaches a separation of 40 dB. It is also worth noting that harmonic components are visible in the spectrogram, and they

are most likely generated by nonlinear behavior of the shaker. These results indicate that the optical phase is characterized by a higher sensitivity to external perturbations, as reflected by a noisier PSD, an observation that holds even under the relatively stable conditions of a back-to-back setup, where environmental disturbances are minimal.

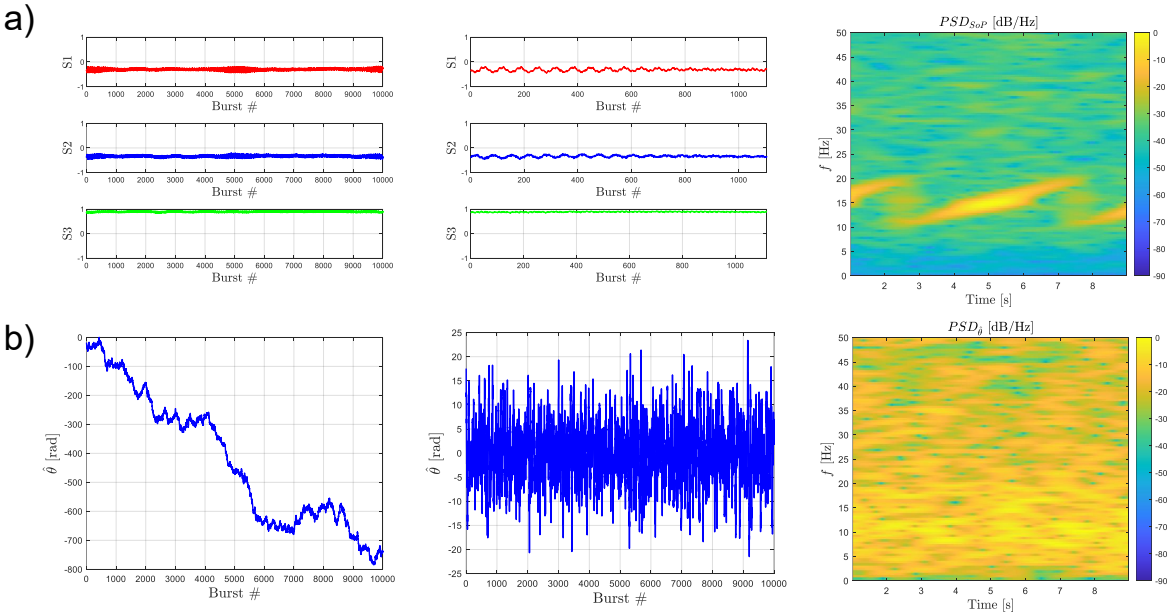

Fig. 4.12 Experimental results using both the SOP-based and phase-based sensing approaches over the 32-km metropolitan fiber link when a periodic 5-second frequency sweep between $f = 10\,\text{Hz}$ and $f = 20\,\text{Hz}$ is applied to the fiber. a) The Stokes parameters, a zoom and the spectrogram are reported. b) The optical phase, before and after DC component removal, and the spectrogram are reported.

These considerations are further supported by the experimental results obtained over the 32-km metropolitan fiber link during a 10-second acquisition, as shown in Fig. 4.11. In this experiment, the mechanical shaker remained active throughout the entire acquisition period. At the output of the metropolitan fiber, the PSD of the optical phase does not reveal any signature of the induced vibration. In this case, the spectral component corresponding to the vibration is completely submerged in backgorund noise, most likely generated by the pervasive micro-vibrations inherent to the urban environment. These background perturbations may arise from diverse sources such as vehicular traffic, nearby construction activity, and other events. In contrast, the SOP-based sensing approach demonstrates greater robustness to these external disturbances. The vibration-induced spectral component remains clearly distinguishable, with a separation of approximately 30 dB from the surrounding noise floor. This behavior is consistently observed even when the vibration is driven by a chirped sinusoidal waveform varying in frequency from 10 to 20 Hz with a 5-second periodicity, as illustrated in Fig. 4.12. Although these results may initially appear in contrast with those

reported in [93], it is important to consider the different experimental conditions. Specifically, two key factors distinguish this analysis: the environmental setting of the transmission and the nature of the induced perturbation. The measurements in this work were conducted over a live metropolitan fiber network located in the urban core of Turin, which presents a considerably noisier setting compared to suburban environments. Additionally, the induced vibration was deliberately kept at a low amplitude by using a mechanical shaker driven with a relatively weak sinusoidal excitation, in order to test the ultimate sensing capabilities in the two configurations. This study thus extends the scope of the comparison between phase- and SOP-based sensing by evaluating their performance under different propagation conditions. The results indicate that SOP-based sensing exhibits better robustness to weak perturbations and performs more reliably in the presence of environmental noise.

4.3 Conclusions

This work has investigated and experimentally tested the capabilities of DSP-based fiber sensing techniques leveraging coherent optical receivers, with a focus on two approaches: polarization-based sensing through SOP extraction and optical phase-based sensing. In the first part, the SOP-based approach has proved capable of detecting vibration-induced perturbations only when they result in angular deviations on the Poincaré sphere that are sufficiently large, typically on the order of several degrees. To enhance sensitivity and mitigate the impact of SOP estimation noise, a moving average applied over N_{win} samples of $\vec{S}[n]$ has been proposed. This post-processing technique significantly reduces the 99-th percentile $P_{99\%}(\Delta\theta)$ of the angular deviation, achieving values below 2 degrees across the entire range of tested OSNR values when $N_{\text{win}} = 15$. Moreover, the experimental and simulation results show a high degree of consistency. This indicates that the experimentally observed SOP estimation accuracy using a commercial coherent transceiver matches the performance under idealized simulation conditions. It is possible to conclude that the measured values of $P_{99\%}(\Delta\theta)$ reflect the intrinsic SOP estimation accuracy achievable at a given OSNR level, and are largely independent of the specific implementation of the receiver DSP. The second part presented a comparative analysis between SOP- and phase-based sensing, performed under identical transmission conditions over a 32-km metropolitan underground fiber link. In this noisy environment, SOP-based sensing demonstrated higher robustness against background perturbations, allowing a more precise detection of induced vibrations. Conversely, the phase-based approach showed relatively worse performance in this scenario, with induced vibrations submerged by environmental noise. Moreover, the extraction of phase information was found

to impose stricter hardware constraints, such as the requirement for ultra-low linewidth lasers to mitigate phase noise, which increases both system cost and complexity. SOP extraction, in contrast, can be implemented with minimal modifications to existing DSP algorithms and does not require hardware modifications. Overall, both methods are promising solutions for integrating fiber sensing capabilities into coherent transceivers. However, SOP-based sensing provides a better balance between complexity, robustness under practical deployment conditions, and feasibility for use in current optical networks.

Chapter 5

Conclusions

This thesis explored signal processing techniques for optical performance monitoring in both long-haul and metropolitan optical fiber links. It demonstrated how the digital signal processing already present in standard coherent receivers, beyond its conventional tasks, can be used to enable smarter, cost-efficient and flexible OPM solutions, and meet the evolving demands of modern optical networks. The research primarily focused on two complementary areas of OPM: digital longitudinal monitoring and optical fiber sensing.

Chapter 1 presented the fundamental principles of digital signal processing in modern coherent transceivers and provided a historical perspective on the evolution of OPM. Particular emphasis was placed on digital longitudinal monitoring, with a focus on longitudinal power monitoring algorithms, as well as on optical fiber sensing techniques, especially in the context of environmental monitoring using already-deployed optical fiber infrastructures.

Chapter 2 presented several novel applications of LPM, with particular emphasis on PDL estimation and localization, as well as the extension of LPM techniques to DSCM and UWB transmission scenarios. The chapter began by introducing a new PDL estimation algorithm for coherent optical links, which leverages the LLS-based LPM method. This approach was tested under operating conditions close to the optimal power regime, across a wide range of PDL values and in multiple-PDL configurations. In all tested scenarios, the algorithm consistently demonstrated high accuracy in estimating both the position and value of the inserted PDL. A comparative study was then carried out between the LLS-based algorithm and an alternative PDL estimation technique leveraging CM-based LPM [109]. While the CM-based method achieved generally higher sensitivity, detecting PDL values as low as 0.25 dB with a maximum error of only 0.058 dB, it required a more complex calibration

procedure. Moreover, in scenarios involving multiple PDL sources, only the LLS-based method succeeded in accurately estimating the end-to-end PDL, demonstrating its suitability for practical multi-span optical links. The analysis then shifted toward extending LPM applications to DSCM systems. A CM-based LPM approach was implemented and tested, revealing that, despite the introduction of a slightly higher noise in the estimated power profiles compared to single-carrier systems, the method provided comparable performance. This confirmed the adaptability of LPM to flexible transmission formats and supported ongoing research in this area. Finally, the chapter reported the experimental validation of LPM in a C+L band UWB transmission system employing full backward Raman amplification over a 540-km SSMF link. The LLS-based method was capable of accurately tracking the power evolution for both C- and L-band channels, with a maximum absolute error of less than 0.83 dB compared to OSA-based measurements. These results demonstrate the effectiveness of LPM in providing accurate, channel-resolved monitoring in challenging UWB scenarios, offering valuable support for the design, optimization, and real-time management of next-generation optical transmission networks.

Chapter 3 introduced a novel method for estimating Kerr-induced NLI in coherent optical transmission systems, fully integrated within the LLS-based LPM algorithm and solely relying on information available at receiver-side DSP. The approach was validated through extensive numerical simulations and experiments over 300-km and 1100-km links. It demonstrated high accuracy across a wide range of launch powers, even in typically challenging conditions for LPM. Comparisons with analytical NLI models and experimental measurements confirmed its reliability, especially for the purpose of power optimization. Despite its pros, the method has one main limitations: it captures only the SCI component of NLI. This issue was mitigated through simple correction factors derived from analytical NLI models. The chapter also addressed practical implementation challenges, particularly the use of HD symbols for reference signal reconstruction in LPM. Simulations revealed a predictable power offset related to the pre-FEC BER/SER, which can be compensated using a simple correction factor. Experimental validation showed that the resulting NLI estimation penalty remains within 0.3 dB. In summary, the work proposes LPM-based NLI estimation as a potential and accurate monitoring strategy, while also providing insights into its main limitations and implementation solutions.

Chapter 4 investigated the sensing capabilities of DSP-based length-integrated techniques using coherent optical receivers, focusing on two approaches: polarization-based sensing via SOP extraction and optical phase-based sensing. First, the accuracy of DSP-based SOP estimation was analyzed. To improve sensitivity and reduce estimation noise, a moving

average applied to the Stokes vector was introduced, lowering the 99-th percentile of the angular deviation to below 2° across all tested OSNR levels. Experimental and simulation results showed good agreement, confirming that the SOP estimation accuracy achievable with commercial coherent transceivers matches that predicted under ideal conditions and is generally independent of the specific DSP implementation. Then, a comparative experimental analysis of SOP- and phase-based sensing over a 32-km underground metropolitan fiber link was presented. In this scenario, SOP-based sensing proved more robust to background noise, enabling more precise detection of external induced vibrations. On the contrary, the phase-based method suffered from the impact of environmental noise and generally requires the use of ultra-narrow linewidth lasers to maintain phase accuracy, imposing stricter hardware constraints and increasing cost. SOP-based sensing could instead be realized with minimal changes to existing DSP architectures and without hardware modifications. In summary, while both techniques can potentially enable integrated fiber sensing in coherent transceivers, SOP-based sensing stands out as the more practical solution due to its lower complexity, higher robustness in noisy environments, and ease of implementation within current network infrastructures.

In conclusion, this thesis has demonstrated that DSP-based OPM represents a fundamental enabler for future high-capacity and flexible optical networks, as well as for environmental sensing. By leveraging the DSP in coherent transceivers, DSP-based OPM offers a cost-effective alternative to traditional hardware-based solutions, significantly reducing complexity and operational costs. Moreover, the ability to monitor multiple impairments simultaneously, using data already available within the receiver, enables a comprehensive and dynamic picture of link performance. The findings and methods presented in this work contribute to this ongoing evolution, providing both theoretical foundations and practical insights for the development of future optical performance monitoring solutions.

References

[1] R. S. Kerdock and D. H. Wolaver. Atlanta fiber system experiment: results of the atlanta experiment. *The Bell System Technical Journal*, 57(6):1857–1879, 1978.

[2] E. Desurvire, J. R. Simpson, and P. C. Becker. High-gain erbium-doped traveling-wave fiber amplifier. *Opt. Lett.*, 12(11):888–890, Nov 1987.

[3] A.R. Chraplyvy, A.H. Gnauck, R.W. Tkach, and R.M. Derosier. 8*10 Gb/s transmission through 280 km of dispersion-managed fiber. *IEEE Photonics Technology Letters*, 5(10):1233–1235, 1993.

[4] F. Derr. Coherent optical QPSK intradyne system: concept and digital receiver realization. *Journal of Lightwave Technology*, 10(9):1290–1296, 1992.

[5] M.G. Taylor. Coherent detection method using dsp for demodulation of signal and subsequent equalization of propagation impairments. *IEEE Photonics Technology Letters*, 16(2):674–676, 2004.

[6] Seb J. Savory. Digital filters for coherent optical receivers. *Opt. Express*, 16(2):804–817, Jan 2008.

[7] Junho Cho and Peter J. Winzer. Probabilistic constellation shaping for optical fiber communications. *Journal of Lightwave Technology*, 37(6):1590–1607, 2019.

[8] Ezra Ip and Joseph M. Kahn. Compensation of dispersion and nonlinear impairments using digital backpropagation. *J. Lightwave Technol.*, 26(20):3416–3425, Oct 2008.

[9] Peter J. Winzer, David T. Neilson, and Andrew R. Chraplyvy. Fiber-optic transmission and networking: the previous 20 and the next 20 years. *Opt. Express*, 26(18):24190–24239, Sep 2018.

[10] Devi Chadha. *Flexible Optical Networks*, pages 297–330. 2019.

[11] Zhenhua Dong, Faisal Nadeem Khan, Qi Sui, Kangping Zhong, Chao Lu, and Alan Pak Tao Lau. Optical performance monitoring: A review of current and future technologies. *Journal of Lightwave Technology*, 34(2):525–543, 2016.

[12] Fabian. N. Hauske, Maxim Kuschnerov, Bernhard Spinnler, and Berthold Lankl. Optical performance monitoring in digital coherent receivers. *Journal of Lightwave Technology*, 27(16):3623–3631, 2009.

[13] Ori Gerstel, Masahiko Jinno, Andrew Lord, and S.J. Ben Yoo. Elastic optical networking: a new dawn for the optical layer? *IEEE Communications Magazine*, 50(2):s12–s20, 2012.

[14] Danshi Wang, Yuchen Song, Yao Zhang, Xiaotian Jiang, Jiawei Dong, Faisal Nadeem Khan, Takeo Sasai, Shanguo Huang, Alan Pak Tao Lau, Massimo Tornatore, and Min Zhang. Digital twin of optical networks: A review of recent advances and future trends. *Journal of Lightwave Technology*, 42(12):4233–4259, 2024.

[15] Ezra Ip, Fabien Ravet, Hugo Martins, Ming-Fang Huang, Tatsuya Okamoto, Shaobo Han, Chaitnaya Narisetty, Jian Fang, Yue-Kai Huang, Milad Salemi, Etienne Rochat, Fabien Briffod, Alexandre Goy, Maria del Rosario Fernández-Ruiz, and Miguel González Herráez. Using global existing fiber networks for environmental sensing. *Proceedings of the IEEE*, 110(11):1853–1888, 2022.

[16] Antonio Mecozzi, Cristian Antonelli, Mikael Mazur, Nicolas Fontaine, Haoshuo Chen, Lauren Dallachiesa, and Roland Ryf. Use of optical coherent detection for environmental sensing. *Journal of Lightwave Technology*, 41(11):3350–3357, 2023.

[17] Kazuro Kikuchi. Fundamentals of coherent optical fiber communications. *Journal of Lightwave Technology*, 34(1):157–179, 2016.

[18] Maxim Kuschnerov, Fabian N. Hauske, Kittipong Piyawanno, Bernhard Spinnler, Mohammad S. Alfiad, Antonio Napoli, and Berthold Lankl. DSP for coherent single-carrier receivers. *J. Lightwave Technol.*, 27(16):3614–3622, Aug 2009.

[19] Md. Saifuddin Faruk and Seb J. Savory. Digital signal processing for coherent transceivers employing multilevel formats. *Journal of Lightwave Technology*, 35(5):1125–1141, 2017.

[20] Andreas Leven, Noriaki Kaneda, Ut-Va Koc, and Young-Kai Chen. Frequency estimation in intradyne reception. *IEEE Photonics Technology Letters*, 19(6):366–368, 2007.

[21] Xian Zhou, Xue Chen, and Keping Long. Wide-range frequency offset estimation algorithm for optical coherent systems using training sequence. *IEEE Photonics Technology Letters*, 24(1):82–84, 2012.

[22] Andrew J. Viterbi and Audrey M. Viterbi. Nonlinear estimation of PSK-modulated carrier phase with application to burst digital transmission. *IEEE Transactions on Information Theory*, 29(4):543–551, 1983.

[23] Milutin Pajovic, David S. Millar, Toshiaki Koike-Akino, Keisuke Kojima, Valeria Arlunno, and Kieran Parsons. Multi-pilot aided carrier phase estimation for single carrier coherent systems. In *Advanced Photonics 2015*, page SpT4D.4. Optica Publishing Group, 2015.

[24] Timo Pfau, Sebastian Hoffmann, and Reinhold Noe. Hardware-efficient coherent digital receiver concept with feedforward carrier recovery for *m* -QAM constellations. *Journal of Lightwave Technology*, 27(8):989–999, 2009.

[25] R. Friskney, K. Warbrick, S. Poliakoff, and R. Heath. Link-based photonic path performance prediction and control. In *2002 28TH European Conference on Optical Communication*, volume 3, pages 1–2, 2002.

[26] Vincent W. S. Chan, Katherine L. Hall, Eytan Modiano, and Kristin A. Rauschenbach. Architectures and technologies for high-speed optical data networks. *J. Lightwave Technol.*, 16(12):2146, Dec 1998.

[27] W.T. Anderson. The MONET project-a final report. In *Optical Fiber Communication Conference. Technical Digest Postconference Edition. Trends in Optics and Photonics Vol.37 (IEEE Cat. No. 00CH37079)*, volume 2, pages 148–149 vol.2, 2000.

[28] Giammarco Rossi, Timothy E. Dimmick, and Daniel J. Blumenthal. Optical performance monitoring in reconfigurable WDM optical networks using subcarrier multiplexing. *J. Lightwave Technol.*, 18(12):1639, Dec 2000.

[29] G. Ishikawa and H. Ooi. Polarization-mode dispersion sensitivity and monitoring in 40-gbit/s OTDM and 10-gbit/s NRZ transmission experiments. In *OFC '98. Optical Fiber Communication Conference and Exhibit. Technical Digest. Conference Edition.*

1998 OSA Technical Digest Series Vol.2 (IEEE Cat. No.98CH36177), pages 117–119, 1998.

[30] M. Teshima, M. Koga, and Ken-Ichi Sato. Performance of multiwavelength simultaneous monitoring circuit employing arrayed-waveguide grating. *Journal of Lightwave Technology*, 14(10):2277–2285, 1996.

[31] M. Rasztovits-Wiech, M. Danner, and W.R. Leeb. Optical signal-to-noise ratio measurement in WDM networks using polarization extinction. In *24th European Conference on Optical Communication. ECOC '98 (IEEE Cat. No.98TH8398)*, volume 1, pages 549–550 vol.1, 1998.

[32] M. Rohde, E.-J. Bachus, and F. Raub. Monitoring of transmission impairments in long-haul transmission systems using the novel digital control modulation technique. In *2002 28TH European Conference on Optical Communication*, volume 3, pages 1–2, 2002.

[33] A. R. Chraplyvy, R. W. Tkach, L. L. Buhl, and R. C. Alferness. Phase modulation to amplitude modulation conversion of cw laser light in optical fibers. In *Optical Fiber Communication*, page PD10. Optica Publishing Group, 1986.

[34] M.N. Petersen, Z. Pan, S. Lee, S.A. Havstad, and A.E. Willner. Online chromatic dispersion monitoring and compensation using a single inband subcarrier tone. *IEEE Photonics Technology Letters*, 14(4):570–572, 2002.

[35] Qian Yu, Zhongqi Pan, Lian-Shan Yan, and A.E. Willner. Chromatic dispersion monitoring technique using sideband optical filtering and clock phase-shift detection. *Journal of Lightwave Technology*, 20(12):2267–2271, 2002.

[36] F. Roy, C. Francia, F. Bruyere, and D. Penninckx. A simple dynamic polarization mode dispersion compensator. In *OFC/IOOC . Technical Digest. Optical Fiber Communication Conference, 1999, and the International Conference on Integrated Optics and Optical Fiber Communication*, volume 1, pages 275–278 vol.1, 1999.

[37] I. Shake, H. Takara, K. Uchiyama, and Y. Yamabayashi. Quality monitoring of optical signals influenced by chromatic dispersion in a transmission fiber using averaged q-factor evaluation. *IEEE Photonics Technology Letters*, 13(4):385–387, 2001.

[38] D.C. Kilper, R. Bach, D.J. Blumenthal, D. Einstein, T. Landolsi, L. Ostar, M. Preiss, and A.E. Willner. Optical performance monitoring. *Journal of Lightwave Technology*, 22(1):294–304, 2004.

[39] Zhiping Jiang and Simin Wang. Diagnosing transient behavior during channel add/drop by real-time performance monitoring. In *OSA Advanced Photonics Congress 2021*, page NeF2B.5. Optica Publishing Group, 2021.

[40] Yvan Pointurier. Design of low-margin optical networks. *Journal of Optical Communications and Networking*, 9(1):A9–A17, 2017.

[41] Petros Ramantanis, Camille Delezoide, Patricia Layec, and Sebastien Bigo. Revisiting the calculation of performance margins in monitoring-enabled optical networks. *Journal of Optical Communications and Networking*, 11(10):C67–C75, 2019.

[42] G. Bosco, R. Cigliutti, E. Torrengo, A. Carena, V. Curri, P. Poggiolini, and F. Forghieri. Joint DGD, PDL and chromatic dispersion estimation in ultra-long-haul WDM transmission experiments with coherent receivers. In *36th European Conference and Exhibition on Optical Communication*, pages 1–3, 2010.

[43] H. Ji, K. Park, J. Lee, H. Chung, E. Son, K. Han, S. Jun, and Y. Chung. Optical performance monitoring techniques based on pilot tones for WDM networkapplications. *J. Opt. Netw.*, 3(7):510–533, Jul 2004.

[44] Zhiping Jiang, Xuefeng Tang, Simin Wang, Ge Gao, Dajiang Jin, Jianfeng Wang, and Minggang Si. DSP enabled, amplitude modulation pilot tone based optical performance monitoring in coherent systems. In *2021 European Conference on Optical Communication (ECOC)*, pages 1–4, 2021.

[45] Zhiping Jiang and Xuefeng Tang. Low-cost signal spectrum monitoring enabled by multiband pilot tone techniques. In *2018 European Conference on Optical Communication (ECOC)*, pages 1–3, 2018.

[46] Zhiping Jiang, Ge Gao, Xuefeng Tang, Dajiang Jin, Minggang Si, and Dong Zhu. Demonstration of real-time filter fault identification and localization using dual-band pilot tone detection enabled by an ASIC chip. In *45th European Conference on Optical Communication (ECOC 2019)*, pages 1–3, 2019.

[47] Zhiping Jiang, Xuefeng Tang, Simin Wang, Ge Gao, Dajiang Jin, Jianfeng Wang, and Minggang Si. Progresses of pilot tone based optical performance monitoring in coherent systems. *Journal of Lightwave Technology*, 40(10):3128–3136, 2022.

[48] Zhiping Jiang, Simin Wang, Xuefeng Tang, Jianfeng Wang, Dajiang Jin, Hao Yang, and Minggang Si. Direct nonlinear noise monitoring for in-service signals in coherent systems. In *2020 European Conference on Optical Communications (ECOC)*, pages 1–4, 2020.

[49] Xiaoxia Wu, Jeffrey A. Jargon, Ronald A. Skoog, Loukas Paraschis, and Alan E. Willner. Applications of artificial neural networks in optical performance monitoring. *Journal of Lightwave Technology*, 27(16):3580–3589, 2009.

[50] Thomas Shun Rong Shen, Qi Sui, and Alan Pak Tao Lau. OSNR monitoring for PM-QPSK systems with large inline chromatic dispersion using artificial neural network technique. *IEEE Photonics Technology Letters*, 24(17):1564–1567, 2012.

[51] Faisal Nadeem Khan, Kangping Zhong, Xian Zhou, Waled Hussein Al-Arashi, Changyuan Yu, Chao Lu, and Alan Pak Tao Lau. Joint OSNR monitoring and modulation format identification in digital coherent receivers using deep neural networks. *Opt. Express*, 25(15):17767–17776, Jul 2017.

[52] Danshi Wang, Mengyuan Wang, Min Zhang, Zhiguo Zhang, Hui Yang, Jin Li, Jianqiang Li, and Xue Chen. Cost-effective and data size adaptive OPM at intermediated node using convolutional neural network-based image processor. *Opt. Express*, 27(7):9403–9419, Apr 2019.

[53] Josh W. Nevin, Sam Nallaperuma, and Seb J. Savory. Gaussian process-driven history matching for physical layer parameter estimation in optical fiber communication networks, 2022.

[54] Yuchen Song, Yao Zhang, Chunyu Zhang, Jin Li, Min Zhang, and Danshi Wang. PINN for power evolution prediction and raman gain spectrum identification in C+L-band transmission system. In *2023 Optical Fiber Communications Conference and Exhibition (OFC)*, pages 1–3, 2023.

[55] Takeo Sasai, Minami Takahashi, Runa Kaneko, Yoshiaki Sone, Masanori Nakamura, and Etsushi Yamazaki. Recent advances in digital longitudinal monitoring of fiber-optic link. In *2024 Optical Fiber Communications Conference and Exhibition (OFC)*, pages 1–3, 2024.

[56] P. Serena, C. Lasagni, A. Bononi, F. Boitier, A. May, P. Ramantanis, and M. Lonardi. Locating fiber loss anomalies with a receiver-side monitoring algorithm exploiting cross-phase modulation. In *2023 Optical Fiber Communications Conference and Exhibition (OFC)*, pages 1–3, 2023.

[57] Ronen Dar, Meir Feder, Antonio Mecozzi, and Mark Shtaif. Properties of nonlinear noise in long, dispersion-uncompensated fiber links. *Opt. Express*, 21(22):25685–25699, Nov 2013.

[58] Takahito Tanimura, Kazuyuki Tajima, Setsuo Yoshida, Shoichiro Oda, and Takeshi Hoshida. Experimental demonstration of a coherent receiver that visualizes longitudinal signal power profile over multiple spans out of its incoming signal. In *45th European Conference on Optical Communication (ECOC 2019)*, pages 1–4, 2019.

[59] Takahito Tanimura, Setsuo Yoshida, Kazuyuki Tajima, Shoichiro Oda, and Takeshi Hoshida. Fiber-longitudinal anomaly position identification over multi-span transmission link out of receiver-end signals. *Journal of Lightwave Technology*, 38(9):2726–2733, 2020.

[60] Matheus Sena, Robert Emmerich, Behnam Shariati, Caio Santos, Antonio Napoli, Johannes K. Fischer, and Ronald Freund. DSP-based link tomography for amplifier gain estimation and anomaly detection in C+L-band systems. *Journal of Lightwave Technology*, 40(11):3395–3405, 2022.

[61] Choloong Hahn, Junho Chang, and Zhiping Jiang. Localization of reflection induced multi-path-interference over multi-span transmission link by receiver-side digital signal processing. In *2022 Optical Fiber Communications Conference and Exhibition (OFC)*, pages 1–3, 2022.

[62] Takeo Sasai, Masanori Nakamura, Seiji Okamoto, Fukutaro Hamaoka, Shuto Yamamoto, Etsushi Yamazaki, Asuka Matsushita Hideki Nishizawa, and Yoshiaki Kisaka. Simultaneous detection of anomaly points and fiber types in multi-span transmission links only by receiver-side digital signal processing. In *2020 Optical Fiber Communications Conference and Exhibition (OFC)*, pages 1–3, 2020.

[63] Takeo Sasai, Masanori Nakamura, Etsushi Yamazaki, Shuto Yamamoto, Hideki Nishizawa, and Yoshiaki Kisaka. Digital longitudinal monitoring of optical fiber communication link. *Journal of Lightwave Technology*, 40(8):2390–2408, 2022.

[64] Takeo Sasai, Masanori Nakamura, Etsushi Yamazaki, and Yoshiaki Kisaka. Precise longitudinal power monitoring over 2,080 km enabled by step size selection of split step fourier method. In *2022 Optical Fiber Communications Conference and Exhibition (OFC)*, pages 1–3, 2022.

[65] Takeo Sasai, Etsushi Yamazaki, Masanori Nakamura, and Yoshiaki Kisaka. Proposal of linear least squares for fiber-nonlinearity-based longitudinal power monitoring in multi-span link. In *2022 27th OptoElectronics and Communications Conference (OECC) and 2022 International Conference on Photonics in Switching and Computing (PSC)*, pages 1–4, 2022.

[66] Takeo Sasai, Minami Takahashi, Masanori Nakamura, Etsushi Yamazaki, and Yoshiaki Kisaka. Linear least squares estimation of fiber-longitudinal optical power profile. *Journal of Lightwave Technology*, 42(6):1955–1965, 2024.

[67] Inwoong Kim, Olga Vassilieva, Ryu Shinzaki, Motohiko Eto, Shoichiro Oda, and Paparao Palacharla. Robust longitudinal power profile estimation in optical networks using MMSE with complex scaling factor. In *2023 Optical Fiber Communications Conference and Exhibition (OFC)*, pages 1–3, 2023.

[68] T. Sasai, Y. Sone, E. Yamazaki, M. Nakamura, and Y. Kisaka. A generalized method for fiber-longitudinal power profile estimation. In *49th European Conference on Optical Communications (ECOC 2023)*, volume 2023, pages 1150–1153, 2023.

[69] Fabien Boitier, Alessandro Pacini, Alix May, and Patricia Layec. A multi-stage method for least-square based longitudinal power profile computation. In *2025 Optical Fiber Communications Conference and Exhibition (OFC)*, pages 1–3, 2025.

[70] A. May, F. Boitier, E. Awwad, P. Ramantanis, M. Lonardi, and P. Ciblat. Receiver-based experimental estimation of power losses in optical networks. *IEEE Photonics Technology Letters*, 33(22):1238–1241, 2021.

[71] Takeo Sasai, Etsushi Yamazaki, and Yoshiaki Kisaka. Performance limit of fiber-longitudinal power profile estimation methods. *Journal of Lightwave Technology*, 41(11):3278–3289, 2023.

[72] Alix May, Fabien Boitier, and Patricia Layec. Accuracy assessment of power profile estimation using MMSE or deconvoluted profiles. *Journal of Lightwave Technology*, 43(14):6460–6468, 2025.

[73] Alix May, Fabien Boitier, Alexis Carbo Meseguer, Juan Uriel Esparza, Philippe Plantady, Alain Calsat, and Patricia Layec. Longitudinal power monitoring over a deployed 10,000-km link for submarine systems. In *2023 Optical Fiber Communications Conference and Exhibition (OFC)*, pages 1–3, 2023.

[74] Matheus Sena, Pratim Hazarika, Caio Santos, Bruno Correia, Robert Emmerich, Behnam Shariati, Antonio Napoli, Vittorio Curri, Wladek Forysiak, Colja Schubert, Johannes K. Fischer, and Ronald Freund. Advanced DSP-based monitoring for spatially resolved and wavelength-dependent amplifier gain estimation and fault location in C+L-band systems. *Journal of Lightwave Technology*, 41(3):989–998, 2023.

[75] M. Eto, K. Tajima, K. Sone, S. Yoshida, R. Shinzaki, S. Oda, and T. Hoshida. Fibre type identification based on power profile estimation. In *49th European Conference on Optical Communications (ECOC 2023)*, volume 2023, pages 127–130, 2023.

[76] Takeo Sasai, Giacomo Borraccini, Yue-Kai Huang, Hideki Nishizawa, Zehao Wang, Tingjun Chen, Yoshiaki Sone, Tatsuya Matsumura, Masanori Nakamura, Etsushi Yamazaki, and Yoshiaki Kisaka. 4D optical link tomography: First field demonstration of autonomous transponder capable of distance, time, frequency, and polarization resolved monitoring. In *2024 Optical Fiber Communications Conference and Exhibition (OFC)*, pages 1–3, 2024.

[77] Matheus Sena, Abdelrahmane Moawad, Robert Emmerich, Behnam Shariati, Marc Geitz, Ralf-Peter Braun, Johannes Fischer, and Ronald Freund. Exploring the potential of longitudinal power monitoring for detecting physical-layer attacks. *J. Opt. Commun. Netw.*, 17(7):C30–C40, Jul 2025.

[78] Alessandro Pacini, Fabien Boitier, Alix May, Vinod Bajaj, Andrea Sgambelluri, Alessio Giorgetti, Luca Valcarenghi, and Patricia Layec. Longitudinal power profile monitoring telemetry enabling self-healing optical networks. *Journal of Optical Communications and Networking*, 17(7):580–589, 2025.

[79] Govind P. Agrawal. *Nonlinear Fiber Optics*. Academic Press, Cambridge, MA, 6th edition, 2019.

[80] Robert W. Boyd. *Nonlinear Optics*. Academic Press, Amsterdam, 3rd edition, 2008.

[81] Ronen Dar, Meir Feder, Antonio Mecozzi, and Mark Shtaif. Pulse collision picture of inter-channel nonlinear interference in fiber-optic communications. *Journal of Lightwave Technology*, 34(2):593–607, 2016.

[82] Pierluigi Poggiolini. The gn model of non-linear propagation in uncompensated coherent optical systems. *J. Lightwave Technol.*, 30(24):3857–3879, Dec 2012.

[83] Ronen Dar, Meir Feder, Antonio Mecozzi, and Mark Shtaif. Accumulation of nonlinear interference noise in fiber-optic systems. *Opt. Express*, 22(12):14199–14211, Jun 2014.

[84] Andrea Carena, Gabriella Bosco, Vittorio Curri, Yanchao Jiang, Pierluigi Poggiolini, and Fabrizio Forghieri. Egn model of non-linear fiber propagation. *Opt. Express*, 22(13):16335–16362, Jun 2014.

[85] Dario Pilori, Mattia Cantono, Andrea Carena, and Vittorio Curri. FFSS: The fast fiber simulator software. In *2017 19th International Conference on Transparent Optical Networks (ICTON)*, pages 1–4, 2017.

[86] A. Vannucci, P. Serena, and A. Bononi. The RP method: a new tool for the iterative solution of the nonlinear schrodinger equation. *Journal of Lightwave Technology*, 20(7):1102–1112, 2002.

[87] Paolo Serena and Alberto Bononi. An alternative approach to the gaussian noise model and its system implications. *Journal of Lightwave Technology*, 31(22):3489–3499, 2013.

[88] L. Minelli, S. Pellegrini, L. Andrenacci, D. Pilori, G. Bosco, L. D. Chiesa, A. Tanzi, C. Crognale, and R. Gaudino. SOP-based DSP blind anomaly detection for sensing on deployed metropolitan fibers. In *49th European Conference on Optical Communications (ECOC 2023)*, volume 2023, pages 519–522, 2023.

[89] Saverio Pellegrini, Giuseppe Rizzelli, Marco Barla, and Roberto Gaudino. Algorithm optimization for rockfalls alarm system based on fiber polarization sensing. *IEEE Photonics Journal*, 15(3):1–9, 2023.

[90] Kristina Shizuka Yamase Skarvang, Steinar Bjørnstad, Robin André Rørstadbotnen, Kurosh Bozorgebrahimi, and Dag Roar Hjelme. Observation of local small magnitude earthquakes using state of polarization monitoring in a 250km passive arctic submarine communication cable. In *2023 Optical Fiber Communications Conference and Exhibition (OFC)*, pages 1–3, 2023.

[91] Kristina Shizuka Yamase Skarvang, Steinar Bjørnstad, Erik Sæthre, and Dag Roar Hjelme. Local wind impact sensing using state of polarization measurement on a live

short-haul aerial fibre cable. In *2024 Optical Fiber Communications Conference and Exhibition (OFC)*, pages 1–3, 2024.

[92] Douglas Charlton, Steven Clarke, David Doucet, Maurice O'Sullivan, Daniel L Peterson, Darryl Wilson, Glenn Wellbrock, and Michel Bélanger. Field measurements of SOP transients in OPGW, with time and location correlation to lightning strikes. *Opt. Express*, 25(9):9689–9696, May 2017.

[93] Ezra Ip, Yue-Kai Huang, Glenn Wellbrock, Tiejun Xia, Ming-Fang Huang, Ting Wang, and Yoshiaki Aono. Vibration detection and localization using modified digital coherent telecom transponders. *Journal of Lightwave Technology*, 40(5):1472–1482, 2022.

[94] Charles J. Carver and Xia Zhou. Polarization sensing of network health and seismic activity over a live terrestrial fiber-optic cable. *Communications Engineering*, 3(1):91, 2024.

[95] Giuseppe Marra, Cecilia Clivati, Richard Luckett, Anna Tampellini, Jochen Kronjäger, Louise Wright, Alberto Mura, Filippo Levi, Stephen Robinson, André Xuereb, Brian Baptie, and Davide Calonico. Ultrastable laser interferometry for earthquake detection with terrestrial and submarine cables. *Science*, 361(6401):486–490, 2018.

[96] Jianwei Tang, Xueyang Li, Chen Cheng, Yaguang Hao, Bang Yang, Jiali Li, Zhixue He, Yanfu Yang, and Weisheng Hu. Forward-transmission based distributed fiber sensing compatible with C+L unidirectional communication systems. In *2024 Optical Fiber Communications Conference and Exhibition (OFC)*, pages 1–3, 2024.

[97] Rudi Bratovich, Fransisco Martinez R., Stefano Straullu, Emanuele Virgillito, Andrea Castoldi, Andrea D'Amico, Francesco Aquilino, Rosanna Pastorelli, and Vittorio Curri. Surveillance of metropolitan anthropic activities by WDM 10g optical data channels. In *2022 European Conference on Optical Communication (ECOC)*, pages 1–4, 2022.

[98] Saverio Pellegrini, Leonardo Minelli, Lorenzo Andrenacci, Giuseppe Rizzelli, Dario Pilori, Gabriella Bosco, Luca Della Chiesa, Claudio Crognale, Stefano Piciaccia, and Roberto Gaudino. Overview on the state of polarization sensing: application scenarios and anomaly detection algorithms. *Journal of Optical Communications and Networking*, 17(2):A196–A209, 2025.

[99] Ezra Ip, Jian Fang, Yaowen Li, Qiang Wang, Ming-Fang Huang, Milad Salemi, and Yue-Kai Huang. Distributed fiber sensor network using telecom cables as sensing media: technology advancements and applications [invited]. *Journal of Optical Communications and Networking*, 14(1):A61–A68, 2022.

[100] J.C. Juarez, E.W. Maier, Kyoo Nam Choi, and H.F. Taylor. Distributed fiber-optic intrusion sensor system. *Journal of Lightwave Technology*, 23(6):2081–2087, 2005.

[101] Yi Weng, Ezra Ip, Zhongqi Pan, and Ting Wang. Single-end simultaneous temperature and strain sensing techniques based on brillouin optical time domain reflectometry in few-mode fibers. *Opt. Express*, 23(7):9024–9039, Apr 2015.

[102] Mark B. Hausner, Francisco Suárez, Kenneth E. Glander, Nick van de Giesen, John S. Selker, and Scott W. Tyler. Calibrating single-ended fiber-optic raman spectra distributed temperature sensing data. *Sensors*, 11(11):10859–10879, 2011.

[103] Ezra Ip, Yue-Kai Huang, Ming-Fang Huang, Milad Salemi, Yaowen Li, Ting Wang, Yoshiaki Aono, Glenn A Wellbrock, and Tiejun J Xia. Distributed fiber sensor network using telecom cables as sensing media: Applications. In *2021 Optical Fiber Communications Conference and Exhibition (OFC)*, pages 1–3, 2021.

[104] John C. Cartledge and Ahmed I. Abd El-Rahman. Impact of transceiver noise on the outage probability due to polarization dependent loss. *IEEE Photonics Technology Letters*, 33(1):59–62, 2021.

[105] Olga Vassilieva, Inwoong Kim, Youichi Akasaka, Martin Bouda, and Motoyoshi Sekiya. Interplay between PDL and nonlinear effects in coherent polarization multiplexed systems. *Opt. Express*, 19(26):B357–B362, Dec 2011.

[106] Dequan Xie, Danshi Wang, Min Zhang, Zichen Liu, Quan You, Qi Yang, and Shaohua Yu. LCoS-based wavelength-selective switch for future finer-grid elastic optical networks capable of all-optical wavelength conversion. *IEEE Photonics Journal*, 9(2):1–12, 2017.

[107] Lynn E. Nelson, Cristian Antonelli, Antonio Mecozzi, Martin Birk, Peter Magill, Anton Schex, and Lutz Rapp. Statistics of polarization dependent loss in an installed long-haul WDM system. *Opt. Express*, 19(7):6790–6796, Mar 2011.

[108] Arnaud Dumenil, Elie Awwad, and Cyril Méasson. PDL in optical links: A model analysis and a demonstration of a PDL-resilient modulation. *Journal of Lightwave Technology*, 38(18):5017–5025, 2020.

[109] Alix May, Elie Awwad, Petros Ramantanis, and Philippe Ciblat. Receiver-based localization and estimation of polarization dependent loss. In *2022 27th OptoElectronics and Communications Conference (OECC) and 2022 International Conference on Photonics in Switching and Computing (PSC)*, pages 1–4, 2022.

[110] Guoxiu Huang, Shoichiro Oda, Yuichi Akiyama, Hiroyuki Irie, Setsuo Yoshida, Hisao Nakashima, and Takeshi Hoshida. Polarization dependent loss monitor with visualization on poincaré sphere in digital coherent system. In *2017 European Conference on Optical Communication (ECOC)*, pages 1–3, 2017.

[111] Bartlomiej Kozicki, Hidehiko Takara, Tetsuro Inui, Tetsuro Komukai, Kunihiko Mori, and Kazushige Yonenaga. Monitoring of orthogonal polarization power ratio due to PDL using intensity tones in polarization multiplexed signals. In *2011 Optical Fiber Communication Conference and Exposition and the National Fiber Optic Engineers Conference*, pages 1–3, 2011.

[112] Zhiping Jiang and Xiang Lin. Distributed polarization dependent loss monitoring using polarization resolved pilot tone. In *2022 European Conference on Optical Communication (ECOC)*, pages 1–4, 2022.

[113] A. Mecozzi and M. Shtaif. The statistics of polarization-dependent loss in optical communication systems. *IEEE Photonics Technology Letters*, 14(3):313–315, 2002.

[114] Segev Zarkosvky and Mark Shtaif. Statistical distribution of polarization-dependent loss in systems characterized by the hinge model. *Opt. Lett.*, 45(5):1224–1227, Mar 2020.

[115] Joana Girard-Jollet, Matteo Lonardi, Petros Ramantanis, Paolo Serena, Chiara Lasagni, Patricia Layec, and Jean-Christophe Antona. Estimating network components PDL using performance statistical measurements. *Journal of Lightwave Technology*, 40(16):5407–5415, 2022.

[116] Motohiko Eto, Kazuyuki Tajima, Setsuo Yoshida, Shoichiro Oda, and Takeshi Hoshida. Location-resolved pdl monitoring with rx-side digital signal processing in multi-span optical transmission system. In *Optical Fiber Communication Conference (OFC) 2022*, page Th1C.2. Optica Publishing Group, 2022.

[117] Minami Takahashi, Takeo Sasai, Etsushi Yamazaki, and Yoshiaki Kisaka. Monitoring PDL value and location using DSP-based longitudinal power profile estimation. *Journal of Lightwave Technology*, 42(17):5866–5873, 2024.

[118] Takeo Sasai, Minami Takahashi, Masanori Nakamura, Etsushi Yamazaki, and Yoshiaki Kisaka. On the signal pattern effect on fibre-longitudinal power monitor. In *ECOC 2024; 50th European Conference on Optical Communication*, pages 160–163, 2024.

[119] Rongqing Hui, Benyuan Zhu, Renxiang Huang, C.T. Allen, K.R. Demarest, and D. Richards. Subcarrier multiplexing for high-speed optical transmission. *Journal of Lightwave Technology*, 20(3):417–427, 2002.

[120] David Krause, Ahmed Awadalla, Abdullah S. Karar, Han Sun, and Kuang-Tsan Wu. Design considerations for a digital subcarrier coherent optical modem. In *2017 Optical Fiber Communications Conference and Exhibition (OFC)*, pages 1–3, 2017.

[121] Yuanyuan Zhang, Maurice O'Sullivan, and Rongqing Hui. Digital subcarrier multiplexing for flexible spectral allocation in optical transport network. *Opt. Express*, 19(22):21880–21889, Oct 2011.

[122] Pierluigi Poggiolini, Antonino Nespola, Yanchao Jiang, Gabriella Bosco, Andrea Carena, Luca Bertignono, Syed Muhammad Bilal, Silvio Abrate, and Fabrizio Forghieri. Analytical and experimental results on system maximum reach increase through symbol rate optimization. *Journal of Lightwave Technology*, 34(8):1872–1885, 2016.

[123] Dave Welch, Antonio Napoli, Johan Bäck, Sanketh Buggaveeti, Carlos Castro, Aaron Chase, Xi Chen, Vince Dominic, Thomas Duthel, Tobias A. Eriksson, Sezer Erkilinç, Peter Evans, Chris R. S. Fludger, Ben Foo, Thomas Frost, Paul Gavrilovic, Steven J. Hand, Aditya Kakkar, Ales Kumpera, Vikrant Lal, Robert Maher, Fabio Marques, Fady Masoud, Atul Mathur, Ray Milano, Miguel Iglesias Olmedo, Magnus Olson, Don Pavinski, João Pedro, Amir Rashidinejad, Parmijit Samra, Warren Sande, Azmina Somani, Han Sun, Norman Swenson, Huan-Shang Tsai, Amin Yekani, Jiaming Zhang, and Mehrdad Ziari. Digital subcarrier multiplexing: Enabling software-configurable optical networks. *Journal of Lightwave Technology*, 41(4):1175–1191, 2023.

[124] Han Sun, Mehdi Torbatian, Mehdi Karimi, Robert Maher, Sandy Thomson, Mohsen Tehrani, Yuliang Gao, Ales Kumpera, George Soliman, Aditya Kakkar, Mohammad Osman, Ziad A. El-Sahn, Clayton Doggart, Weikun Hou, Shailesh Sutarwala, Yuejian

Wu, Mohammad Reza Chitgarha, Vikrant Lal, Huan-Shang Tsai, Scott Corzine, Jiaming Zhang, John Osenbach, Sanketh Buggaveeti, Zulfikar Morbi, Miguel Iglesias Olmedo, Irene Leung, Xian Xu, Parmijit Samra, Vince Dominic, Steve Sanders, Mehrdad Ziari, Antonio Napoli, Bernhard Spinnler, Kuang-Tsan Wu, and Parthiban Kandappan. 800g DSP ASIC design using probabilistic shaping and digital sub-carrier multiplexing. *Journal of Lightwave Technology*, 38(17):4744–4756, 2020.

[125] Fred Buchali, Fabian Steiner, Georg Böcherer, Laurent Schmalen, Patrick Schulte, and Wilfried Idler. Rate adaptation and reach increase by probabilistically shaped 64-QAM: An experimental demonstration. *Journal of Lightwave Technology*, 34(7):1599–1609, 2016.

[126] I. Kim, O. Vassilieva, R. Shinzaki, M. Eto, S. Oda, and P. Palacharla. Multi-channel longitudinal power profile estimation. In *49th European Conference on Optical Communications (ECOC 2023)*, volume 2023, pages 491–494, 2023.

[127] Takeshi Hoshida, Vittorio Curri, Lidia Galdino, David T. Neilson, Wladek Forysiak, Johannes K. Fischer, Tomoyuki Kato, and Pierluigi Poggiolini. Ultrawideband systems and networks: Beyond C + L-band. *Proceedings of the IEEE*, 110(11):1725–1741, 2022.

[128] Jeremie Renaudier, Antonio Napoli, Maria Ionescu, Cosimo Calò, Gerrit Fiol, Vitaly Mikhailov, Wladek Forysiak, Nicolas Fontaine, Francesco Poletti, and Pierluigi Poggiolini. Devices and fibers for ultrawideband optical communications. *Proceedings of the IEEE*, 110(11):1742–1759, 2022.

[129] Wayne S. Pelouch. Raman amplification: An enabling technology for long-haul coherent transmission systems. *Journal of Lightwave Technology*, 34(1):6–19, 2016.

[130] M. Cantono, A. Ferrari, D. Pilori, E. Virgillito, J. L. Augé, and V. Curri. Physical layer performance of multi-band optical line systems using raman amplification. *Journal of Optical Communications and Networking*, 11(1):A103–A110, 2019.

[131] Runa Kaneko, Takeo Sasai, Fukutaro Hamaoka, Masanori Nakamura, and Etsushi Yamazaki. Fiber longitudinal monitoring of inter-band-SRS-induced power transition in S+C+L WDM transmission. In *2024 Optical Fiber Communications Conference and Exhibition (OFC)*, pages 1–3, 2024.

[132] Inwoong Kim, Kyousuke Sone, Olga Vassilieva, Shoichiro Oda, Paparao Palacharla, and Takeshi Hoshida. Nonlinear SNR estimation based on power profile estimation in

hybrid raman-EDFA link. In *2024 Optical Fiber Communications Conference and Exhibition (OFC)*, pages 1–3, 2024.

[133] Richard L. Sutherland. *Handbook of Nonlinear Optics*. Optical Science and Engineering. CRC Press, Boca Raton, FL, 2nd edition, 2003.

[134] M.A. Farahani and T. Gogolla. Spontaneous raman scattering in optical fibers with modulated probe light for distributed temperature raman remote sensing. *Journal of Lightwave Technology*, 17(8):1379–1391, 1999.

[135] André Souza, Nelson Costa, Jo ao Pedro, and Jo ao Pires. Raman amplifier design and launch power optimization in multi-band optical systems. *J. Opt. Commun. Netw.*, 17(1):A13–A22, Jan 2025.

[136] Akira Naka and Toshiya Matsuda. Operational issues facing commercial raman amplifier system: Safety measures and system designs. In *2015 Optical Fiber Communications Conference and Exhibition (OFC)*, pages 1–3, 2015.

[137] Malin Premaratne. Analytical characterization of optical power and noise figure of forward pumped raman amplifiers. *Opt. Express*, 12(18):4235–4245, Sep 2004.

[138] Rongqing Hui, Youichi Akasaka, and Paparao Palacharla. Investigation of forward and backward pumped distributed raman amplification schemes for a single-span 600gb/s coherent fiber system. In *26th Optoelectronics and Communications Conference*, page W4B.5. Optica Publishing Group, 2021.

[139] Vittorio Curri and Andrea Carena. Merit of raman pumping in uniform and uncompensated links supporting nywdm transmission. *Journal of Lightwave Technology*, 34(2):554–565, 2016.

[140] Yanchao Jiang, Antonino Nespola, Stefano Straullu, Alberto Tanzi, Stefano Piciaccia, Fabrizio Forghieri, Dario Pilori, and Pierluigi Poggiolini. Closed-form EGN model with comprehensive raman support. In *ECOC 2024; 50th European Conference on Optical Communication*, pages 1431–1434, 2024.

[141] Henrique Buglia, Robert I. Killey, and Polina Bayvel. Ultra-wideband modeling of optical fibre nonlinearity in hybrid-amplified links. *Journal of Lightwave Technology*, 42(24):8664–8677, 2024.

[142] Jad Sarkis, Yanchao Jiang, Stefano Piciaccia, Fabrizio Forghieri, and Pierluigi Poggiolini. Signal and raman pump launch power optimization in a C+L+S+E system using fast power profile estimation. In *2025 Optical Fiber Communications Conference and Exhibition (OFC)*, pages 1–3, 2025.

[143] Christian Malouin, Philip Thomas, Bo Zhang, Jason O'Neil, and Ted Schmidt. Natural expression of the best-match search godard clock-tone algorithm for blind chromatic dispersion estimation in digital coherent receivers. In *Advanced Photonics Congress*, page SpTh2B.4. Optica Publishing Group, 2012.

[144] M. Santagiustina, C. G. Someda, G. Vadalà, S. Combrié, and A. De Rossi. Theory of slow light enhanced four-wave mixing in photonic crystal waveguides. *Opt. Express*, 18(20):21024–21029, Sep 2010.

[145] Pierluigi Poggiolini and Mahdi Ranjbar-Zefreh. Closed form expressions of the nonlinear interference for UWB systems. In *2022 European Conference on Optical Communication (ECOC)*, pages 1–4, 2022.

[146] Md. Saifuddin Faruk and Seb J. Savory. Measurement informed models and digital twins for optical fiber communication systems. *Journal of Lightwave Technology*, 42(3):1016–1030, 2024.

[147] Seb J. Savory. Digital coherent optical receivers: Algorithms and subsystems. *IEEE Journal of Selected Topics in Quantum Electronics*, 16(5):1164–1179, 2010.

[148] Leonardo Minelli, Gabriella Bosco, Stefano Straullu, Antonino Nespola, Stefano Piciaccia, and Dario Pilori. Dsp-based inter-channel interference monitoring in flexible wavelength-routed networks. *Journal of Optical Communications and Networking*, 16(6):695–705, 2024.

[149] P. Poggiolini, G. Bosco, A. Carena, V. Curri, Y. Jiang, and F. Forghieri. The gn-model of fiber non-linear propagation and its applications. *Journal of Lightwave Technology*, 32(4):694–721, 2014.

[150] Alex Alvarado, Tobias Fehenberger, Bin Chen, and Frans M. J. Willems. Achievable information rates for fiber optics: Applications and computations. *Journal of Lightwave Technology*, 36(2):424–439, 2018.

[151] Daniel Lippiatt, Siddharth Varughese, Thomas Richter, Sorin Tibuleac, and Stephen E. Ralph. Joint linear and nonlinear noise estimation of optical links by exploiting carrier

phase recovery. In *2020 Optical Fiber Communications Conference and Exhibition (OFC)*, pages 1–3, 2020.

[152] F. J.V. Caballero, D. J. Ives, C. Laperle, D. Charlton, Q. Zhuge, M. O'Sullivan, and Seb J. Savory. Machine learning based linear and nonlinear noise estimation. *Journal of Optical Communications and Networking*, 10(10):D42–D51, 2018.

[153] Andrew D. Shiner, Mohammad E. Mousa-Pasandi, Meng Qiu, Michael A. Reimer, Eui Young Park, Michael Hubbard, Qunbi Zhuge, Francisco J. Vaquero Caballero, and Maurice O'Sullivan. Neural network training for osnr estimation from prototype to product. In *2020 Optical Fiber Communications Conference and Exhibition (OFC)*, pages 1–3, 2020.

[154] Gabriele Di Rosa, Stefanos Dris, and André Richter. Statistical quantification of nonlinear interference noise components in coherent systems. *Opt. Express*, 28(4):5436–5447, Feb 2020.

[155] Zhenhua Dong, Alan Pak Tao Lau, and Chao Lu. Osnr monitoring for qpsk and 16-qam systems in presence of fiber nonlinearities for digital coherent receivers. *Opt. Express*, 20(17):19520–19534, Aug 2012.

[156] Christian Rasmussen and Mehmet Aydinlik. Optical signal-to-noise ratio (OSNR) monitoring and measurement in optical communications sytems, December 19 2017. US Patent 9,847,833.

[157] F. J. Vaquero-Caballero, D. J. Ives, and S. J. Savory. Perturbation-based frequency domain linear and nonlinear noise estimation. *Journal of Lightwave Technology*, 40(18):6055–6063, 2022.

[158] Jianing Lu, Gai Zhou, Jing Zhou, and Chao Lu. Joint linear and nonlinear noise monitoring techniques based on spectrum analysis. *Opt. Express*, 28(24):36953–36971, Nov 2020.

[159] Hyung Joon Cho, Daniel Lippiatt, Varghese A. Thomas, Siddharth Varughese, Steven Searcy, Thomas Richter, Sorin Tibuleac, and Stephen E. Ralph. Constellation-based identification of linear and nonlinear OSNR using machine learning: a study of link-agnostic performance. *Opt. Express*, 30(2):2693–2710, 01 2022.

[160] Mohamed Al-Nahhal, Ibrahim Al-Nahhal, Octavia A. Dobre, and Sunish Kumar Orappanpara Soman. Parallel neural network structures for signal-to-noise ratio estimation

in optical fiber communication systems. *Journal of Lightwave Technology*, 42(6):1941–1954, 2024.

[161] M. Boertjes, A. S. Kashi, J. C. Cartledge, and W.-Y. Chan. Machine learning model training framework for nonlinear signal-to-noise ratio estimation in heterogeneous optical networks. *Journal of Lightwave Technology*, pages 1–11, 2024.

[162] Isaia Andrenacci, Matteo Lonardi, Petros Ramantanis, Élie Awwad, Ekhine Irurozki, Stephan Clémençon, and Sylvain Almonacil. Machine-learning-based technique to establish ASE or Kerr impairment dominance in optical transmission. *J. Opt. Commun. Netw.*, 16(4):481–492, Apr 2024.

[163] Ronen Dar and Peter J. Winzer. Nonlinear interference mitigation: Methods and potential gain. *Journal of Lightwave Technology*, 35(4):903–930, 2017.

[164] Manuel S. Neves, Abel Lorences-Riesgo, Celestino S. Martins, Sami Mumtaz, Gabriel Charlet, Paulo P. Monteiro, and Fernando P. Guiomar. Carrier-phase recovery for coherent optical systems: Algorithms, challenges and solutions. *Journal of Lightwave Technology*, 42(3):1095–1108, 2024.

[165] J. Chang, C. Hahn, X. Tang, T. Zhao, W. C. Ng, and Z. Jiang. Demonstration of longitudinal power profile estimation using commercial transceivers and its practical consideration. In *49th European Conference on Optical Communications (ECOC 2023)*, pages 1334–1337, 2023.

[166] Vittorio Curri, Andrea Carena, Andrea Arduino, Gabriella Bosco, Pierluigi Poggiolini, Antonino Nespola, and Fabrizio Forghieri. Design strategies and merit of system parameters for uniform uncompensated links supporting Nyquist-WDM transmission. *Journal of Lightwave Technology*, 33(18):3921–3932, 2015.

[167] Randy Eisenach. “ASE noise loading for terrestrial WDM applications”. Accessed: Dec 4, 2024.

[168] Ciena. “WaveLogic 6”. Accessed: Dec 4, 2024.

[169] Thomas Richter, Jie Pan, and Sorin Tibuleac. Comparison of WDM bandwidth loading using individual transponders, shaped, and flat ASE noise. In *Optical Fiber Communication Conference*, page W1B.2. Optica Publishing Group, 2018.

[170] Y. Jiang, A. Nespola, S. Straullu, F. Forghieri, S. Piciaccia, A. Tanzi, M. Ranjbar Zefreh, G. Bosco, and P. Poggiolini. Experimental test of a closed-form EGN model over C+L bands. *Journal of Lightwave Technology*, pages 1–11, 2024.

[171] Alexei Pilipetskii, Dmitry Kovsh, Eduardo Mateo, Elizabeth Rivera Hartling, Georg Mohs, Ljupcho Jovanovski, Massimiliano Salsi, Mattia Cantono, Maxim Bolshtyansky, Olivier Courtois, Olivier Gautheron, Omar Ait Sab, Pascal Pecci, Priyanth Mehta, Stephen Grubb, Takanori Inoue, Valey Kamalov, Vijay Vusirikala, Vincent Letellier, and Yoshihisa Inada. The subsea fiber as a shannon channel. In *SubOptic 2019*, 2019.

[172] Gabriella Bosco, Andrea Carena, Roberto Cigliutti, Vittorio Curri, Pierluigi Poggiolini, and Fabrizio Forghieri. Performance prediction for WDM PM-QPSK transmission over uncompensated links. In *Optical Fiber Communication Conference/National Fiber Optic Engineers Conference 2011*, page OThO7. Optica Publishing Group, 2011.

[173] Edouard Grellier and Alberto Bononi. Quality parameter for coherent transmissions with Gaussian-distributed nonlinear noise. *Opt. Express*, 19(13):12781–12788, Jun 2011.

[174] Yanchao Jiang, Fabrizio Forghieri, Stefano Piciaccia, Gabriella Bosco, and Pierluigi Poggiolini. Optimum launch power in multiband systems. In *50th European Conference on Optical Communications (ECOC 2024)*, page W2A.84, 2024.

[175] H. Buglia, E. Sillekens, A. Vasylchenkova, P. Bayvel, and L. Galdino. On the impact of launch power optimization and transceiver noise on the performance of ultra-wideband transmission systems [invited]. *J. Opt. Commun. Netw.*, 14(5):B11–B21, May 2022.

[176] Salma Escobar-Landero, Abel Lorences-Riesgo, Xiaohui Zhao, Yann Frignac, and Gabriel Charlet. S+C+L high-capacity transmission systems: Challenges and opportunities. *Journal of Lightwave Technology*, 42(12):4260–4270, 2024.

[177] S. Benedetto and P. Poggiolini. Polarization shift keying: an efficient coherent optical modulation. In *SBT/IEEE International Symposium on Telecommunications*, pages 14–20, 1990.

[178] M. A. Soto and J. A. Ramírez. Earthquake monitoring using fibre-optic distributed acoustic sensing. In *49th European Conference on Optical Communications (ECOC 2023)*, volume 2023, pages 1441–1444, 2023.

[179] Ali Masoudi and Trevor P. Newson. High spatial resolution distributed optical fiber dynamic strain sensor with enhanced frequency and strain resolution. *Opt. Lett.*, 42(2):290–293, Jan 2017.